Swansea University
Prifysgol Abertawe

Criticality of the Thirring Model in 2+1D

Jude Worthy

Primary Supervisor: Prof. Simon Hands

Administrative Supervisor: Prof. Chris Allton

Submitted to Swansea University in Fulfilment of the Requirements for the Degree of Doctor of Philosophy

Swansea University 2023

Criticality of the Thirring Model in 2+1D

Jude Worthy

Abstract

The 2+1d Thirring model provides a good laboratory to explore criticality in a strongly coupled region. We investigate the utility of Ginsparg-Wilson relation obeying Dirac operators, namely overlap operators and domain wall operators for this enterprise and seek to improve them. These operators recover global $U(2)$ symmetry in the continuum limit as required by any theory with chiral symmetry. We do this via calculation of the bilinear condensate and the evaluation of an equation of state around a phase transition. However, numerical calculations using QFTs may be computationally very expensive, especially around phase transitions. In the past often only quenched calculations have been possible. As available computing power has increased however, dynamic calculations have become increasingly feasible. In this work we carry out both quenched and dynamic simulations. We look to find critical exponents via the equation of state characterizing the behaviour of the condensate in the continuum limit, and in the process find improvements in the evaluation of the measurements.

For my mother, and in loving memory of my father.

I, Jude Worthy, declare that this thesis titled, 'Criticality of the Thirring Model in 2+1D' and the work presented in it are my own. I confirm that:

- This work has not previously been accepted in substance for any degree and is not being concurrently submitted in candidature for any degree.
- This thesis is the result of my own investigations, except where otherwise stated. Other sources are acknowledged by footnotes giving explicit references. A bibliography is appended.
- I hereby give consent for my thesis, if accepted, to be available for photocopying and for inter-library loan, and for the title and summary to be made available to outside organisations.
- The University's ethical procedures have been followed and, where appropriate, that ethical approval has been granted.

Signature:

Date:

30/8/23

Acknowledgements

My PhD studies began formally under the supervision of Prof. Simon Hands, to whom I am forever indebted. It has been a pleasure learning from and collaborating with Simon, and he has continued on in a primary supervisory capacity after departing the university. Once I was blind and now I am only blind in one eye thanks to Simon.

The administrative supervisory duties were passed on to Prof. Chris Allton, to whom I offer many thanks for carrying out that thankless task with good humour and professional diligence.

Contents

Chapter 1

Introduction

The fundamental idea of lattice field theory is to discretize spacetime, representing it as a lattice of points and links, providing a natural regularistation, allowing access to strongly coupled regions beyond the reach of perturbative methods. In Euclidean space, working with the functional formalism (path integral formulations) the discretization allows calculations on computers, utilising well established numerical methods from statistical mechanics. To find a continuum theory from the lattice one we must take the limit of the lattice spacing $a \to 0$ in a manner corresponding to the renormalized group techniques of Hamiltonian formulations, varying the parameters of the theory with a suitably to keep the physical content constant.

From a condensed matter perspective the lattice spacing may correspond to different physical systems, the lattice sites corresponding to the molecular structure of a metal for example, and we may not initially seek the continuum limit. However, we may find phase transitions in such a system occuring at critical values of the parameters. Such critical phenomena are typically found in strongly coupled regions, and happen in the continuum limit of the lattice theory. Thus the search for critical phenomena in the condensed matter community corresponds to the search for a continuum theory in the particle physics community.

From either persepctive finding the limit is a challenging task. On a lattice with a fixed number of points the continuum limit corresponds to a vanishing volume. To keep the volume constant requires a divergent number of lattice sites. Hence we must look at lattice measurements close to, but not at, the continuum limit.

At a critical phase transition some physical quantity typically undergoes some sort of continuous but non-smooth change. This quantity may be an order parameter. A correlation length associated with the order parameter will be divergent at the phase transition but will be characterised by a power law with its exponent (critical exponent) in the region around the phase transition. As such, these exponents may be seen to

characterise the physics of the associated property. In this work we look at chiral symmetry breaking, in which the chiral condensate $\langle\bar{\psi}\psi\rangle$ is the breaking order parameter, and will be looking for appropriate exponents to describe its behaviour in the critical region. To this end we carry out lattice simulations close to the transition and construct an equation of state with suitable exponents.

Working in 2+1d, while having always been of theoretical interest, has become of practical interest especially with the industrial development of graphene. Exploring the strongly coupled 2+1d Thirring model, a toy interacting fermion theory, is challenging and has seen much endeavour increasingly over recent years. For example [1–6], cover aspects including critical flavour number, U(2) symmetry breaking, and meson correlators. Different discretisations of the Dirac operator have been explored, including staggered, domain wall, and SLAC fermions, and different results have been found. It is desirable to capture as many of the continuum symmetries on the lattice as possible. However, we cannot keep them all and must choose. Since we will be interested in U(2)-symmetry breaking, picking a Dirac operator with U(2)-symmetry on the lattice would seem a sensible choice. We choose to work with overlap and domain wall operators to this end. I hope herein to contribute to this body of work.

In short the objectives of this thesis are to explore and compare some numerical attributes of the chosen U(2)-invariant Dirac operators in the context of the 2+1d Thirring model, and to calculate the critical exponents associated with the symmetry breaking bilinear condensate in the continuum limit. We will access the continuum limit of the lattice theory through the constuction of an equation of state in the vicinity of the lattice fixed point.

The thesis is laid out as follows. The basics of lattice QFT in the functional formalism is briefly highlighted in chapter 2. Some general aspects of Dirac operators are reviewed in chapter 3, with a focus on the chiral operators which will be used in the numerical calculations. Some details of the calculation of the operators are provided. Most of the results in this work relate to the bilinear condensates which are described in chapter 4. Chapter 5 reviews the Thirring model, and introduces the equation of state which will be used to find the critical exponents. Chapter 6 gives an overview of dynamic fermions and their evaluation before moving onto the results chapters. Chapter 7 shows the locality of the overlap operator and looks at the Ginsparg-Wilson errors of the operators. Chapters 8 and 9 look at the condensates, equations of state, and critical exponents for quenched and dynamic cases respectively. Chapter 10 considers the evaluation of the susceptibility and the axial ward identity. Finally a summary and outlook is given in chapter 11.

Some of the early work relating to the locality of the overlap operator has been published in the article [7] and further material has been presented and published at the symposium

[8, 9][1].

Throughout, the following labels are often used in the legends of the figures, as well as in the text. HT (occasinoally just H) denotes a formulation using the hyperbolic tanh approximation to the sign function, and Z refers to a Zolotarev approximation. S refers to a Shamir formulation and W the Wilson formulation. DW is the domain wall formulation, and OL is the overlap formulation. Q refers to quenched, and D to dynamic measurements. AXMY denotes a case where auxiliary fields have (dynamically) been generated with $L_s = X$, and the measurements have been evaluated with $L_s = Y$. M will usually refer to the mass type with M1 the standard mass, and M3 the twisted mass, although M is the the domain wall height/overlap parameter. These labels will sometimes be mixed together.

[1] Other unpublished presentations were given at the Miami 2020 Physics Conference (December 2020) and the Asia-Pacific Symposium for Lattice Field Theory (August 2020).

Chapter 2

Lattice Quantum Field Theory

2.1 Functional Formalism

Following [10] the functional formalism (path integral method) of a fermionic theory coupled to an auxiliary field in Euclidean space gives the quantisation

$$\langle O \rangle = \frac{1}{Z} \int \mathcal{D}[\psi, \bar{\psi}] \mathcal{D}[A] \exp(-S_F[\psi, \bar{\psi}, A] - S_G[A]) O[\psi, \bar{\psi}, A] \tag{2.1}$$

$$Z = \int \mathcal{D}[\psi, \bar{\psi}] \mathcal{D}[A] \exp(-S_F[\psi, \bar{\psi}, A] - S_G[A]) \tag{2.2}$$

where $\langle O \rangle$ is the observable and Z is the generating (partition) function derived from the classical action

$$S = S_F[\psi, \bar{\psi}, A] + S_G[A] \tag{2.3}$$

comprising (interacting) fermionic and bosonic components. The spinors ψ and $\bar{\psi}$ are 4-component Grassmann fields on the lattice to ensure Fermi statistics, and A is a real valued 3-component field. The actions comprise their respective lagrangains.

$$\begin{aligned} S_F &= \int dx \mathcal{L}_F[\psi(x), \bar{\psi}(x), A(x)] \\ S_G &= \int dx \mathcal{L}_G[A(x)] \end{aligned} \tag{2.4}$$

In this work we are interested in the single gauge invariantly coupled fermionic field given by eqn. 2.5, and the gauge *variant* Thirring auxiliary field given by eqn. 2.6 in 2 spatial dimensions.

$$\mathcal{L}_F = \bar{\psi}(\gamma_\mu(\partial_\mu + iA_\mu) + m)\psi \tag{2.5}$$

$$\mathcal{L}_G^{Thirring} = \frac{1}{2g^2}A_\mu^2 \tag{2.6}$$

In order to make the integrals well defined the theory must be regularized, which we achieve by moving onto a discrete lattice. The lattice regularization also enables the exploration of strong coupling for which perturbative methods are not applicable and we will then be able to calculate observables with the aid of computers. We will primarily be concerned with the evaluation of the bilinear condensate, $C = \langle\bar{\psi}\psi\rangle$. Hence our observable of choice is $O = \bar{\psi}\psi$.

2.2 Lattice Discretisation and the Dirac Operator

Working in 2 spatial dimensions, we discretise the continuum space $x = (x_0, x_1, x_2)$ with a finite volume lattice over a volume $V = T \times L^2$ where T is the extent of the time dimension and L the the extent of the spatial dimensions. We consider N_t and N_s nodes in temporal and spatial dimensions, so that we have lattice spacings $a_s = L/N_s$ and $a_t = T/N_t$ but we always work with $a = a_s = a_t$. We then have $N_v = N_s^2 N_t$ and $V = N_v a^3$. The fermion (Dirac) field points are distributed uniformly $\psi(n) \equiv \psi(x(n))$ at $x(n) = (ta, ja, ia)$ for $d = 3$ with $n = i + N_s j + N_s^2 t$, and indices running from 0 to $N_{s/t} - 1$. The volume is periodic in the spatial dimensions and anti-periodic in the temporal direction. As such there are no nodes on $x_0 = T$, $x_1 = L$, or $x_2 = L$. The anti-periodic conditions implement non-zero temperature conditions and are implemented by fixing the temporal component of the auxiliary field $A_\mu(N_t - 1, j, i) = -A_\mu(0, j, i)$. As $N_t \to \infty$, $T \to 0$.

It would seem natural to simply discretise the bosonic field A_μ on the nodes, but Wilson's formulation ensured exact gauge invariance through the introduction of the bosonic link fields $U_\mu(n)$. These links are located between nodes in their respective orientation. eg $U_1(n) \equiv U_1(t(n), i(n), j(n))$ is on the link connecting nodes with coords $(t(n), i(n), j(n))$ and $(t(n), i(n)+1, j(n))$. Such link fields may be constructed compactly or non-compactly from the auxiliary field $A_\mu(n)$.

Compact link:

$$U_\mu(n) = \exp(iaA_\mu(n)) \tag{2.7}$$

Non-Compact link:

$$U_\mu(n) = 1 + iaA_\mu(n) \tag{2.8}$$

The Taylor expansion of the compact form is identical to the non-compact form up to first order. It is tempting to think that these formulations should be equivalent in the continuum limit $a \to 0$, but we shall see that they may lead to very different results.[1]

With the link fields suitably constructed we locate the discretized fermionic components $\psi(n)$ on the nodes. The *naive* discretization of the fermionic lagrangian at node n is given by

$$\mathcal{L}_F(n) = \bar{\psi}(n)(\sum_{\mu=1}^{d} \gamma_\mu \frac{U_\mu(n)\psi(n+\hat{\mu}) - U_\mu(n-\hat{\mu})^\dagger \psi(n-\hat{\mu})}{2a} + m\psi(n)) \tag{2.9}$$

with corresponding action

$$S_F[\psi, \bar{\psi}, U] = a^3 \sum_{n\in\Lambda} \mathcal{L}_F(n) = \bar{\psi} D_0 \psi + m\bar{\psi}\psi \tag{2.10}$$

The γ_μ are elements of a Clifford algebra. We will choose from 4x4 complex valued matrix representations. 4x4 subelements of D_0, where $D = D_0 + mI$, are then given by

$$D_0(j|i) = a^3 \sum_{\mu=1}^{d} \gamma_\mu \frac{U_\mu(j)\delta_{j,i+\hat{\mu}} - U_\mu(j-\hat{\mu})^\dagger \delta_{j,i-\hat{\mu}}}{2a} \tag{2.11}$$

For the vector auxiliary field we have the lagrangian and action, where $A_\mu(n)$ is 3-component (over μ) at lattice site indexed by n, and Λ is the set of all lattice sites.

$$\mathcal{L}_G(n) = \frac{1}{g^2} \sum_{\mu} A_{n,\mu}^2 \tag{2.12}$$

$$S_G[A] = a^3 \sum_{n\in\Lambda} \mathcal{L}_G(n) \tag{2.13}$$

The discretisation provides a natural regularisation, with the grid spacing a providing an ultra-violet cutoff, and the spatial size L providing an infra-red cutoff. The allowed momenta are thus restricted to the *Brillouin zone*, $p_\mu \in [-\pi/a, \pi/a]$. To recover vacuum conditions we require $T \to \infty$, and correspondingly a finite time extent corresponds to a finite temperature system. Thermal equilibirum is reached by extending the spatial dimensions $L \to \infty$.

[1] It is to be noted that although we assume the convergence of the MCMC algorithm for the non-compact case, it is not as clear cut as for the compact case.

2.3 Lattice Measurements

We use the Matthews-Salam relations[2] [11, 12] to integrate out the Grassmann variables in the fermionic action, S_F. We find the fermion matrix $M \equiv M[A]$, where M results from the replacement of each element $D(j|i)$ with a 4x4 complex valued matrix according to the choice of gammas. Eqns 2.1 and 2.2 become

$$\langle O \rangle = \frac{1}{Z} \int \mathcal{D}[A] \exp(-S_G[A]) \det[M] \hat{O}[A] \tag{2.14}$$

$$Z = \int \mathcal{D}[A] \exp(-S_G[A]) \det[M] \tag{2.15}$$

The particular form of $\hat{O}[A]$ is not general in this notation. For example though, with $O = \bar{\psi}\psi$, and mass term $m\bar{\psi}\psi$ in the Lagrangian, $\hat{O}[A] = \mathrm{Tr}[M^{-1}]$.

The *Haar* measure of the continuum becomes the product of weighted Riemannian integration (measure) over each auxiliary field component $A_{i,\mu}$.

$$\mathcal{D}[A] = \prod_{i,\mu} \int_{-\infty}^{\infty} dA_{i,\mu} \tag{2.16}$$

Hence

$$Z = \prod_{i,\mu} \int_{-\infty}^{\infty} dA_{i,\mu} \exp(-S_G[A]) \det[M] \tag{2.17}$$

The calculations are now well defined, and it is feasible to calculate eqn. 2.14 analytically in some simple instances. However, in practice, we must resort to Monte Carlo integration, based on a series of N auxiliary link field configurations $\{A^n\}$ so that

$$\langle O \rangle \approx \frac{1}{N} \sum_{n=1}^{N} \hat{O}[A^n] \tag{2.18}$$

The error of the approximation decreases as $1/\sqrt{N}$ when the fields $\{A^n\}$ are generated independently with probability

$$P(A^n) \propto \exp(-S_G[A^n]) \det(M[A^n]) \tag{2.19}$$

The determinant must be positive for this technique to work. Unfortunately, the determinant is not guaranteed to positive, and this is known as the sign problem. A

[2] See appendix A.1.

commonly used remedy, which is assumed to be physically acceptable[3], is to replace $M[A]$ with $(M[A]M[A]^\dagger)^{1/2}$.

This covers the barest of bones of lattice field theory and we now turn to the choice of Dirac operator.

[3] $(M^\dagger M)^{1/2}$ may lose the locality of M if M not positive definite.

Chapter 3

Dirac Operators

We start by reviewing some properties and symmetries of the continuum operator, notably the $U(2)$ global symmetry, that we wish to replicate in the lattice formulations. We then go on to describe the difficulty of achieving this symmetry caused by Nielsen-Ninomiya "No-Go" theorem, which states that chiral symmetry (the analogue of $U(2)$ symmetry in 3+1d) cannot be achieved on the lattice in conjunction with a set of other desired lattice properties. The workaround to this problem, the Ginsparg-Wilson relations, is described, and Dirac operators, domain wall and overlap, satisfying these relations are then introduced. Calculational details are given of these operators. The optimal Zolotarev approximation to the sign function required by the overlap operator is specified as well as the coefficients required by the equivalent domain wall formulation. Finally the relation between the overlap and domain wall formulations is provided. With precise definitions forthcoming in this chapter, we believe this work introduces the overlap and domain wall operators with Wilson kernel and twisted mass term to the literature, and that simulations using this variant have not been carried out elsewhere before.

3.1 Properties of the Continuum Dirac Operator

We consider the Euclidean Dirac equation $(\gamma_\mu(\partial_\mu + iA_\mu) + m)\psi = 0$. In 3+1d there is no choice but for ψ to be a 4-component spinor, comprising two *Weyl* fermions and a mass term coupling them. In 2+1d it may be 2-component in the *irreducible* form comprising only a single Weyl fermion and mass term. However, this is not parity invariant (invariant under a reflection). We choose the *reducible* 4-vector form which *is* parity invariant [3], as shown in appendix A.2. Then we choose the gamma matrices

$$\gamma_0 = \begin{pmatrix} 0 & 0 & 0 & -i \\ 0 & 0 & -i & 0 \\ 0 & i & 0 & 0 \\ i & 0 & 0 & 0 \end{pmatrix}, \gamma_1 = \begin{pmatrix} 0 & 0 & 0 & -1 \\ 0 & 0 & 1 & 0 \\ 0 & 1 & 0 & 0 \\ -1 & 0 & 0 & 0 \end{pmatrix}, \gamma_2 = \begin{pmatrix} 0 & 0 & -i & 0 \\ 0 & 0 & 0 & i \\ i & 0 & 0 & 0 \\ 0 & -i & 0 & 0 \end{pmatrix} \tag{3.1}$$

and we have

$$\gamma_3 = \begin{pmatrix} 1 & 0 & 0 & 0 \\ 0 & 1 & 0 & 0 \\ 0 & 0 & -1 & 0 \\ 0 & 0 & 0 & -1 \end{pmatrix}, \gamma_5 = \begin{pmatrix} 0 & 0 & -1 & 0 \\ 0 & 0 & 0 & -1 \\ -1 & 0 & 0 & 0 \\ 0 & -1 & 0 & 0 \end{pmatrix} \tag{3.2}$$

where $\gamma_5 \equiv \gamma_0\gamma_1\gamma_2\gamma_3$ would be the *chirality* operator in 3+1d.

In 3+1d the *helicity* of a spinor $\phi(x)$ is the spin direction projected onto the plane normal to its direction of motion, and so may be imagined to be a corkscrew motion rotating either clockwise/left-handed or anti-clockwise/right-handed relative to the direction of motion [13]. Since it is relative to the direction of motion, helicity is a constant of motion but is not Lorentz invariant. However, it is independent of the frame of reference for massless particles travelling at the speed of light. The *chirality* operator γ_5 is closely connected to helicity, but is Lorentz invariant. For massless fermions it corresponds to helicity. γ_5 has degenerate eigenvalues ± 1 which are associated with a left and right handedness. As such the Dirac 4-vector may be separated into a left-handed component and right handed component via left and right projectors (operators with the property $P^2 = P$) using γ_5.

$$P_+ = \frac{1+\gamma_5}{2} \quad ; \quad P_- = \frac{1-\gamma_5}{2} \tag{3.3}$$

with further properties $P_+ + P_- = I$, $P_+P_- = P_-P_+ = 0$. We can then define left and right handed *Weyl* fermions

$$\begin{aligned} \psi_R &= P_+\psi \quad ; \quad \bar{\psi}_R = \bar{\psi}P_- \\ \psi_L &= P_-\psi \quad ; \quad \bar{\psi}_L = \bar{\psi}P_+ \end{aligned} \tag{3.4}$$

from which we make the *chiral decomposition* of the fermion action

$$S = \bar{\psi}D\psi + m\bar{\psi}\psi = \bar{\psi}_L D\psi_L + \bar{\psi}_R D\psi_R + m(\bar{\psi}_L\psi_R + \bar{\psi}_R\psi_L) \tag{3.5}$$

Eqn. 3.5 shows that the massless Dirac 4-vector may be viewed as comprising 2 independent Weyl fermions, which couple with the introduction of a mass term.

As we will see below, due to an expanded global symmetry in 2+1d there is no longer a unique choice of "chiral" projector,[1] and hence there is no longer a unique way to define left or right handedness. Since we are free to choose certain alternative projectors, we will instead use γ_3 projectors.

$$P_+ = \frac{1+\gamma_3}{2} \quad ; \quad P_- = \frac{1-\gamma_3}{2} \tag{3.6}$$

The choice of γ_3 in eqn. 3.2 leads to these projectors having the simple form

$$P_+ = \begin{pmatrix} I & 0 \\ 0 & 0 \end{pmatrix}; P_- = \begin{pmatrix} 0 & 0 \\ 0 & I \end{pmatrix} \tag{3.7}$$

where I is the 2×2 identity matrix. γ_5 and γ_3 are *not* interchangeable in general, even though we may choose either for the projector.

Having introduced chirality, we can introduce *chiral symmetry*. In 3+1d massless fermions have global invariance under the *chiral rotation*

$$\psi \to e^{i\alpha\gamma_5}\psi \quad ; \quad \bar{\psi} \to \bar{\psi}e^{i\alpha\gamma_5} \tag{3.8}$$

Chirality can be equivalently expressed by the *chirality relation*, the anti-commuting relation

$$D\gamma_5 = -\gamma_5 D \tag{3.9}$$

In 2+1d the Euclidean Dirac action for fermions was given by eqns. 2.4 and 2.5. The action has global symmetries [3]

$$\psi \to e^{i\alpha}\psi \; ; \; \bar{\psi} \to \bar{\psi}e^{-i\alpha} \tag{3.10a}$$

$$\psi \to e^{\alpha\gamma_3\gamma_5}\psi \; ; \; \bar{\psi} \to \bar{\psi}e^{-\alpha\gamma_3\gamma_5} \tag{3.10b}$$

Further, when $m = 0$,

$$\psi \to e^{i\alpha\gamma_5}\psi \; ; \; \bar{\psi} \to \bar{\psi}e^{i\alpha\gamma_5} \tag{3.11a}$$

[1] Strictly speaking, there is no chirality in 2+1d, but we continue to use the analogy.

$$\psi \to e^{i\alpha\gamma_3}\psi \;\; ; \;\; \bar{\psi} \to \bar{\psi}e^{i\alpha\gamma_3} \tag{3.11b}$$

These make up a $U(2)$ symmetry, explicitly breaking to a $U(1) \otimes U(1)$ with the mass term (the symmetry breaking is $U(1) \otimes U(1) \to U(1)$ in 3+1d). This symmetry was enabled by choosing the reducible rather than irreducible spinors. Since we are working in a 2+1d "physical" space, one may view the extra γ_3 spin dimension as a fictitious non-physical extra dimension. As well as eqn. 3.9 we have

$$\begin{aligned} D\gamma_3 &= -\gamma_3 D \\ D\gamma_3\gamma_5 &= \gamma_5\gamma_3 D \end{aligned} \tag{3.12}$$

We distinguish explicit, spontaneous, and anomalous symmetry breaking [14]. Explicit symmetry breaking occurs in the classical lagrangian as with the mass term in eqn. 3.5. Anomalous symmetry breaking occurs when the lagrangian keeps its symmetry but on quantisation, that is taking the path integral over the lagrangian, loses the invariance. The symmetry breaking is associated with the measure rather than the lagrangian itself. Spontaneous symmetry breaking maintains the symmetry in the lagrangian, but it is broken in the ground state of the system. This is associated with a degeneracy of ground states. These forms are not mutually exclusive but spontaneous symmetry breaking may be hidden by anomalous and anomalous may be hidden by explicit.

In a chiral theory, chirality swaps under a parity (reflection) transformation. In a vector theory, chirality remains constant under a parity (reflection) transformation [15, 16]. So chiral symmetry does not imply a chiral theory. The search for a chiral theory on the lattice was a signifcant challenge and led to the chirally symmetric Dirac operators which we will consider, albeit with vector theories. In 3+1d chiral symmetry is anomalous. Not so in 2+1d and we may be able to observe spontaneous symmetry breaking at some critical value of some symmetry breaking parameter should the model possess such a property.

Having already chosen the parity invariant 4-component form of ψ we are allowed to replace the mass with the *twisted* invariant mass terms [3]:

$$\begin{aligned} m &\to i\gamma_3 m \\ m &\to i\gamma_5 m \end{aligned} \tag{3.13}$$

which were shown to have signifcant numerical advantages. The twisted mass terms are anti-hermitian. They are a consequence of the $U(1) \otimes U(1)$ symmetry and hence found

via the rotations eqns. 3.11a and 3.11b. We will use the $m \to i\gamma_3 m$ variant extensively throughout this work.

3.2 Wilson Dirac Operator

In the continuum a single massless fermion with momentum p is identified as a pole in the momentum space propagator. Unfortunately, on the lattice we find 2^d such poles, where d is the dimension of the problem. This is known the *doubling problem*. Wilson added a vanishing term (as $a \to 0$), $-a/2D_\mu^2$, to the lagrangian to circumvent this. In the continuum

$$S_F[\psi, \bar{\psi}, A] = \int d^4x\, \bar{\psi}(x)(\gamma_\mu D_\mu - \frac{a}{2}D_\mu^2 + m)\psi(x) \tag{3.14}$$

$$D_\mu = \partial_\mu + iA_\mu(x) \tag{3.15}$$

We presented the naive Dirac operator on the lattice in section 2.2. We further add the (lattice) Wilson correction

$$\bar{\psi}W\psi = -\frac{a^5}{2}\sum_{n\in\Lambda}\bar{\psi}(n)(\sum_{\mu=1}^{d}\frac{U_\mu(n)\psi(n+\hat{\mu}) - 2\psi(n) + U_{-\mu}(n)\psi(n-\hat{\mu})}{a^2}) \tag{3.16}$$

so the entries of W are

$$W(j|i) = -\frac{a^5}{2}\sum_{\mu=1}^{d}\frac{U_\mu(j)\delta_{j,i+\hat{\mu}} - 2\delta_{j,i} + U_{-\mu}(j)\delta_{j,i-\hat{\mu}}}{a^2} \tag{3.17}$$

The Wilson Dirac operator is then just $D_W = D_0 + W$ and the Wilson Dirac action is

$$S_F[\psi, \bar{\psi}, U] = \bar{\psi}D_W\psi + m\bar{\psi}\psi \tag{3.18}$$

The Wilson-Dirac operator does not have chiral symmetry or $U(2)$ symmetry in 2+1d. However, it is γ_5-hermitian, $\gamma_5 D\gamma_5 = D^\dagger$, and also γ_3-hermitian in 2+1d.

3.3 Nielsen-Ninomiya No-Go Theorem

Unfortunately the Wilson term added to the Dirac operator to deal with the doubling problem explicitly breaks chiral symmetry, i.e. while $\gamma_5 D_0 = -D_0\gamma_5$, $\gamma_5 D_W \neq -D_W\gamma_5$. More broadly the Nielsen-Ninomiya No-Go theorem [17], in 3+1d, asserts that certain

desirable properties of a lattice model are simultaneously unachievable. [18] restates the theorem as that there can be no net chirality (i.e. the number of left handed and right handed particles is equal, and hence we cannot isolate a single left or right handed particle, which is an objective of a chiral theory) in a lattice model of fermions in which the Hamiltonian satisfies the following conditions:

1) it is quadratic in the fields
2) it is invariant under translations of the (cubic) lattice
3) it is invariant under change of the chiral phase of the fields
4) it is local, specifically in the sense that it is continuous in momentum space

Proofs and variants under differing assumptions have been proposed and [19] provides one of the clearer introductions to the topic including the following definition in momentum space. Assuming the fermionic lattice action $S_F = a^4 \sum_p \bar{\psi}_p \tilde{D}(p) \psi_p$, then the following four assumptions imply the existence of doublers and that they comprise an equal number of left and right handed particles.

1) Reflection positivity. This may be expressed as $\tilde{D}(p) = \gamma_4 \tilde{D}(\mathbf{p}, -\mathrm{p}_4)\gamma_4$.
2) Cubic group symmetry. These are the rotations and translations on the cubic lattice and imply that further reflections hold: $\tilde{D}(p) = \gamma_\mu \tilde{D}^\dagger(p)(R_\mu p)\gamma_\mu$ with $(R_\mu p)_\nu = p_\nu(1 - 2\delta_{\mu\nu})$.
3) Chiral invariance. $\tilde{D}(p) = -\gamma_5 \tilde{D}(p)\gamma_5$.
4) Locality. Locality in coordinate space, $||D(x)|| \leq C\exp(-\gamma x)$ should fall off exponentially with the number of lattice spacings, implies continuity in momentum space of $\tilde{D}(p)$.

In order to remove the doublers one of these conditions must be broken. We note that a discretisation is *ultra-local* if the derivative stencil is limited to only a finite number neighbouring lattice sites.

In 2+1d we (masslessly) have U(2) symmetry analogously to chiral symmetry, and points (3) are altered as set out in the next section.

3.4 Ginsparg Wilson Relation

The Ginsparg-Wilson [10, 20] (GW) relation provided the solution to the Nielsen-Ninomiya conundrum which had been thought to be an insurpassable problem for chirally invariant theories. Nevertheless, the domain wall [21] and overlap operators [22] circumvent the chiral condition. With a vanishing (in the continuum limit as $a \to 0$) modification to the 3rd condition of the Neilsen-Ninomiya No-Go theorem, $\gamma_5 D + D\gamma_5 = 0$, all

4 properties can be achieved for finite a. The (GW) relation may be given equivalently by either of

$$\begin{aligned} \gamma_5 D + D\gamma_5 &= 2aD\gamma_5 D \\ (1-aD)\gamma_5 D &= -D\gamma_5(1-aD) \end{aligned} \tag{3.19}$$

which replaces the chiral relation. For the 2+1d formulation, further GW relations [3, 23, 24] are found.

$$\begin{aligned} \gamma_3 D + D\gamma_3 &= 2aD\gamma_3 D \\ \gamma_3\gamma_5 D - D\gamma_3\gamma_5 &= 0 \end{aligned} \tag{3.20}$$

Together these correspond to the invariant transformations

$$\begin{aligned} \Psi \to e^{i\alpha\gamma_3(1-\frac{aD}{2})}\Psi \;\; ; \;\; \bar{\Psi} \to \bar{\Psi} e^{i\alpha\gamma_3(1-\frac{aD}{2})} \\ \Psi \to e^{i\alpha\gamma_5(1-\frac{aD}{2})}\Psi \;\; ; \;\; \bar{\Psi} \to \bar{\Psi} e^{i\alpha\gamma_5(1-\frac{aD}{2})} \\ \Psi \to e^{i\alpha\gamma_3\gamma_5}\Psi \;\; ; \;\; \bar{\Psi} \to \bar{\Psi} e^{i\alpha\gamma_3\gamma_5} \end{aligned} \tag{3.21}$$

We also require that the Dirac operator D has γ_5- and γ_3-hermiticity, i.e. $\gamma_5 D\gamma_5 = \gamma_3 D\gamma_3 = D^\dagger$. The GW relation may be further expressed in terms of a fully chirally symmetric, but non-local, Dirac operator D_c, such that $D_c\gamma_5 + \gamma_5 D_c = 0$.

$$\begin{aligned} D_c &= (1-aD)^{-1}D \\ D_c^{-1} &= D^{-1} - a \end{aligned} \tag{3.22}$$

GW fermions do not suffer exceptional configurations [10]. Exceptional configurations occur when negative real eigenvalues are close to the mass value. A vanishingly small mass term will always be enough to render the smallest eigenvalue vanishingly positive.

Mass terms have not been considered so far. [25] specifies, with $a = 1$, the bare mass to be added directly to the chiral Dirac operator rather than the GW operator, resulting in the relations

$$D = (D_c + m)(1 + D_c)^{-1}$$
$$D_c = \frac{D - m}{1 - D} \tag{3.23}$$

3.5 Ginsparg Wilson Dirac Operators

In this work we consider overlap and domain wall formulations which may be formally equivalent (domain wall may be seen as a generalisation of the overlap although developed first). Within each method which we choose twisted or non-twisted mass, Shamir or Wilson kernel, and Zolotarev or hyperbolic tanh (HT) sign approximations. One of the driving considerations of this work is to discern the most pertinent differences between the formulations in the context of the 2+1d Thirring model. The chiral anomaly for which the overlap method was developed does not exist in 2+1d, but it is thought we still require the correct chiral symmetry on the lattice to attain the correct continuum theory in the $a \to 0$ limit.

Although we do not explore it in this work we mention the SLAC Dirac operator as an alternative solution to the doubling problem, which has been used in other closely related studies [4], and has found conflicting results which will be discussed further. Rather than using a finite point stencil for the derivative, a fourier representation is used which does not have doublers, since the dispersion relation remains linear. However, it is non-local, upsetting the Nielsen-Ninomiya conditions in that way[2].

3.6 Domain Wall Operator

The domain wall method that eventually led to the overlap operator was initially developed by Kaplan [21], building on work of Callen and Harvey [26], and was an attempt to find a chiral theory on the lattice, with the plan to put the electroweak part of the Standard Model on the lattice. Eventually, it was used for QCD, a vector theory, and is used in this work. We review the origin of the method closely following the original work [21] and especially a good early overview [27].

To begin, consider the Hamiltonian operator of free fermions in a single spatial dimension $H = \sigma_1[\sigma_2\partial_x + m_0]$, where σ_i are Pauli matrices, and $\sigma_3 = -\sigma_1\sigma_2$ is the chirality operator. Define a so called mass defect term in a non-physical extra dimension, s, such that $m(s)$ is a smooth asymptotic monotonic odd function with

[2]However, it can be shown that taking the derivative of a sufficiently smooth ϕ, with a Fourier operator *is* exponentially local. The non-locality only manifests with discontinuous ϕ. Limiting the possible Dirac fields ϕ on the lattice may provide another way around the Nielsen-Ninomiya theorem.

$$m(s) = \begin{cases} -m_0 & s \to -\infty \\ 0 & s = 0 \\ +m_0 & s \to +\infty \end{cases} \tag{3.24}$$

Then we consider the new Hamiltonian with the extra dimension

$$H = -\sigma_1[\sigma_2\partial_x + \sigma_3\partial_s + m(s)] \tag{3.25}$$

which has chiral energy eigenstates

$$\Psi_\pm = e^{ip_x x}\Phi_\pm(s)u_\pm \tag{3.26}$$

$$\Phi_\pm(s) = \exp(\pm\int_0^s m(s')ds') \tag{3.27}$$

and $u_\pm$ are chiral eigenstates

$$\sigma_3 u_\pm = \pm u_\pm \tag{3.28}$$

$\Phi_+(s)$ diverges and hence is not normalizable, leaving $\Phi_-(s)$ as the only acceptable solution. The chiral zeromode eigenstate it describes propagates parallel to the wall and falls off exponentially away from the wall. Hence the mode is bound to the $s = 0$ hyperplane.

Moving to an infinite lattice, with lattice spacing a and $m(s)$ given by a step function

$$m(s) = m_0\theta(s); \theta(s) = \begin{cases} -1 & s \le a \\ 0 & s = 0 \\ +1 & s \ge a \end{cases} \tag{3.29}$$

where $m_0 \equiv \frac{\sinh(a\mu_0)}{a}$ we have the Hamiltonian given by

$$H = -\sigma_1[\sigma_2\triangle_x + \sigma_3\triangle_s + m(s)] \tag{3.30}$$

where $\triangle_k$ is the usual 2nd order 1st derivative stencil. This has two chiral zeromode solutions

$$\Psi_\pm = e^{ikx}\Phi_\pm(s)u_\pm \tag{3.31}$$

where, with n_s the index of the lattice node in the extra s-dimension,

$$\Phi_+(s) = e^{\mu_0|s|} \tag{3.32}$$

$$\Phi_-(s) = (-1)^{n_s}\Phi_+(s) \tag{3.33}$$

$\Phi_+(s)$ is now normalizable, and hence is also an acceptable solution. Unfortunately there are still doublers and we have 2 positive chirality states, and 2 negative chirality states (2^d in higher dimensions). Again we can turn to the Wilson correction for doublers with the Hamiltonian

$$H = -\sigma_1[\sigma_2\triangle_x + \sigma_3\triangle_s + m(s) - r(\triangle_{xx} + \triangle_{ss})] \tag{3.34}$$

which has solutions

$$\Phi_\pm(s \pm a) = -k_{eff}(s)\Phi_\pm(s) \tag{3.35}$$

and it is found that not only are the doublers removed, but the Φ_+ solution is not normalizable, resulting in a single chiral zero mode bound to the domain wall and exponentially decreasing away from the wall, which was the objective of the method. Unfortunately, for calculations we must have a finite lattice and boundary conditions (bcs) must be imposed. Periodic bcs in the s-direction and antiperiodic bcs in the x-direction are chosen. To ensure that solutions are separable in the s-dimension, the lattice Hamiltonian eqn. 3.34 is rewritten

$$H = -\sigma_1[\sigma_2\sin(k) + \sigma_3\triangle_s + m(s) - r(\cos(k) - 1) - r\triangle_{ss})] \tag{3.36}$$

with momenta k given by, for $n = 0, ..., L-1$

$$k = \frac{\pi}{L}(n + 1/2) \tag{3.37}$$

The mass terms are given by

$$m(s) \equiv \sinh(\mu_0)\theta(s); \theta(s) = \begin{cases} -1 & 1 < s < \frac{L_s+1}{2} \\ +1 & \frac{L_s+1}{2} < s < L_s \\ 0 & s = 1, \frac{L_s+1}{2} \end{cases} \tag{3.38}$$

Now there are two domain walls, and two defects, one at $s = 1$ and one at $s = \frac{L_s+1}{2}$. The energy eigenvalues of eqn. 3.36 come in $\pm$ pairs each corresponding to an eigenstate bound to one of the defects and of opposite chirality.

Finally we want to couple to an auxiliary field. Unfortunately, regardless of whether the auxiliary field is constructed with an extra s-dimension or not, the theory is vector like again, and not the chiral theory that was initially envisaged. However, the electro-weak sector of the Standard Model was the target chiral theory. Shamir and Furman [28, 29] proposed using the method for QCD, a vector-like theory, and provided a slightly different formulation that is the most often used, the most salient point now being that it satisfies the Ginsparg-Wilson relation. The lattice mass distribution now has the defect on the boundaries rather than the interior walls.

$$m(s) = \begin{cases} -M & 0 < s < L_s \\ 0 & s = 0, L_s \end{cases} \tag{3.39}$$

We present that formulation and similar formulations in the following. It is most easily viewed in a reduced matrix form in the extra dimension, where $D_W \equiv D_W(-M)$ contains the domain wall height, M, and m is a bare mass which we require to be introduced into the formalism to take the $m \to 0$ limit.

$$D_{SDW}(m) = \begin{pmatrix} D_W + I & -P_- & 0 & mP_+ \\ -P_+ & D_W + I & -P_- & 0 \\ 0 & -P_+ & D_W + I & -P_- \\ mP_- & 0 & -P_+ & D_W + I \end{pmatrix} \tag{3.40}$$

where we identify the fermion on the wall with

$$\begin{aligned} \psi(x) &= P_+\Psi(x, N) + P_-\Psi(x, 1) \\ \bar{\psi}(x) &= \bar{\Psi}(x, 1)P_+ + \bar{\Psi}(x, N)P_- \end{aligned} \tag{3.41}$$

We consider this the standard formulation which has the standard mass term, the Shamir kernel, and the hyperbolic tanh sign approximation. To consider the variants we split eqn. 3.40 into component massive and non-massive parts, $D_{DW}(m) = D^0_{DW} + D^m_{DW}$, and with the introduction of coefficients ω_s into the diagonal of the kinematic component, which are set to 1 for the usual hyperbolic tanh (HT) formulation.

$$D^0_{SDW} = \begin{pmatrix} \omega_1 D^{\parallel} + I & -P_- & 0 & 0 \\ -P_+ & \omega_2 D^{\parallel} + I & -P_- & 0 \\ 0 & -P_+ & \omega_3 D^{\parallel} + I & -P_- \\ 0 & 0 & -P_+ & \omega_4 D^{\parallel} + I \end{pmatrix} \tag{3.42}$$

$$D^{m1}_{SDW} = \begin{pmatrix} 0 & 0 & 0 & P_+ \\ 0 & 0 & 0 & 0 \\ 0 & 0 & 0 & 0 \\ P_- & 0 & 0 & 0 \end{pmatrix} \tag{3.43}$$

Then without adjustment to the kinematic component, we may choose the twisted mass form

$$D^{m3}_{SDW} = i\gamma_3 D^{m1}_{SDW} = \begin{pmatrix} 0 & 0 & 0 & i\gamma_3 P_+ \\ 0 & 0 & 0 & 0 \\ 0 & 0 & 0 & 0 \\ i\gamma_3 P_- & 0 & 0 & 0 \end{pmatrix} \tag{3.44}$$

The subscript SDW denotes the Shamir kernel formulations. We also consider the Wilson kernel formulations, subscript WDW, introduced by Borici [30], and made optimal by Chiu [31], the latter introducing non-unity coefficients chosen to match the Zolotarev approximation in the overlap operator.

$$D^0_{WDW} = \begin{pmatrix} \omega_1 D^{\parallel} + I & (\omega_1 D^{\parallel} - I)P_- & 0 & 0 \\ (\omega_2 D^{\parallel} - I)P_+ & \omega_2 D^{\parallel} + I & (\omega_2 D^{\parallel} - I)P_- & 0 \\ 0 & (\omega_3 D^{\parallel} - I)P_+ & \omega_3 D^{\parallel} + I & (\omega_3 D^{\parallel} - I)P_- \\ 0 & 0 & (\omega_4 D^{\parallel} - I)P_+ & \omega_4 D^{\parallel} + I \end{pmatrix} \tag{3.45}$$

We denote the T1 mass terms, mD^{m1}_{TOL}, which are correspondingly given as

$$D^m_{WDW} = \begin{pmatrix} 0 & 0 & 0 & -(\omega_1 D^{\parallel} - I)P_+ \\ 0 & 0 & 0 & 0 \\ 0 & 0 & 0 & 0 \\ -(\omega_4 D^{\parallel} - I)P_- & 0 & 0 & 0 \end{pmatrix} \tag{3.46}$$

$$D^{m3}_{WDW} = \begin{pmatrix} 0 & 0 & 0 & -i(\omega_1 D^{\parallel} - I)P_+\gamma_3 \\ 0 & 0 & 0 & 0 \\ 0 & 0 & 0 & 0 \\ -i(\omega_4 D^{\parallel} - I)P_-\gamma_3 & 0 & 0 & 0 \end{pmatrix} \tag{3.47}$$

The identification with the fermion fields must be adjusted from eqn. 3.48.

$$\begin{aligned} \psi(x) &= P_+\Psi(x,N) + P_-\Psi(x,1) \\ \bar{\psi}(x) &= -\bar{\Psi}(x,1)(\omega_1 D^{\parallel} - I)P_+ - \bar{\Psi}(x,N)(\omega_N D^{\parallel} - I)P_- \end{aligned} \tag{3.48}$$

The domain wall fermionic partition function $Z_F = \int \mathcal{D}[\Psi, \bar{\Psi}, U]\ e^{-S_F[\Psi,\bar{\Psi},U]}$, with $S_F = \int \bar{\Psi} D_{DW}[U]\Psi$, includes not only the fermion field identified in eqns. 3.41 and 3.48 but also $L_s - 1$ non-physical fields spread throughout the extra dimension. While measurements may be taken with identification of the physical field we need to add so called *Pauli-Villars* fields to the action to make a partition function which corresponds to a single field. This is necessary for the correct production of auxiliary fields as shown in chapter 6. We require

$$Z = \int \mathcal{D}[\Psi, \bar{\Psi}, \Phi, \bar{\Phi}, U]\ e^{-S_F[\Psi,\bar{\Psi},U] - S_G[U] - S_{PV}[\Phi,\bar{\Phi},U]} \tag{3.49}$$

where the Pauli-Villars action S_{PV} can be defined in terms of the domain wall operator with mass set to 1.

$$S_{PV}[\Phi, \bar{\Phi}, U] = \int_x \Phi D_{DW}[U](1)\Phi \tag{3.50}$$

We note that these pseudo fermions Φ, $\bar{\Phi}$, are complex valued rather than being Grassmann numbers, and hence are bosonic, with the property that

$$\begin{aligned} \int \mathcal{D}[\Phi, \bar{\Phi}, U]\ e^{\int_x \bar{\Phi} D_{DW}[U]\Phi} &= \frac{1}{\int \mathcal{D}[\Psi, \bar{\Psi}, U]\ e^{\int_x \bar{\Psi} D_{DW}[U]\Psi}} \\ &= \frac{1}{\det[D_{DW}]} \end{aligned} \tag{3.51}$$

3.7 Overlap Dirac Operator

The overlap operator was developed in a series of papers [32, 33] following on from Kaplan's orginal domain wall paper [21], before finally finding its modern form by Neuberger [22] in the lattice functional formalism. It was developed in the Hamiltonian formalism and a review of the initial development is provided by Jansen [27]. It is related to the domain wall operator, exactly when the bulk formulation is used[3]. It was originally given by (although without the mass term), with lattice spacing $a = 1$,

$$D_{OL} = \frac{1+m}{2} + \frac{1-m}{2} V \tag{3.52}$$

$$V = D_W (D_W^\dagger D_W)^{-1/2} \tag{3.53}$$

$$D_W \equiv D_W(-M) \tag{3.54}$$

Equivalently, since $D_W = \gamma_5 D_W^\dagger \gamma_5$,

$$D_{OL} = \frac{1+m}{2} + \frac{1-m}{2} \gamma_5 \mathrm{sgn}(H_W) \tag{3.55}$$

$$H_W = \gamma_5 D_W \tag{3.56}$$

where $0 < M < 2$ (the mass term in the Wilson Dirac operator, eqn. 3.54) is here an overlap regularisation parameter[4] corresponding to the domain wall height, and the sign function is defined by $\mathrm{sgn}(X) = X(X^2)^{-1/2}$. Eqn. 3.56 is the *Wilson kernel* . The kernel is not unique, and H_W may be replaced, most notably by the*Shamir kernel* H_S where

$$H_S = \gamma_5 D_W (2 + D_W)^{-1} \tag{3.57}$$

and the Mobius kernels which comprise combinations of the two. We focus on the Wilson and Shamir kernels. In 2+1d we may replace the γ_5 with γ_3 [35] so that we have the structurally identical formulation

$$D_{OL} = \frac{1+m}{2} + \frac{1-m}{2} \gamma_3 \mathrm{sgn}(H_W) \tag{3.58}$$

$$H_W = \gamma_3 D_W \tag{3.59}$$

We also have the alternative mass formulations

[3] The bulk formulation uses the same auxiliary field on every slice in the extra s-dimension.

[4] There is topological significance to this parameter not considered in this work, as discussed in [34] for example.

$$D_{OL}^{im\gamma_3} = \frac{1 + im\gamma_3}{2} + V\frac{1 - im\gamma_3}{2} \tag{3.60}$$

$$D_{OL}^{im\gamma_5} = \frac{1 + im\gamma_5}{2} + V\frac{1 - im\gamma_5}{2} \tag{3.61}$$

which should be physically the same. Although V is γ_3,γ_5-hermitian, the new mass terms are not (since i makes them anti-hermitian). Note also there is a numerical difference whether the mass term is left or right of the V term.

An approximation to the sign function is necessary, and typically a rational function is used. After the approximation is applied the operator is sometimes referred to as the *truncated* overlap operator, although we will continue to refer to the approximation as the overlap operator.

Similarly to the domain wall operator, it is applicable to vector theories and has been applied extensively to QCD. As such it has been designated as the vector overlap operator [36], whereas the same authors introduce the chiral overlap operator. The chiral overlap operator exploits further similarity with the domain wall operator which is more general in the sense that the auxiliary field may vary in the extra dimension. The chiral overlap operator uses this flexibility to have different auxiliary fields associated with left and right chirality modes.

We see that the overlap operator satisfies the GW conditions, eqns. 3.19 and 3.20

$$\begin{aligned} \gamma_3 D + D\gamma_3 &= \gamma_3(\frac{1}{2} + \frac{1}{2}V) + (\frac{1}{2} + \frac{1}{2}V)\gamma_3 \\ &= \gamma_3 + \gamma_3\frac{V}{2} + \frac{V}{2}\gamma_3 = \frac{1}{2}(\gamma_3 + \gamma_3 V + V\gamma_3 + \gamma_3) \\ &= 2(\frac{1}{2} + \frac{1}{2}V)(\frac{\gamma_3}{2} + \frac{\gamma_3}{2}V) = 2D\gamma_3 D \end{aligned} \tag{3.62}$$

The same holds for the γ_5 formulation, and also

$$\begin{aligned} \gamma_3\gamma_5 D - D\gamma_3\gamma_5 &= \gamma_3 D^\dagger\gamma_5 - D\gamma_3\gamma_5 \\ &= D\gamma_3\gamma_5 - D\gamma_3\gamma_5 = 0 \end{aligned} \tag{3.63}$$

However, it is not so clear that they satisfy locality. However, we will numerically demonstrate this in chapter 7.

3.8 Direct Calculation of the Overlap Operator

The computational difficulty in calculating the overlap operator is in the sign function. Fortunately it can be expressed, and calculated approximately, as a rational function, including as a factored expression or as a partial fraction. The partial fraction formulation may be derived from the factored form. The sign function can be expressed as [37], where the coefficients are to be determined.

$$\mathrm{sgn}(x) = cx\frac{\prod_i x^2 - n_i}{\prod_j x^2 - d_j} \tag{3.64}$$

and hence we have

$$\begin{aligned} D_{OL} &= \frac{1+m}{2} + \frac{1-m}{2} c D_W \frac{\prod_i (\gamma_5 D_W)^2 - n_i I}{\prod_j (\gamma_5 D_W)^2 - d_j I} \\ D_{OL} &= \frac{1+m}{2} + \frac{1-m}{2} c D_W \frac{\prod_i D_W^\dagger D_W - n_i I}{\prod_j D_W^\dagger D_W - d_j I} \end{aligned} \tag{3.65}$$

The denominators may be evaluated, for example, successively with a conjugate gradient algorithm, or simultaneously with a multishift conjugate gradient algorithm [38]. The factored form above may be reexpressed as a partial fraction for improved numerical stability, in which eqn. 3.65 becomes

$$D_{OL} = \frac{1+m}{2} + \frac{1-m}{2} c D_W (a_0 + \sum_j \frac{a_j}{D_W^\dagger D_W - d_j I}) \tag{3.66}$$

The product ranges are $i = 1, ..., N_i$, $j = 1, ..., N_j$. a_0 is one if $N_i = N_j$ and zero if $N_i < N_j$. To evaluate with the Shamir kernel, $D_S = D_W[2 + D_W]^{-1}$, with $D_S^\dagger = D_W^\dagger[2 + D_W^\dagger]^{-1}$, which corresponds to the domain wall formulation eqn. 3.42, we may use

$$\begin{aligned} V_S &= \frac{D_W}{2+D_W}[\frac{D_W^\dagger}{2+D_W^\dagger}\frac{D_W}{2+D_W}]^{-1/2} \\ &\approx \frac{D_W}{2+D_W}\sum_j a_j(2+D_W)[D_W^\dagger D_W + (2+D_W^\dagger)d_i(2+D_W)]^{-1}(2+D_W^\dagger) \end{aligned} \tag{3.67}$$

3.8.1 Hyperbolic Tangent Approximation

The coefficients must be chosen. A simple approximation to the sign function is given by the hyperbolic tangent (polar) approximation [39].

$$\mathrm{sgn}(x) \approx \tanh(n \tanh^{-1} x) = \frac{1 - (\frac{1-x}{1+x})^n}{1 + (\frac{1-x}{1+x})^n} \tag{3.68}$$

The approximation becomes exact as $n \to \infty$. Note for matrices $(1+x)/(1+y)$ would be ambiguous if x and y do not commute. This becomes

$$\mathrm{sgn}(x) \approx \begin{cases} xn \dfrac{\prod_{j=1}^{n/2-1} [x^2 + (\tan \frac{j\pi}{n})^2]}{\prod_{j=0}^{n/2-1} [x^2 + (\tan \frac{(j+1/2)\pi}{n})^2]} & n \text{ even} \\ \dfrac{x}{n} \prod_{j=1}^{(n-1)/2} \dfrac{[x^2 + (\tan \frac{j\pi}{n})^2]}{[x^2 + (\tan \frac{(j-1/2)\pi}{n})^2]} & n \text{ odd} \end{cases} \tag{3.69}$$

and the partial fraction expressions

$$\mathrm{sgn}(x) \approx \begin{cases} \dfrac{2x}{n} \sum_{j=0}^{n/2-1} \dfrac{1 + (\tan \frac{(j+1/2)\pi}{n})^2}{x^2 + (\tan \frac{(j+1/2)\pi}{n})^2} & \text{even} \end{cases} \tag{3.70}$$

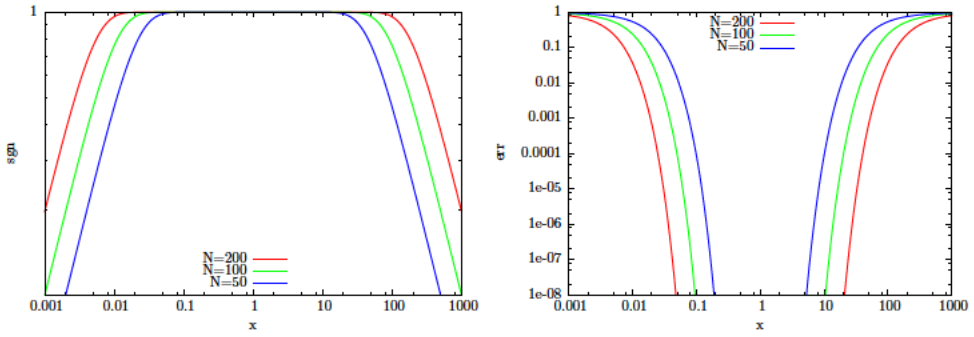

FIGURE 3.1: Hyperbolic tangent (polar) approximation to the sign function with different n. Left panel: Sign Function. Right panel: Error.

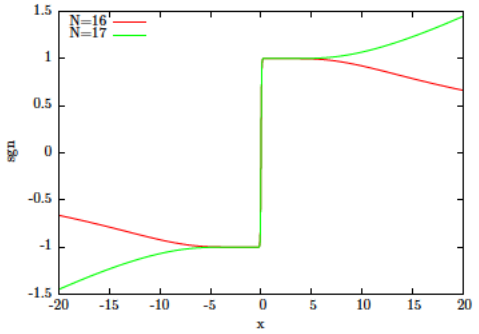

FIGURE 3.2: Hyperbolic tangent approximation to the sign function.

We see in figure 3.1 that the approximation is roughly symmetric about $x = 1$, and that the error, in the right panel, remains large away from $x = 1$ even for relatively large n. It is strictly symmetric about 0, as shown in fig. 3.2 with the approximation vanishing as it approaches zero for both even and odd cases, and as $x \to \infty$ for even n cases. However, it seems worthwhile choosing even n since the odd n approximation diverges as $x \to \infty$

We can use the scaling rule, eqn. 3.71 [40], to keep the accuracy in the lower range, and forgoing it in the upper range (or vice versa). Significant reductions in n can potentially be achieved, improving the speed of calculation of the approximation. Fig. 3.3 shows the scalings where N has been reduced from 200 to 50 via scalings of 1 to 4. The error at the lower range remains nearly identical to the higher n counterpart.

$$\mathrm{sgn}(x; n) \approx \mathrm{sgn}(sx; n/s) \tag{3.71}$$

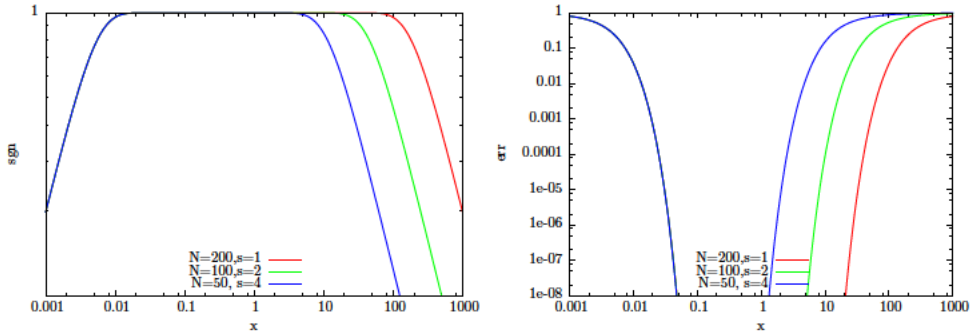

FIGURE 3.3: Scaled hyperbolic tanh (polar) approximation to the sign function with different scale factor s. Left panel: Sign Function. Right panel: Error.

3.8.2 Zolotarev Optimal Rational Function

We seek an odd rational approximation over the positive and negative ranges $[r_1, r_2]$ and $[-r_2, -r_1]$. Zolotarev [41] found optimal such rational approximations which we denote

$$\mathcal{Z}_{\text{sgn}}^{[r_1,r_2]}(x) \approx \text{sgn}(x) \tag{3.72}$$

The approximation is optimal in the L_∞ norm in the specified range, i.e. no other rational approximation exists over the specified range that does not have a larger maximum error somewhere in that range.

Herein we follow [31, 37, 42–44], which provide derivations. At the crux of it is the Jacobi elliptic sine function $\text{sn}(z, k)$, and what we call the Zolotarev elliptic function, with coefficients given in the algorithm box below

$$\frac{\text{sn}(z/M, \lambda)}{\text{sn}(z, k)} = \frac{1}{M} \prod_{m=1}^{N} \frac{1 - \frac{\text{sn}(z,k)^2}{c_m}}{1 - \frac{\text{sn}(z,k)^2}{c'_m}} \tag{3.73}$$

from which we we can find the continuous real rational function by considering the contour $z(t) = tK$ for $t \in [0, 1]$ and $z(t) = K + i(t-1)K'$ for $t \in [1, 2]$, where $K \equiv K(k)$ and $K' \equiv K(k')$ are the complete elliptic integrals, defined in the box below, and $k' = (1-k)^{1/2}$. Specifying $x = \text{sn}(z(t), k)$ gives

$$\text{sn}(z/M, \lambda) = \frac{x}{M} \prod_{m} \frac{1 - \frac{x^2}{c_m}}{1 - \frac{x^2}{c'_m}} \tag{3.74}$$

The approximation may be stated as in the following box:

The Zolotarev sign function applies over a designated range $[r_1, r_2]$ and approximation order N. Then if N is even let, $N_n = N/2 - 1$ and $N_d = N/2$, otherwise if N is odd, let $N_n = (N-1)/2$ and $N_d = (N-1)/2$. Let the Zolotarev sign function be given by

$$\mathcal{Z}_{sgn}^{[r_1,r_2]}(r) = \mathcal{Z}_{sgn}^{[1,\beta]}(x) = mx \frac{\prod_{m=1}^{N_n} 1 - \frac{x^2}{c_m}}{\prod_{m=1}^{N_d} 1 - \frac{x^2}{c'_m}} \tag{3.75}$$

where $\beta = \frac{r_2}{r_1}$ and $x = \frac{r}{r_1}$. Then we have the factored expression

$$\mathcal{Z}_{\text{sgn}}^{[r_1,r_2]}(r) = dr \frac{\prod_{m=1}^{N_n} (a_m - r^2)}{\prod_{m=1}^{N_d} (d_m - r^2)} \tag{3.76}$$

with $d = \frac{m}{r_1}\frac{\prod_{m=1}^{N_d} r_1^2 c'_m}{\prod_{m=1}^{N_n} r_1^2 c_m}$, $a_m = r_1^2 c_m$, $d_m = r_1^2 c'_m$. Further, it can be expressed via a partial fraction decomposition

$$\mathcal{Z}_{\text{sgn}}^{[r_1,r_2]}(r) = dr(b_0 + \sum_{m=1}^{N_d} \frac{b_m}{r^2 + d_m}) \tag{3.77}$$

where b_m must be evaluated and d_m are the denominators of the factored expression.

Calculation of the Zolotarev sign function coefficients is then carried out as follows:

Set range parameters

$$\begin{aligned} k &= \frac{1}{\beta} \\ k' &= \sqrt{1-k^2} \end{aligned} \tag{3.78}$$

$$\Delta = K'/N \tag{3.79}$$

Set complete elliptic integrals

$$\begin{aligned} K &= \int_0^1 \frac{dt}{(1-t^2)(1-k^2t^2)^{1/2}} \\ K' &= \int_0^1 \frac{dt}{(1-t^2)(1-k'^2t^2)^{1/2}} \end{aligned} \tag{3.80}$$

Set constants

$$m = \frac{2\lambda}{1+\lambda}\frac{1}{M} \tag{3.81}$$

$$M = R(1) \tag{3.82}$$

$$C = \frac{\text{sn}(K,k)\text{sn}(\Delta,k')}{1-\text{dn}^2(K,k)\text{sn}^2(\Delta,k')} \tag{3.83}$$

$$\lambda = \frac{M}{C\ R(C^2)} \tag{3.84}$$

where

$$R(x) = \frac{\prod_{m=1}^{N_n} 1 - \frac{x}{c_m}}{\prod_{m=1}^{N_d} 1 - \frac{x}{c'_m}} \tag{3.85}$$

and

$$\begin{aligned} c_m &= \frac{-\text{sn}^2(2m\Delta,k')}{1-\text{sn}^2(2m\Delta,k')} \\ c'_m &= \frac{-\text{sn}^2((2m-1)\Delta,k')}{1-\text{sn}^2((2m-1)\Delta,k')} \end{aligned} \tag{3.86}$$

Fig. 3.4 shows the errors of the two approximations. The Zolotarev errors are, in a

sense, uniform across the specified range, whereas the HT errors, while very small around $x = 1$ struggle with large errors away from unity. In fig. 3.5 we see the distribution of denominator coefficients of the two approximations. The left panel shows the strong clustering and narror range of the HT method contrasting with the much wider range of the and more even spread of the Zolotarev method.

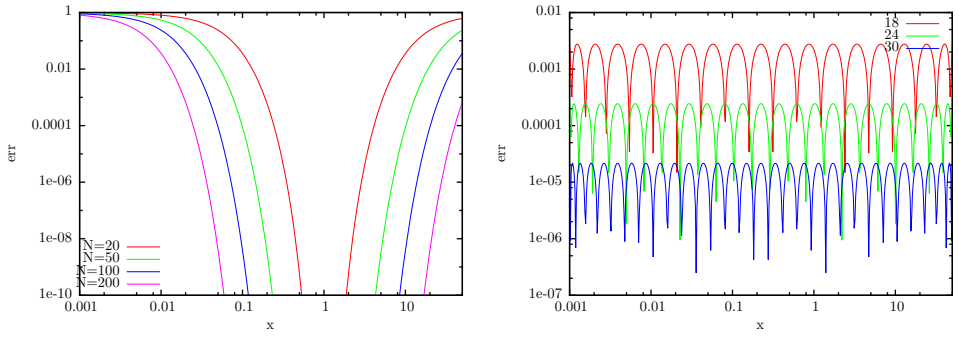

FIGURE 3.4: Errors for approximations to sign function. Left panel: HT. Right panel: Zolotarev.

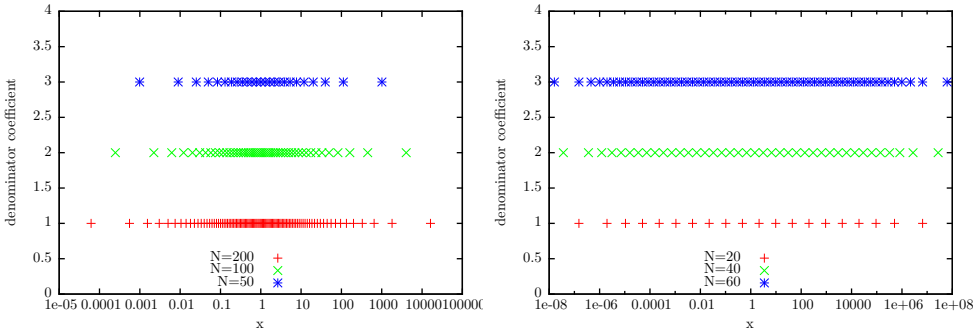

FIGURE 3.5: Distribution of denominator coefficients for approximations to the sign function with different n. Note the wide difference in x-axis ranges. Left panel: Hyperbolic tanh. Right panel: Zolotarev approximation.

The domain wall formulation requires knowledge of u_j, the roots of $\mathcal{Z}_{\text{sgn}}^{[r_1,r_2]}(x) - 1$. The extrema and roots are calculated via

Extrema: For $m \in (1, \ldots, N+1)$

$$x_m = r_1(1 - k'^2 \mathrm{sn}^2((m-1)\Delta, k')^{-1/2} \tag{3.87}$$

Roots: For $m \in (1, \ldots, N)$

$$\begin{aligned} y_0 &= M\mathrm{sn}^{-1}(\sqrt{\frac{1+3\lambda}{(1+\lambda)^3}}, \lambda') \\ y_m &= (-1)^{m-1} y_0 + 2[\frac{m}{2}]\Delta \end{aligned} \tag{3.88}$$

$$x_m = r_1(1 - k'^2 \mathrm{sn}^2(y_m, k'))^{-1} \tag{3.89}$$

where $[\frac{m}{2}]$ is the lowest integer value and asn is the inverse of the Jacobi elliptic sine function.

Fig. 3.6 shows error plots, extrema and root locations over an exemplary range.

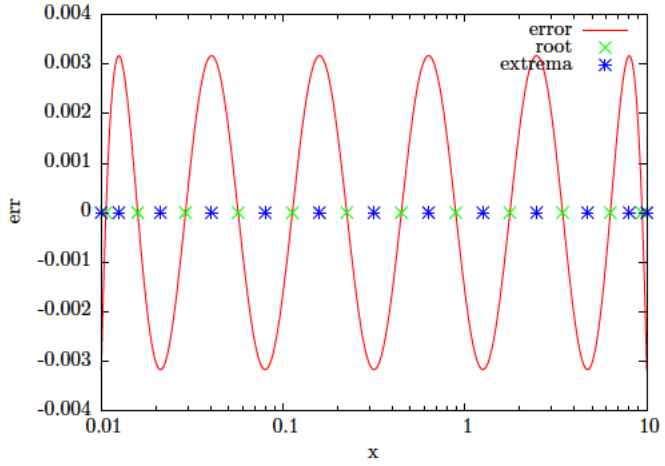

FIGURE 3.6: Roots and extrema of the Zolotarev approximation with $N = 12$.

The Zolotarev algorithm was optimal across the ranges $[-r_2, -r_1]$ and $[r_1, r_2]$. We may further seek an optimal rational function across just $[r_1, r_2]$. The Remez algorithm is an iterative technique, also based on Chebyshev's theorem, which has no requirement that the function be odd, and will find more optimal solutions should they exist. As it turns out, it seems that the Remez algorithm does identically give the optimal Zolotarev solution, and no improvement.

3.9 Relation Between Domain Wall and Overlap

The equivalence of the domain wall and overlap formulations was understood from the beginning. Early in the development of the overlap operator it was noted [33] that the domain wall of [21] could be developed from their formalism. We show the formal equivalence of the methods via their shared determinant in appendix A.3 following [39] and [35]. Below we just quote the most pertinent relations from [40] to highlight the full matrix equivalence. With the compacting matrix

$$C = \begin{pmatrix} P_- & P_+ & 0 & 0 \\ 0 & P_- & P_+ & 0 \\ 0 & 0 & P_- & P_+ \\ P_+ & 0 & 0 & P_- \end{pmatrix}, C^\dagger = C^{-1} = \begin{pmatrix} P_- & 0 & 0 & P_+ \\ P_+ & P_- & 0 & 0 \\ 0 & P_+ & P_- & 0 \\ 0 & 0 & P_+ & P_- \end{pmatrix} \tag{3.90}$$

we have

$$K_{DW} = C^\dagger D_{DW}^{-1}(1) D_{DW}(m) C = \begin{pmatrix} D_{OL}(m) & 0 & 0 & 0 \\ -(1-m)\triangle_2^R & 1 & 0 & 0 \\ -(1-m)\triangle_3^R & 0 & 1 & 0 \\ -(1-m)\triangle_4^4 & 0 & 0 & 1 \end{pmatrix} \tag{3.91}$$

[35] has further shown the equivalence for the twisted mass terms. It is important to note that the twisted mass formulation is not used for the Pauli-Villars terms, so that

$$K_{DW}^{M3} = C^\dagger D_{DW}^{-1}(1) D_{DW}^{M3}(m) C \tag{3.92}$$

Hence $(K_{DW}\Psi)_1 = D_{OL}\psi$ when $\Psi = \{\psi, 0, \cdots, 0\}$ and since we have

$$(K_{DW}^{M3})^{-1} = C^\dagger (D_{DW}^{M3})^{-1}(m) D_{DW}(1) C \tag{3.93}$$

we may also calculate the inverse of the overlap operator indirectly with $(K_{DW}^{-1}\Psi)_1 = D_{OL}^{-1}\psi$. We sometimes refer to these calculations as indirect calculation of the overlap operator rather than calculation of the domain wall operator.

3.10 Further Formulations

There are alternative algebraic formulations using an extra "dimension" and exploiting the Shur complement to achieve the same evaluation of the overlap operator [39]. Although we don't explore them further it is useful to be aware of them. The Schur

complement of a block matrix is defined via its LDU decomposotion $M = LDU$, to be the bottom right element of the D component

$$M = \begin{pmatrix} A & B \\ C & D \end{pmatrix} = \begin{pmatrix} I & 0 \\ CA^{-1} & I \end{pmatrix} \begin{pmatrix} A & 0 \\ 0 & D - CA^{-1}B \end{pmatrix} \begin{pmatrix} I & A^{-1}B \\ 0 & I \end{pmatrix} \tag{3.94}$$

This is given by

$$\mathcal{S} = D - CA^{-1}B \tag{3.95}$$

and has the property that $\det(M) = \det(A)\det(D - CA^{-1}B)$.

We may indirectly evaluate the partial fraction formulation $\text{sign}(H) = \sum_{j=1}^{n} \frac{a_j H}{H^2 - d_j^2}$ using

$$\begin{pmatrix} \frac{\gamma_5 D_W}{a_1} & 1 & 0 & 0 & 1 \\ 1 & \frac{a_1 \gamma_5 D_W}{d_1^2} & 0 & 0 & 0 \\ 0 & 0 & \frac{\gamma_5 D_W}{a_2} & 1 & 1 \\ 0 & 0 & 1 & \frac{a_1 \gamma_5 D_W}{d_2^2} & 0 \\ -1 & 0 & -1 & 0 & R \end{pmatrix} \tag{3.96}$$

which has the Schur complement

$$R + \frac{a_1 \gamma_5 D_W}{D_W^\dagger D_W - d_1^2} + \frac{a_2 \gamma_5 D_W}{D_W^\dagger D_W - d_2^2} \tag{3.97}$$

There is also a continued fraction formulation

$$\text{sign}(\gamma_5 D_W) = \beta_0 \gamma_5 D_W + \cfrac{1}{\beta_1 \gamma_5 D_W + \cfrac{1}{\beta_2 \gamma_5 D_W + \cfrac{1}{\beta_3 \gamma_5 D_W}}} \tag{3.98}$$

which is the Schur complement of

$$\begin{pmatrix} \beta_3 \gamma_5 D_W & 1 & 0 & 0 \\ 1 & \beta_2 \gamma_5 D_W & 1 & 0 \\ 0 & 1 & \beta_1 \gamma_5 D_W & 1 \\ 0 & 0 & 1 & \beta_0 \gamma_5 D_W \end{pmatrix} \tag{3.99}$$

Chapter 4

Bilinear Condensate

The bilinear condensate $\langle\bar{\psi}\psi\rangle$ is the primary measurement of this work, and we will use calculations of it to look for the critical coupling, β_c, in the lattice Thirring model, taking $m \to 0$, and to find critical exponents characterising the behaviour of the condensate in the vicinity of the critical point. The suitability of the different variants set out in this chapter will be explored in the results chapters.

4.1 Measurements

We start by introducing some useful notation. With $D \equiv D[U]$, we define the brackets $\langle\cdot\rangle_F$ and $\langle\cdot\rangle_G$ with integrals

$$\langle O\rangle_F \equiv \int \mathcal{D}[\Psi,\bar{\Psi}]O[\Psi,\bar{\Psi}]\exp(-\bar{\Psi}D\Psi) \tag{4.1}$$

$$\langle O\rangle_G \equiv \int \mathcal{D}[U]\exp(-S_G[U])O[U] \tag{4.2}$$

We then have the fermionic part of the partition function

$$Z_F \equiv \langle 1\rangle_F = \int \mathcal{D}[\Psi,\bar{\Psi}]\exp(-\bar{\Psi}D\Psi) = \det[D] \tag{4.3}$$

and the full interacting partition function

$$Z = \langle Z_F\rangle_G = \int \mathcal{D}[U]\exp(-S_G[U])\det[D] \tag{4.4}$$

Our measurements will then be of the form

$$\langle O \rangle = \frac{1}{Z} \langle \langle O \rangle_F \rangle_G \tag{4.5}$$

which defines our use of the bracket $\langle \cdot \rangle$.

4.2 Bilinear Condensate

We are most interested in the bilinear condensate, $C = \langle \bar{\psi}\psi \rangle$, herein referred to as just the condensate. The condensate is the order parameter we choose for the Thirring model. It is zero in the unbroken phase and non-zero in the broken phase. The continuous but non-smooth change occurs at the critical coupling strength. The condensate is defined by the derivative of the free energy[1] wrt the symmetry-breaking parameter, and is given by

$$C \equiv \frac{\partial \ln Z}{\partial m} \tag{4.6}$$

Noting that in general[2]

$$\frac{\partial \ln Z}{\partial m} = \frac{1}{Z} \langle \frac{\partial Z_F}{\partial m} \rangle_G \tag{4.7}$$

and since for Dirac operators linear in mass which we again split according to $D = D^0 + mD^m$ we have

$$\frac{\partial Z_F}{\partial m} = \langle \bar{\psi} D^m \psi \rangle_F \tag{4.8}$$

and hence we find that the condensate may be equivalently expressed as

$$C \equiv \langle \bar{\psi} D^m \psi \rangle \tag{4.9}$$

To evaluate this we require

$$\frac{\partial Z_F}{\partial m} = \langle \mathrm{Tr}[D^m D^{-1}] \det[D] \rangle \tag{4.10}$$

and from here we use the Monte Carlo integration[3] with

[1] By analogy to classical statistical mechanics in which the Helmholtz free energy $F(T) \propto \ln Z(T)$
[2] Derivations of equations in this section are given in appendix A.5
[3] As set out in appendix B.1.

$$C = \frac{1}{N}\sum_i \mathrm{Tr}[D^m[U_i]D^{-1}[U_i]] \tag{4.11}$$

We observe in passing that the mass term in the Shamir domain wall formulation is independent of U. We now turn to the particular forms for the overlap and domain wall operators.

4.3 Overlap Condensate

We distinguish two mass variants of the overlap operator, the standard mass and the γ_3 twisted mass formulation, given in section 3.7, and again separate the mass terms from the non mass terms with the notation given in eqn. 4.12. The indices $j = 1$ corresponds to the standard mass term and $j = 3$ the twisted mass term so that

$$D^j_{OL} = D^0_{OL} + mD^{Mj}_{OL} \tag{4.12}$$

in which we have the mass terms

$$\begin{aligned} D^0_{OL} =& \frac{1}{2} + \frac{1}{2}V \\ D^{M1}_{OL} =& \frac{1}{2} - \frac{1}{2}V \\ D^{M3}_{OL} =& \frac{i\gamma_3}{2} - V\frac{i\gamma_3}{2} \\ V =& \gamma_3 \mathrm{sgn}[H] \end{aligned} \tag{4.13}$$

H is given by either the Wilson kernel $H_W = \gamma_3 D_W$ or the Shamir kernel $H_S = \gamma_3 D_W(2 + D_W)^{-1}$. The trace terms to evaluated for the condensate are then given by

$$\tilde{C}^1_{OL} = \mathrm{Tr}[D^{M1}_{OL}(D^1_{OL})^{-1}] = \mathrm{Tr}[\frac{1}{1-m}((D^1_{OL})^{-1} - 1)] \tag{4.14}$$

$$\tilde{C}^3_{OL} = \mathrm{Tr}[D^{M3}_{OL}(D^3_{OL})^{-1}] = \mathrm{Tr}[\frac{-1}{i\gamma_3 + m}((D^3_{OL})^{-1} - 1)] \tag{4.15}$$

We note that a left handed formulation with the twisted mass gives the same condensate even though $D^{M3}_{OL}(D^3_{OL})^{-1} \neq D^{M4}_{OL}(D^4_{OL})^{-1}$ where

$$D^{M4}_{OL} = \frac{i\gamma_3}{2} - \frac{i\gamma_3}{2}V \tag{4.16}$$

These formulations are unaffected by the choice of kernel, and derivations are given in appendix A.5.

4.4 Domain Wall Condensates

For the domain wall formulation, the trace is more complicated due to the splitting of the fermion onto opposite walls. Also, the formulation is dependent not only on the mass term but also on the choice of kernel. The different fomulations have already been described for splitting and we again use the notation $D^j_{DW} = D^0_{DW} + mD^{Mj}_{DW}$ with subscript DW replaced with SDW for Shamir formulations and WDW for Wilson formulations, and the superscript j again corresponds to the mass formulation. In each case the M matrix corresponds the domain wall operator, so for example in eqn. 4.17 $M = D^1_{SDW}$. The subscript indices indicate the submatrix of the extra dimension, as illustrated in eqn. 3.42 for example. The variant components are defined in section 3.6. Then we have traces for the Shamir kernel given by

$$\mathrm{Tr}[D^{M1}_{SDW}(D^1_{SDW})^{-1}] = -(\mathrm{Tr}[P_+(M^{-1})_{N1}] + \mathrm{Tr}[P_-(M^{-1})_{1N}]) \tag{4.17}$$

$$\mathrm{Tr}[D^{M3}_{SDW}(D^3_{SDW})^{-1}] = -i(\mathrm{Tr}[P_+M^{-1}_{N,1}] - \mathrm{Tr}[P_-M^{-1}_{1,N}]) \tag{4.18}$$

And for the Wilson kernel we have

$$\mathrm{Tr}[D^{M1}_{WDW}(D^1_{WDW})^{-1}] = (\mathrm{Tr}[(\omega_1 D^{\|} - I)P_+M^{-1}_{N,1}] + \mathrm{Tr}[(\omega_N D^{\|} - I)P_-M^{-1}_{1,N}]) \tag{4.19}$$

$$\mathrm{Tr}[D^{M3}_{WDW}(D^3_{WDW})^{-1}] = i(\mathrm{Tr}[(\omega_1 D^{\|} - I)P_+M^{-1}_{N,1}] - \mathrm{Tr}[(\omega_N D^{\|} - I)P_-M^{-1}_{1,N}]) \tag{4.20}$$

Derivations of these are given in [44].

Chapter 5

Thirring Model in 2+1D

The Thirring model [45] was introduced as a toy relativistic model with an analytic solution in 1+1d. With considerable current industrial interest in planar materials such as graphene, understanding of the 2+1d case is of interest both as toy model and is of relevance to the commercial world. However, there is no analytic solution in 2+1d, and odd dimensioned theories have significantly different properties to their even numbered counterparts. The model may be further considered a stepping stone towards understanding strongly coupled QED in 2+1d. It has been suggested [3] that this is the simplest relativistic fermi model which necessitates numerical techniques for the exploration of the strongly coupled sector where perturbative approaches don't work.

The Euclidean continuum formulation of the Thirring model for a single fermion field, in which the current density $J_\mu = i\bar{\psi}\gamma_\mu\psi$ is conserved, so that $\frac{\partial J_\mu}{\partial x_\mu} = 0$, is given by [46]:

$$S[\psi,\bar{\psi}] = \int d^3x \bar{\psi}(\gamma_\mu\partial_\mu + m)\psi + \frac{g^2}{2}(\bar{\psi}\gamma_\mu\psi)^2 \tag{5.1}$$

It has a global $U(2)$ symmetry with mass terms explicitly breaking this to $U(1)\otimes U(1)$ as set out in section 3.1. The self interacting term may be reformulated (see appendix A.4) with an auxiliary field so that we have $S[\psi,\bar{\psi}] = S_F[\psi,\bar{\psi},A] + S_G[A]$, where the fermionic action takes the form of the usual gauge invariant Dirac term although the Thirring action $S_G[A]$ is *not* gauge invariant:

$$S_F[\psi,\bar{\psi},A] = \int d^3x \bar{\psi}(\gamma_\mu(\partial_\mu + iA_\mu) + m)\psi \tag{5.2}$$

$$S_G[A] = \frac{1}{2g^2}\int d^3x A_\mu^2 \tag{5.3}$$

This formulation allows the Monte Carlo integration technique already introduced (eqn. 2.18) to be used in calculations. After discretisation we have the dimensionless coupling

strength parameter $\beta = a/g^2$. We keep the lattice spacing fixed at $a = 1$ and will vary β in its stead.

We will will seek fixed point parameter values, described in the next section, in the lattice theory parameter space[1]. In the case of the Thirring model, we have two parameters[2] m and β. We a priori know that $m_f = 0$ and will seek β_f. Fixed points correspond to continuum theories, that is taking $a \to 0$, although methodologically we will control a through β. If $0 < \beta_f < \infty$ then it is a critical coupling, $\beta_c = \beta_f$, and it is associated with a phase transition. At such a phase transition there may be an observable which changes phase.[3] Such an observable is an order parameter and we wish to characterize that order parameter. Lumping together [47] higher order forms[4] from Ehrenfest's classification of phase transitions, we distinguish between first order phase transitions wherein the order parameter is discontinuous at the critical point, and continuous phase transitions in which some higher derivative of the order parameter is discontinuous. The characterisation will be with power law functions (functions of the form $f(a, b) = a^\alpha b^\beta$) expressed in an equation of state (EoS) around the critical point. For the Thirring model we will concentrate on the condensate $C = \langle\bar{\psi}\psi\rangle$ as the order parameter and will seek some form $C(m, \beta)$ which holds close to the critical point. To this end we continue on a path set out in the 90s with the Gross-Neveu model [48], and later the Thirring model [2], and will utilise the EoS developed therein.

The change in order parameter at the critical point is caused by the breaking of some symmetry and is called spontaneous symmetry breaking.

Early numerical work on the 2+1d Thirring model was carried out with staggered fermions [49]. More recent work has included SLAC fermions [4], and domain wall fermions [50]. A summary of related work in the area is provided in [6]. Somewhat problematically, the different methods have found different critical flavour numbers. Simulations with staggered formulations lead to $3 < N_c < 4$, and the SLAC formulations have $N_c < 1$. Domain wall results indicate $1 < N_c < 2$. In this work we continue with the domain wall/overlap formulation, motivated by the intention to capture the $U(2)$ symmetry on the lattice, in contrast to staggered fermions which break from $U(1) \otimes U(1) \to U(1)$, but also with a local formulation in contrast to the SLAC fermions.

5.1 Fixed Points, Power Laws, and Critical Exponents

Although it is usual to consider the lattice spacing fixed in lattice calculations, it is intuitive to consider the continuum from the $a \to 0$ limit. As the lattice spacing a

[1] The parameter space is just the set of lattice theories covering all possible values of the parameters.
[2] We have already specified the number of fermions, $N_f = 1$, and do not consider it a parameter here.
[3] The critical point of water is a counter example of this.
[4] The lowest order of discontinuous derivative gave the classification order.

varies, if the parameters of the theory are fixed, β and m in our Thirring model, the physical measurables will change. That is to say, changing the lattice spacing changes the physical theory. For small enough a, to keep the same physical theory we must change the parameters in accordance with a. That is we require $\beta \equiv \beta(a)$, and $m \equiv m(a)$. To be independent of this change requires $\frac{\partial \beta}{\partial a} = 0$ which defines a fixed point[5]. We will find this fixed point in the continuum limit as $a \to 0$. Thus we are saying that at a fixed point the constants of the theory (which govern the physics) are independent of the lattice scale. This is equivalent to the usual perturbative renormalization process [48]. In the Thirring model we have the critical parameters $m_c = 0$ and we want to find β_c.

A consequence of scale independence is that ratios of measurements at corresponding ratios of scales should be equal. Denoting a measurement $\mathcal{M}$ using a lattice lagrangian $\mathcal{L}[\beta]$ with a single parameter β (ignoring m for illustration), close to a critical value $\beta = \beta_c$, this can be expressed as (with the colon : meaning such that)

$$\frac{\mathcal{M}[\mathcal{L}(\beta : \beta - \beta_c = c)]}{\mathcal{M}[\mathcal{L}(\beta : \beta - \beta_c = \alpha c]} = \frac{\mathcal{M}[\mathcal{L}(\beta : \beta - \beta_c = d)]}{\mathcal{M}[\mathcal{L}(\beta : \beta - \beta_c = \alpha d]} \tag{5.4}$$

$\mathcal{M}$ can then be expressed as a power law $\mathcal{M} \propto (\beta - \beta_c)^\delta$ since if $\frac{f(a)}{f(\alpha a)} = \frac{f(b)}{f(\alpha b)}$ then $f(x) \propto x^\delta$. Since we can find this power law through curve fitting we can then extrapolate to find the measurement of the continuum limit.

In the region around a system with dimensionless critical coupling value β_c, the hyperscaling hypothesis [51] asserts that the only significant parameter is a length scale ξ of the order parameter. For the Thirring model we use the condensate as the order parameter. Letting $\Sigma(x) = \bar{\psi}(x)\psi(x)$, $\Sigma = (\sum_x \Sigma(x))/V$, the condensate may be expressed as $C = \langle \Sigma \rangle$, and we define the associated correlation length ξ such that for large $|x - y| \gg \xi$:

$$\langle \Sigma(x)\Sigma(y) \rangle \propto \frac{1}{|x-y|^p} e^{-|x-y|/\xi} \tag{5.5}$$

Then the length scale has an associated power law with exponent ν as the critical coupling strength is approached.

$$\xi \propto |\beta - \beta_c|^{-\nu} \tag{5.6}$$

However, it is divergent at β_c. At the critical coupling the correlator takes a pure power law form

[5] Note this not the beta function relating coupling strength to energy scale.

$$\langle \Sigma(x)\Sigma(y)\rangle \propto \frac{1}{|x-y|^{d-2-\eta}} \tag{5.7}$$

which defines another critical exponent η. These two critical exponents are the physical properties of the system that are the ultimate goal of our calculations. Given the divergence of the length scale at the critical coupling we must work with calculations in the vicinity of the critical coupling. It is easier to calculate the order parameter than the diverging length scale directly, and we shall do this in conjunction with an equation of state in order to evaluate the critical exponents.

5.2 Equation of State

From RG equation reasoning [2] we have the general macroscopic equation

$$H(M,t,1) \sim M^{\delta}\mathcal{F}(tM^{-1/\beta_m}) \tag{5.8}$$

where H is some field that breaks the symmetry explicitly, M is the order parameter broken at the critical point, t is the distance from the critical point, $\mathcal{F}$ is a universal scaling function, and the 1 in H refers to the lattice regularization. For the Thirring model, the external force H, is replaced with the mass m, the order parameter M is the bilinear condensate $\langle\bar{\psi}\psi\rangle$, and the coupling strength $\beta = a/g^2$ is the critical parameter, so $t = \beta - \beta_c$. Then we have

$$m = \langle\bar{\psi}\psi\rangle^{\delta}\,\mathcal{F}[(\beta-\beta_c)\langle\bar{\psi}\psi\rangle^{-1/\beta_m}] \tag{5.9}$$

and after taking the Taylor expansion of $\mathcal{F}$ we have the equation of state (EoS)

$$m = A(\beta-\beta_c)\langle\bar{\psi}\psi\rangle^{\delta-1/\beta_m} + B\langle\bar{\psi}\psi\rangle^{\delta} \tag{5.10}$$

in which $A = \mathcal{F}(0)$ and $B = \mathcal{F}'(0)$. Considering the line $m = 0$, and since $\langle\bar{\psi}\psi\rangle^{\delta} \neq 0$ in the broken phase, we have $\mathcal{F}[(\beta-\beta_c)\langle\bar{\psi}\psi\rangle^{-1/\beta_m}] = 0$, and hence

$$(\beta-\beta_c)\langle\bar{\psi}\psi\rangle^{-1/\beta_m} \sim const \tag{5.11}$$

Clearly, at the critical coupling we have $\beta - \beta_c = 0$, so

$$m \sim \langle\bar{\psi}\psi\rangle^{\delta} \tag{5.12}$$

We can relate δ and β_m back to ν and η via the hyperscaling relations, with $d = 3$:

$$\beta_m = \frac{1}{2}\nu(d - 2 + \eta) = \frac{1}{2}\nu(1 + \eta) \tag{5.13}$$

$$\delta = \frac{d + 2 - \eta}{d - 2 + \eta} = \frac{5 - \eta}{1 + \eta} \tag{5.14}$$

and hence

$$\eta = \frac{5 - \delta}{1 + \delta} \tag{5.15}$$

$$\nu = \frac{2\beta_m}{1 + \eta} \tag{5.16}$$

For Dirac operators which have the same physical content, we would expect the calculated critical exponents to be the same. Hence the choice of Wilson or Shamir kernel should yield the same critical exponents, and that calculation and comparison is one of the objectives of this work. If so there should be some relation between $m_w = \mathrm{EoS}(\beta_w, C_w(m_w, \beta_w))$ and $m_s = \mathrm{EoS}(\beta_s, C_s(m_s, \beta_s))$ so that for some functions f, and g,

$$\begin{aligned} m_s &= f(m_w, \beta_w) \\ \beta_s &= g(m_w, \beta_w) \end{aligned} \tag{5.17}$$

Rather than seeking critical exponents according to an equation of state [52] considers more general space of four fermi models, including Gross-Neveu interactions $(\bar{\psi}\psi)^2$, Thirring interactions $(\bar{\psi}\gamma_\mu\psi)^2$ as well as $(\bar{\psi}\gamma_{35}\psi)^2$ and $(\bar{\psi}\gamma_{\mu\nu}\psi)^2$ and looks at a network of fixed points in the parameter space. Should our results not match it could be indicative that such a wider model space is required in which to find a continuum theory. The magnitude of the discrepancy might also measure the magnitude of the required correction.

Uniqueness of universality class implied by locality [53] suggests different discretisations should have the same continuum limit, but in a space with a multitude of fixed points it is difficult to ensure different algorithms converge to the same fixed point.

5.3 Quenched Generation of Auxiliary Fields and the Choice of Measure

We want to generate an ensemble of auxiliary fields so that we can use the Monte Carlo integration calculation of eqn. 2.18. However, the determinant of the Dirac operator in the probability density function, eqn. 2.19, is very costly, and some insight can be garnered simply assuming $\det[D] = 1$. This is the quenched approach, and then we are interested in the quenched auxiliary measure

$$\int \mathcal{D}[A] \exp(-S_G[A]) \tag{5.18}$$

which, for the Thirring model with Riemannian measure, eqn. 2.16, and with $A_k \equiv A_{i,\mu}$, is given by

$$\prod_k \sqrt{\frac{\beta}{2\pi}} \int_{-\infty}^{\infty} dA_k e^{-\frac{\beta}{2}A_k^2} \tag{5.19}$$

So our sequence of auxiliary fields A^n may be generated with each value being an independent gaussian random number $A_k^n \sim \mathcal{N}(0, \frac{1}{\beta})$. This is the non-compact measure. A compact (unnormalised) measure [54] is given by

$$\prod_k \int_{-\pi}^{\pi} dA_k e^{\beta[\cos(A_k)-1]} \tag{5.20}$$

for which we require our sample A_k to be taken from the probability density function $e^{\beta[\cos(A_k)-1]}/N$ where $N = \int_{-\pi}^{\pi} dx\, e^{\beta[\cos(x)-1]}$.

However, for a fermion measurement, we use either non-compact links $U_k = 1 + iaA_k$, eqn. 2.7, or compact links, $U_k = e^{iaA_k}$, eqn. 2.8, transforming A to U for use in Dirac operators, denoted $D[U_{NC}]$ or $D[U_C]$.

In true gauge field theories we want the link fields to be unitary, $U(1)$, to ensure gauge invariance on the lattice and hence the compact formulation is natural. It is appropriate to use the compact measure with compact links. However, this introduces $O(a)$ terms into the naive lattice fermion action [10]. Since the auxiliary field of the Thirring model is not gauge invariant there is no reason to force a $U(1)$ link and so it seems natural to use the non-compact link formulation for which no additional terms are found in the lattice fermion action. Further, there are no lattice artifacts in the bosonic action of order higher than the intended A_μ^2 term when using the non-compact link. Accordingly the non-compact measure is appropriate. There is plenty of precedent in the literature [3, 5] for this. However, compact links and measures have also been explored with the

Thirring model [54]. We are primarily interested in the non compact, but will touch on the compact as well in our calculations.[6]

It is worth pointing out that at first glance it seems that any derivative of the compact or non compact links should be the same in the $a \to 0$ limit, and indeed in the weakly coupled limit, where A_k is small, $U_C|^{a\to 0}_{\beta\to\infty} = U_{NC}|^{a\to 0}_{\beta\to\infty}$, the Dirac operators are the same, $D[U_C] = D[U_{NC}]$, and the compact and non compact measures are equivalent. However, away from the weakly coupled region this is not the case and they constitute distinct formulations.

[6] We note that the RHMC algorithm to be described in the next chapter is only formally proven for the compact case.

Chapter 6

Dynamic Fermions

While quenched fermions have been studied extensively in the past, that was largely due to the computational challenge of *dynamic* fermions, for which the $\det[D] = 1$ assumption is not made. We will distinguish between the *valence* fermions - that is the Dirac operator used to calculate measurements - and *sea* fermions - the Dirac operator used in the generation of the auxiliary fields. Compromising between quenched and dynamic fermions we may use different Dirac operators for each calculation. If they are not the same, then the measurements are considered *partially quenched*. The primary reason to do this, similarly to full quenching, is to accelerate the calculation. At best this may be viewed as two calculationally inconsistent methods for different parts of the overall calculation, and at worst as being a non-physical calculation. Nevertheless it is an established practice; partially quenched simulations in QCD have been carried out with regular Wilson fermions for the sea components, and domain wall valence fermions for example. Changing the mass term has also been tested [10], although [55] gives an example where the condensate measured using massively generated gauge fields in the $m \to 0$ limit erroneously remained non-zero.

Since we want to calculate the integral eqn. 2.14 with Monte Carlo integration, and we cannot simply generate the auxiliary fields via the distribution functions allowed by the quenched formulation, alternative methods must be found. Such methods include Markov chain, classical dynamics, and langevin (stochastic dynamics) methods [19, 39], but perhaps the currently most used method is the hybrid Monte Carlo method [56], taking aspects of classical dynamics and the Markov methods. The rational hybrid Monte Carlo [57] (RHMC) method allows for the calculation of any number of fermion fields rather than the necessarily even number of fermion fields of the original hybrid Monte Carlo (HMC) method.

6.1 Markov Chain Monte Carlo Generation of Auxiliary Fields

We want to generate a sequence of independent auxiliary fields A from which to derive the Dirac operator link fields U used in the Monte Carlo integration of our lattice measurement, eqn. 2.18. For a given action $S[A]$, we want to find a distribution A with probability distribution $P[A] \propto e^{-S[A]}$. This is done via Markov chain $(A_0, \ldots, A_N)$. The essence of a Markov chain is simply that the generation of the next stochastic variable in the sequence is dependent only on the previous value and not the entire time history. [39] gives more details and proofs of the underlying maths, but the resulting *Metropolis* algorithm is

1. Choose A_0.
2. Loop for $n = 1, N$
   - Choose some A', according to any probabilistic rule which ensures that all allowable A fields may be achieved after a finite number of steps (this is *ergodicity*).
   - Assign A^n according to

$$A^n = \begin{cases} A' & \text{with probability } \min\{1, \exp(-S[A'] - S[A^{n-1}])\} \\ A^{n-1} & \text{otherwise} \end{cases}$$

For N large enough, A_N will take the specified distribution $\propto e^{-S[A]}$, regardless of the choice of A_0 and we have created an independent A field for the Monte Carlo integration. To ensure the convergence of the A^N field to a fixed probability distibution, it suffices to have *detailed balance*, also called *time reversibility*. Some more details are given in appendix B.2. In practice one does not choose a new initial field A_0 for each new field to be generated, and we take our fields from a single extended Markov chain. Further, the fields extracted from this chain may be correlated but there are methods available to work with correlated data.

6.2 Hybrid Monte Carlo Generation of Auxiliary Fields

We want a good way to choose A'. The most utilized method is currently to adopt a non-physical hamiltonian dynamics step, specifying the hamiltonian $H = \frac{1}{2}P^2 + S[A]$, and then march according to

$$\dot{A} = \frac{\partial H}{\partial P} = P \tag{6.1a}$$

$$\dot{P} = -\frac{\partial H}{\partial A} = -\frac{\partial S[A]}{\partial A} \tag{6.1b}$$

The time marching scheme must be time reversible to satisfy detailed balance. Further *symplectic* integrators are bound to surfaces of constant H to within discretisation errors. To this end the leapfrog method[1] is used to discretise the time marching. Here that is if A is evaluated at $t = i\triangle t$, then P is evaluated at $t = (i + 1/2)\triangle t$. It is possible to evaluate the *force* term, $\dot{P}$, when we use an *effective* action $S_{eff}(A)$ which has real numbers rather than the Grassmann numbers of the original action. A^{n-1} is known at the beginning of each hamiltonian dynamics step, except for A^0 which must be set, either as a random distribution or fixed to zero. Each member of P must be set to a random gaussian distribution at the beginning of each step. This is the hybrid Monte Carlo method introduced in [56].

1. Choose A_0
2. Loop for $n = 1, N$
   (a) Initialise ϕ, and P_{start} with gaussian random variables.
   (b) Set $A_{start} = A_{n-1}$ and evaluate $H_0 = H(\phi, P_{start}, A_{start})$.
   (c) Loop for $t = 1, T$
      i. March P and A with leapfrog scheme.
      ii. Check if loop ends.
   (d) Evaluate $H_1 = H(\phi, P_{end}, A_{end})$
   (e) Monte Carlo acceptance step $A_n = A_{end}$ with probability $\min\{1, \exp(H^0 - H^1)\}$, otherwise $A_n = A_{n-1}$

Note however, now the probability in the acceptance step uses the artificial H rather than the original action S, since the fixed point distribution of the Metropolis algorithm now includes the hamiltonian momentum variables P. However, the marginal probability distribution of the auxiliary field remains $e^{-S[A]}$.

6.3 Effective Action and Pseudofermions

Again, we need to remove the Grassmann variables from eqn. 2.3. We will replace the fermionic action $S_F[\bar{\psi}, \psi, U]$ with an effective action $S_{eff}[\phi, U]$ which we can use with

[1] For the advection equation given by $\frac{q_i^{n+1} - q_i^{n-1}}{2\triangle t} + \frac{\partial q^n}{\partial x} = 0$

the HMC strategies [58].

Since the Grassmann integral can be recast (assuming M is positive definite) with complex valued pseudofermions ϕ via

$$\int \mathcal{D}[\psi,\bar{\psi}]\exp(-\bar{\psi}M\psi) = \int \mathcal{D}[\phi,\phi^\dagger]\exp(-\phi^\dagger M^{-1}\phi) \tag{6.2}$$

we will have the have partition function

$$Z = \int \mathcal{D}[A]\mathcal{D}[\phi,\phi^\dagger]\,\exp(-S_{eff}[\phi,A] - S_G[A]) \tag{6.3}$$

in which the effective action for 2 species of fermion is given by the real valued

$$S_{eff}[\phi,\phi^\dagger,U] = S_G[U] + \frac{1}{2}\phi^\dagger(D[U]^\dagger D[U])^{-1}\phi \tag{6.4}$$

We have used $M = (D[U]^\dagger D[U])^{-1}$ where we have exploited $\det[D[U]] = \det[D^\dagger[U]]$ to ensure positive semidefinite eigenvalues, since the eigenvalues of $\gamma_5 D[U]$ are real and $D[U]$ has γ_5-hermiticity. These attributes may not be true in general but are for operators satisfying the GW relations. For $N_f = 1$ we want

$$S_{eff}[\phi,\phi^\dagger,U] = S_G[U] + \frac{1}{2}\phi^\dagger(D[U]^\dagger D[U])^{-1/2}\phi \tag{6.5}$$

corresponding to partition function

$$Z = \int \mathcal{D}[U]\,\exp(-S_G[U])\det[(D^\dagger[U]D[U])]^{1/2} \tag{6.6}$$

ϕ is initialised at the beginning of each trajectory with complex gaussian distribution $P(\phi) \sim \exp(-\frac{1}{2}\phi^2)$.

6.4 Effective Domain Wall Action

Denoting the domain wall fermion operator with bare mass m, $M(m)$, and incorporating the Pauli-Villars components for the sea fermions gives $D[U] = M(m)M(1)^{-1}$ so letting the two fermion form be $D^\dagger D$, where we have dropped the explicit dependence on U, we have

$$
\begin{aligned}
Z &= \int \mathcal{D}[U] \exp(-S_G[U]) \det[M^\dagger(1)^{-1} M^\dagger(m) M(m) M(1)^{-1}]^{1/2} \\
&= \int \mathcal{D}[U] \exp(-S_G[U]) \det[(M^\dagger(1)M(1))^{-1/4} (M^\dagger(m)M(m))^{1/2} (M^\dagger(1)M(1))^{-1/4}]
\end{aligned}
\tag{6.7}
$$

Hence the effective action is given by

$$
S_{eff}[\phi, \phi^\dagger, U] = S_G[U] + \phi^\dagger (M^\dagger(1)M(1))^{\frac{1}{4}} (M^\dagger(m)M(m))^{-\frac{1}{2}} (M^\dagger(1)M(1))^{\frac{1}{4}}) \phi \tag{6.8}
$$

as given in [46].

6.4.1 Force Terms

We need to evaluate $\frac{\partial S}{\partial A_{x,\mu}}$, eqn. 6.1b, for the hamiltonian evolution step. The matrix derivative $\frac{dA^{-1}}{dt} = -A^{-1} \frac{dA}{dt} A^{-1}$ is useful in the following. In the Thirring model we have for the auxiliary field

$$
\frac{\partial S_G[A]}{\partial A_{x,\mu}} = \frac{2}{g^2} A_{x,\mu} \tag{6.9}
$$

For the fermionic term we have

$$
\begin{aligned}
\frac{\delta S}{\delta A_{x,\mu}} &= \phi^\dagger \frac{\delta (M^\dagger M(1))^{1/4}}{\delta A_{x,\mu}} (M^\dagger M(m))^{-1/2} (M^\dagger M(1))^{1/4} \phi \\
&\quad + \phi^\dagger (M^\dagger M(1))^{1/4} \frac{\delta (M^\dagger M(m))^{-1/2}}{\delta A_{x,\mu}} (M^\dagger M(1))^{1/4} \phi \\
&\quad + \phi^\dagger (M^\dagger M(1))^{1/4} (M^\dagger M(m))^{-1/2} \frac{\delta (M^\dagger M(1))^{1/4}}{\delta A_{x,\mu}} \phi \\
&= 2\mathrm{Re}[\phi^\dagger \frac{\delta (M^\dagger M(1))^{1/4}}{\delta A_{x,\mu}} (M^\dagger M(m))^{-1/2} (M^\dagger M(1))^{1/4} \phi] \\
&\quad + \phi^\dagger (M^\dagger M(1))^{1/4} \frac{\delta (M^\dagger M(m))^{-1/2}}{\delta A_{x,\mu}} (M^\dagger M(1))^{1/4} \phi
\end{aligned}
\tag{6.10}
$$

Denoting

$$\begin{aligned}\hat{\phi} =& (M^\dagger M(m))^{1/4}\phi \\ \bar{\phi} =& (M^\dagger M(m))^{-1/2}\hat{\phi}\end{aligned} \tag{6.11}$$

we have the much more benign looking

$$\frac{\delta S}{\delta A_{x,\mu}} = 2\mathrm{Re}[\phi^\dagger \frac{\delta (M^\dagger M(1))^{1/4}}{\delta A_{x,\mu}} \bar{\phi}] + \hat{\phi}^\dagger \frac{\delta (M^\dagger M(m))^{-1/2}}{\delta A_{x,\mu}} \hat{\phi} \tag{6.12}$$

The rational hybrid monte carlo method [57, 59] evaluates these fractional powers as partial fraction expansions, the coefficients of which are obtained with the Remez algorithm, an implementation of which is provided by [60]. We have the expansions

$$\begin{aligned}(M^\dagger M(m))^\alpha &= \alpha_0 + \sum_i \frac{\alpha_i}{M^\dagger M(m) + \beta_i} \\ \frac{\delta (M^\dagger M(m))^\alpha}{\delta A_{x,\mu}} &= \sum_i \alpha_i \frac{\delta}{\delta A_{x,\mu}} \frac{1}{M^\dagger M(m) + \beta_i}\end{aligned} \tag{6.13}$$

$$\frac{\delta}{\delta A_{x,\mu}} \frac{1}{M^\dagger M(m) + \beta_i} = (M^\dagger M(m) + \beta_i)^{-1} \frac{\delta (M^\dagger M(m) + \beta_i)}{\delta A_{x,\mu}} (M^\dagger M(m) + \beta_i)^{-1} \tag{6.14}$$

$$\frac{\partial (M^\dagger M(m) + \beta_i)}{\partial A_{x,\mu}} = M^\dagger(m) \frac{\partial M(m)}{\partial A_{x,\mu}} + \frac{\partial M^\dagger(m)}{\partial A_{x,\mu}} M(m) \tag{6.15}$$

Ultimately the domain wall force terms boil down to the force terms of Wilson Dirac operator. If the Wilson kernel of the domain wall formulation is being used, then extra force terms must be included to account for the off-diagonal terms in eqn. 3.45.

6.4.2 Dirac and Wilson Force Terms

We are looking for $\frac{\partial S_F[A]}{\partial A_\mu(x)}$. For the (massless) naive part

$$S_F[\psi, \bar{\psi}, U] = \sum_{n\in\Lambda} \bar{\psi}(n) (\sum_{\mu=1}^{d} \gamma_\mu \frac{U_\mu(n)\psi(n+\hat{\mu}) - U_\mu(n-\hat{\mu})^\dagger \psi(n-\hat{\mu})}{2}) = \bar{\psi} D_0 \psi \tag{6.16}$$

For the non-compact links we have (remembering $A_\mu^\dagger = A_\mu$ since A is real)

$$S_F[A] = \sum_{n\in\Lambda} \bar{\psi}(n)(\sum_{\mu=1}^{d} \gamma_\mu \frac{(1+iA_\mu(n))\psi(n+\hat{\mu}) - (1+iA_\mu(n-\hat{\mu}))^\dagger \psi(n-\hat{\mu})}{2}) \tag{6.17}$$

and so

$$\frac{\partial S_F[A]}{\partial A_\mu(x)} = (\bar{\psi}(x)\gamma_\mu i\psi(x+\hat{\mu}) + \bar{\psi}(x+\hat{\mu})\gamma_\mu i\psi(x))/2 \tag{6.18}$$

$$\frac{\partial S_F^\dagger[A]}{\partial A_\mu(x)} = -i(\bar{\psi}(x)\gamma_\mu \psi(x+\hat{\mu}) + \bar{\psi}(x+\hat{\mu})\gamma_\mu \psi(x))/2 \tag{6.19}$$

and for the compact links we have

$$\begin{aligned} S_F[A] &= \sum_{n\in\Lambda} \bar{\psi}(n)(\sum_{\mu=1}^{d} \gamma_\mu \frac{\mathrm{e}^{iA_\mu(n)}\psi(n+\hat{\mu}) - (\mathrm{e}^{iA_\mu}(n-\hat{\mu})^\dagger \psi(n-\hat{\mu})}{2}) \\ \frac{\partial S_F[A]}{\partial A_\mu(x)} &= (\bar{\psi}(x)\gamma_\mu i\mathrm{e}^{iA_\mu(x)}\psi(x+\hat{\mu}) + \bar{\psi}(x+\hat{\mu})\gamma_\mu i\mathrm{e}^{-iA_\mu(x)}\psi(x))/2 \end{aligned} \tag{6.20}$$

and the Wilson part

$$S_{FW}[\psi,\bar{\psi},U] = -\frac{1}{2}\sum_{n\in\Lambda} \bar{\psi}(n)(\sum_{\mu=1}^{d} U_\mu(n)\psi(n+\hat{\mu}) - 2\psi(n) + U_{-\mu}(n)\psi(n-\hat{\mu})) \tag{6.21}$$

For the non-compact formulation we have

$$\begin{aligned} S_{FW}[A] &= -\frac{1}{2}\sum_{n\in\Lambda} \bar{\psi}(n)(\sum_{\mu=1}^{d} (1+iA_\mu(n))\psi(n+\hat{\mu}) - 2\psi(n) + (1+iA_\mu(n-\hat{\mu})^\dagger)\psi(n-\hat{\mu})) \\ \frac{\partial S_{FW}[A]}{\partial A_\mu(x)} &= -\frac{1}{2}(\bar{\psi}(x)i\psi(x+\hat{\mu}) - \bar{\psi}(x+\hat{\mu})i\psi(x)) \end{aligned} \tag{6.22}$$

and for the compact formulation we have

$$S_{FW}[A] = -\frac{1}{2}\sum_{n\in\Lambda}\bar{\psi}(n)(\sum_{\mu=1}^{d}(\mathrm{e}^{iA_\mu(n)})\psi(n+\hat{\mu}) - 2\psi(n) + (\mathrm{e}^{iA_\mu(n-\hat{\mu})})^\dagger)\psi(n-\hat{\mu}))$$
$$\frac{\partial S_{FW}[A]}{\partial A_\mu(x)} = -\frac{1}{2}(\bar{\psi}(x)i\mathrm{e}^{iA_\mu(x)}\psi(x+\hat{\mu}) - \bar{\psi}(x+\hat{\mu})i\mathrm{e}^{-iA_\mu(x)}\psi(x)) \tag{6.23}$$

6.5 Effective Overlap Action

It is interesting to note the step which separates the force term of the domain wall formulation from the overlap formulation. Although the force terms are different the measurements should still be identical between the methods in the Monte Carlo integration limit. The question would be whether there is any difference in acceptance rate or other properties of the hamiltonian dynamics step. For the overlap action we have the partition function, identical to eqn. 6.6

$$Z = \int \mathcal{D}[U]\,\exp(-S_G[U])\det[D_{OL}(m)D_{OL}^\dagger(m)]^{1/2} \tag{6.24}$$

and for which we have the effective action

$$S_{eff}[\phi,\phi^\dagger,U] = \phi_1^\dagger(D_{OL}(m)D_{OL}^\dagger(m))^{-1/2}\phi_1 \tag{6.25}$$

In order to directly recast this in a domain wall formulation we use $\tilde{\phi} = \{\phi_1, 0, ..., 0\}$, and recall $K_{OL}(m) = C^\dagger M^{-1}(1)M(m)C$, eqn. 3.91. Then

$$\begin{aligned} S_{eff}[\phi,\phi^\dagger,U] &= \tilde{\phi}^\dagger(K_{OL}(m)K_{OL}^\dagger(m))^{-1/2}\tilde{\phi} \\ &= \tilde{\phi}^\dagger[C^\dagger M^{-1}(1)M(m)M^\dagger(m)(M^\dagger)^{-1}(1)C]^{-1/2}\tilde{\phi} \\ &= \tilde{\phi}^\dagger(C^\dagger)^{1/2}(M^\dagger(1))^{1/2}(M(m)M^\dagger(m))^{-1/2}(M(1))^{1/2}C^{1/2}\tilde{\phi} \end{aligned} \tag{6.26}$$

And so comparing with eqn. 6.8 we see the alterations which facilitate the use of a symmetric matrix inverter. The C matrices can be dropped since they just recombine to make a new set of random numbers.

$$\begin{gathered} \tilde{\phi}^\dagger(C^\dagger)^{1/2}(M^\dagger(1))^{1/2} \to \tilde{\phi}^\dagger(M^\dagger M(1))^{1/4} \\ (M(1))^{1/2}C^{1/2}\tilde{\phi} \to (MM^\dagger)^{1/4}\tilde{\phi} \end{gathered} \tag{6.27}$$

Chapter 7

Locality and the GW error

A code has been written in Fortran implementing the overlap and domain wall operators set out in chapter 3 with which to explore some of their properties. We provide some validation of the code before looking at the locality and the GW error.

7.1 Validation

Fig. 7.1 shows the L_s convergence of Dirac overlap operators (eqn. 3.55 and variants) with a fixed auxiliary field, and a fixed field ψ to apply the operator to. With j being the L_s value, for direct evaluation we use

$$\mathrm{err}_j = |D_j\psi - D_{j-2}\psi|_\infty \tag{7.1}$$

For indirect evaluation of the overlap operator utilising the domain wall operator, eqns. 3.91 and 3.92, we have

$$\mathrm{err}_j = |v_j - v_{j-2}|_\infty \tag{7.2}$$

where $v_j = (D_j^5\Psi_j)_1$, and $\Psi_j = \{\psi, 0, ..., 0\}$, so that v_j is the same size as Ψ_j. $D^5 = K_{DW}$ or $D^5 = K_{DW}^{M3}$.

The error of the Shamir operator is seen to converge more quickly than for the Wilson operator in both HT (hyperbolic tangent) and Z (Zolotarev) cases, the latter converging much more rapidly with L_s as expected. The convergence rates are indifferent to the choice of mass term, a slightly surprising result given our a priori knowledge [3] of the significant improvements to be had using the twisted mass formulation M3. The bare mass is set to 0.05. For the HT formulations, the indirect calculations should give identical values to the direct calculations (the Shamir Zolotarev and Shamir HT are

only the same in the L_s limit). This is shown in the right panel where the convergence plots are identical for the corresponding formulations. $12^2 \times 12$ lattices were used and the auxiliary field instance was generated, with the quenched assumption, with weak coupling of $\beta = 2$. Not only do we want each formulation to converge with L_s, we want all Shamir formulations to convergence to the same values, and all Wilson formulations to converge to the same values, although these will be distinct. Happily, we find this to be the case.

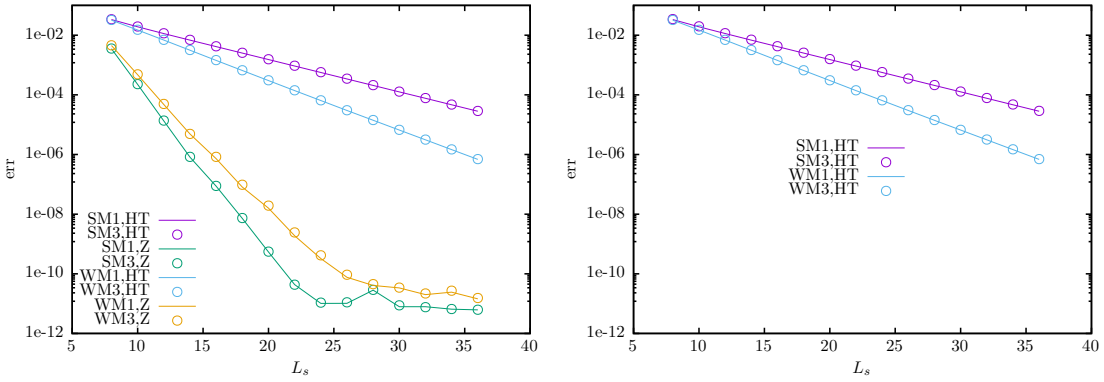

FIGURE 7.1: Dirac Operator Convergence. Left panel: Direct evaluation of the overlap operator (eqn. 3.55 and variants). Right panel: Indirect calculation of the overlap operator through K_{DW} (eqn. 3.91) and K_{DW}^{M3} (eqn. 3.92)

7.2 Locality of Overlap Operator

Overlap and domain wall fermions operators in the $L_s \to \infty$ limit obey the GW relation. In order to recover the $U(2)$ symmetry in the continuum limit $a \to 0$, we must have the GW terms $aD\gamma_5 D$ (eqn.3.19) and equivalently the transform terms $\frac{aD}{2}$ (eqn.3.21) vanishing in the same limit. A sufficient condition for this to be the case is the Dirac operator being exponentially local, which also ensure the uniqueness of the continuum limit [53]. The overlap operator is a dense matrix and manifestly non-local and hence exponential locality is certainly not obvious. Proof that it is has been given for the overlap operator in 3+1d in the weakly coupled region for QCD [53], and numerical support was also provided. The proof depends on the positive real boundedness of $H^\dagger H$, where H is the kernel of the sign function, and makes a separate case for when the smallest eigenvalues go to zero. However, the upper boundedness stems from the unitarity of the gauge links $U = e^{i\theta}$. However, with the non-unitarity $U = 1 + i\theta$, there is no such bound. Further, we are considering a strongly coupled region. Considering these factors, it is not inevitable that locality will hold near a critical region, nor in an unbounded model of different dimension.

To recover continuum $U(2)$ symmetry as $a \to 0$, we require

$$\lim_{a\to 0} e^{i\alpha\gamma_3(1-\frac{aD}{2})} = e^{i\alpha\gamma_3} \tag{7.3}$$

To see that exponential locality is sufficient to achieve eqn.7.3, note that

$$e^{i\alpha\gamma_3(1-\frac{aD}{2})}\Psi = e^{i\alpha\gamma_3}(I + i\alpha\gamma_3(-\frac{aD}{2}) + \cdots)\Psi \tag{7.4}$$

so that recovery requires

$$[aD\Psi]_{a\to 0} = 0 \tag{7.5}$$

Remembering D is itself dependent on a, we have $\Psi'_j = [a\sum_i D_{ji}\Psi_i]_{a\to 0} = 0$, which is true if $[\sum_i D_{ji}\Psi_i]_{a\to 0} < \infty$, which is true for any bounded Ψ if $[\sum_i D_{ji}]_{a\to 0} < \infty$, which is true if D is exponentially local, and hence exponential locality allows recovery of $U(2)$ symmetry.

Now, following the numerical methodology of [53], we want to illustrate locality in the critical region. We consider the effect of a Dirac operator D on a point source $\eta^{y,i}$ specified at an arbitrary location y on the lattice, and for a specified Dirac index, i. ie $\eta^{y,i}(x,d) = \delta_{x,y}\delta_{i,d}$. Then we evaluate

$$\psi = D\eta^{y,d} \tag{7.6}$$

Next, we calculate the decay of the point source as

$$l(r) = \max\{|\psi(x)|_2 : |x-y|_1 = r\} \tag{7.7}$$

using the l_2 norm for the decay value (over the dirac indices), and the l_1 norm to determine the distance from the source location y. This calculation of distance has been called the "Manhattan taxi distance".

For locality to hold, we expect to see exponential decay at some distance from the source. The decays of the Wilson overlap operator for quenched cases are shown for different lattice sizes and coupling strengths in figure 7.2. The mass is non-zero in the left panel and zero in the right panel, and suggests that the locality is essentially independent of m, at least for small m. Increasing the coupling strength slows the decay rate, and increasing the lattice volume shows the decay continuing to fall away further from the source at the same rate, indicating there is not a finite volume effect preventing the decay rate going to zero.

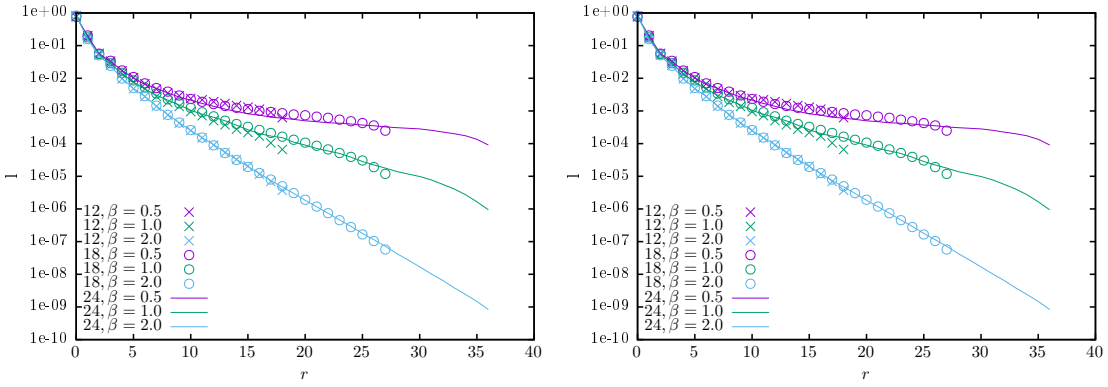

FIGURE 7.2: Quenched Wilson Locality. Calculated with Zolotarev, $Ls = 24$, range $[0.001, 10]$. Measurements taken at 8 points on each of 50 auxiliary fields. Left panel: $m = 0.01$. Right panel: $m = 0$.

Fig. 7.3 shows the decay with compact links for the quenched Wilson case. Unlike the compact case for which the decay rate is monotonically increasing with coupling strength, now the decay rate increases through the strong coupling region and then starts to decline again.

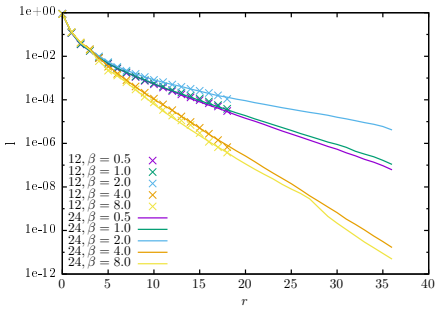

FIGURE 7.3: Quenched Wilson Locality. Measurements taken at 8 points on each of 50 auxiliary fields, $m = 0$, Zolotarev range $[0.001, 10]$

Although quenched formulations were used in the work of [53], we really want to use dynamically generated auxiliary fields. To this end we use fields, from a collaboration [7], generated with the Shamir kernel, $m = 0.005$, the twisted mass, and the HT approximation with $L_s = 64$ on a $16^2 \times 16$ mesh. β is varied over the established critical region $\beta \approx 0.28$. Plots are shown in fig. 7.4.

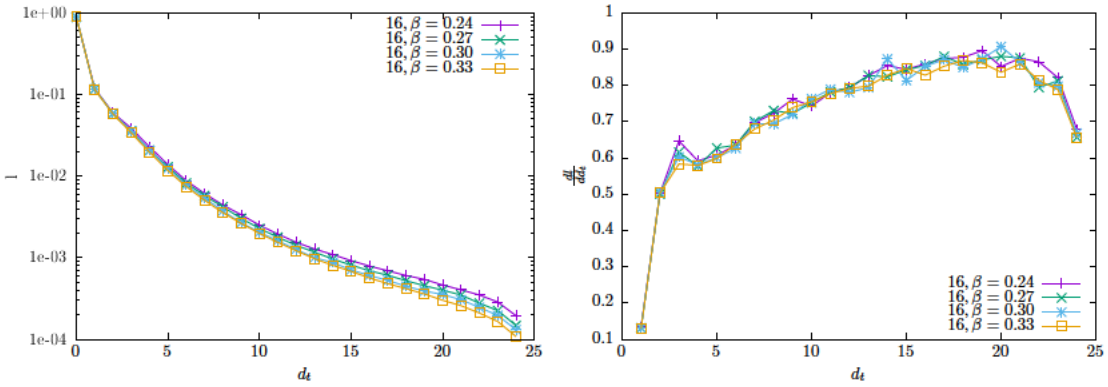

FIGURE 7.4: Dynamic Shamir Locality. Measurements taken at 8 points on each of 12 auxiliary fields.

We see in the left panel that, although increasing slightly over the critical point, the decay rate is dependent on the number of lattice points rather than physical distance, and hence is consistent with non-locality.[1] Convergence to a meaningful value of the decay rate on this small volume is seen to be difficult in the right-hand plots which show the exponent from one d_t-value to the next, by plotting $f(d_t)/f(d_t - 1)$.

At the critical value, as $a \to 0$, non locality would lead to a zero decay rate in lattice units. Since this is manifestly not the case in any of the results, we may conclude that this is strong evidence for the exponential locality of the operators, as we hoped.

7.3 Ginsparg Wilson Error

We also examine the L_s error of the overlap operator via the GW term, as a means to assess recovery of U(2) symmetry. We define the GW error as, with $a = 1$,

$$\text{err}_{GW} = |(\gamma_3 D + D\gamma_3 - 2D\gamma_3 D)\psi|_\infty \tag{7.8}$$

with ψ a randomly assigned field. This error should be exactly zero for zero mass as $L_s \to \infty$. There is also what we call the GW correction term, eqn 7.9.

$$\text{GW}_{cor} = |(2D\gamma_3 D)\psi|_\infty \tag{7.9}$$

The correction should vanish as we reach the continuum limit, and U(2) symmetry is restored. Now we concentrate on the GW error which is amenable to testing with quenched fields, and rely on the locality of the previous section to ensure that this correction term will vanish.

[1] The non-dimensional lattice spacing in the code is kept at 1. As $\beta \to \beta_c$ the physical lattice spacing goes to zero.

For each β we use a single fixed instance of a quenched auxiliary field, consistent between different equal-β cases, and a fixed instance of ψ, consistent between all cases. With these configurations we look at the GW error. Fig. 7.5 shows plots with the Wilson kernel. In the left panel, using the HT approximation, we see that in the weakly coupled case, $\beta = 2$, the error vanishes rather quickly (to machine precision by approximately $L_s = 60$). Errors are also shown with non-zero mass values of $m = 0.001$ and $m = 0.01$. The larger the mass value is, the sooner on the L_s scale the GW error is subsumed by the mass term. With the stronger couplings, $\beta = 1$ and $\beta = 0.5$, we see that the error decay rate is very significantly hampered, not even reaching a value of 0.01 by $L_s = 160$ in the strongest $\beta = 0.5$ case. The non-zero mass terms again limit the L_s convergence according to their magnitude.

The right panel shows the error with Zolotarev approximations. The Zolotarev range was set according the the kernel eigenvalues as given in table 7.1. A stronger coupling of $\beta = 0.2$ is now included. As expected the decay rate is significantly improved, and again the mass terms overwhelm the error decay. Interestingly, the decay rate does not deteriorate further from $\beta = 0.5$ to $\beta = 0.2$, but in fact is a marginal improvement. This is reasonable since β is then further away from the critical value (which we will show is ≈ 0.8 for the quenched case). However, it is also explained by the difference in instance of the auxiliary field, considering the eigenvalue range given in table 7.1. The $\beta = 0.5$ has a larger condition number than the $\beta = 0.2$ case, and the error of the sign approximation is proportional to this.

As will be shown in the next chapter, on average the stronger coupling will lead to a wider eigenvalue range, rather than the inversion found in these instances. Of course L_s convergence is not exclusively governed by the properties of the scalar sign function approximation.

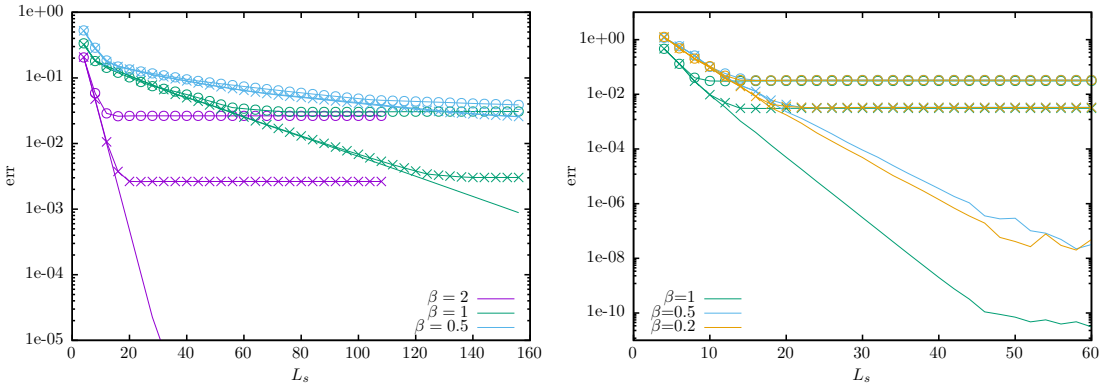

FIGURE 7.5: Wilson kernel GW error calculated on a single quenched configuration, generated with $\beta = 0.2$, $\beta = 0.5$, $\beta = 1.0$ or $\beta = 2.0$. For masses $m = 0$ (no point type), $m = 0.01$ (circle), $m = 0.001$ (cross). Left and right panels have different scales. Left panel: HT formulation. Right panel: Zolotarev formulation.

In the left panel of fig. 7.6 a direct comparison of the Wilson Zolotarev and Wilson HT cases is plotted. In the right hand panel, a similar plot is given, but for the Shamir cases. Again, the Zolotarev approximation very significantly increases the error decay rate. Further the Shamir formulations give a slight improvement on the Wilson formulations despite having a larger condition number in the $\beta = 0.5$ instance.

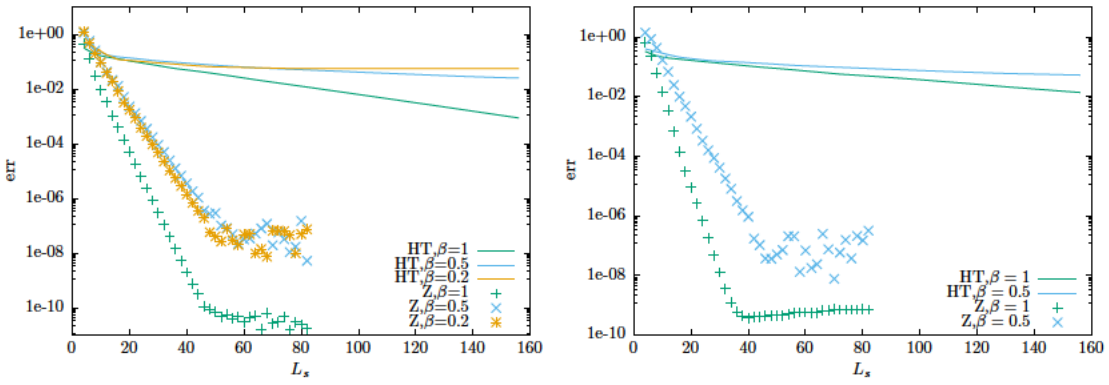

FIGURE 7.6: GW error calculated on a single quenched configuration with Zolotarev and HT formulations with $m = 0$ in all cases. Left panel: Wilson kernel. Right panel: Shamir kernel ($8^2 \times 8$ lattice).

β	W min	W max	W cond	S min	S max	S cond
1	1.82e-2	5.72	314	9.1e-3	2	219
0.5	2.72e-4	7.29	26,801	1.36e-4	4.3	31,618
0.2	5.8e-4	10.77	18,569			

TABLE 7.1: Wilson and Shamir kernel eigenvalue ranges and condition number (max/min eigenvalue) for the auxiliary field used for the GW error calculations at each β.

Referring to table 7.1 we observe that the lowest Shamir eigenvalues are half of those with the Wilson formulation. This is not a coincidence and is reproduced on a series of auxiliary fields in fig. 7.7 with the legend S(Wilson) referring to the evaluation of eqn. 7.10.

$$\lambda_S \approx \lambda_W/(2+\lambda_W) \tag{7.10}$$

It is not a formal relation, $\lambda_S \neq \lambda_W/(2+\lambda_W)$ in general, and merely observed in passing. It only holds when $M = 1$, and only for the smallest eigenvalues. It does not hold for the largest eigenvalues.

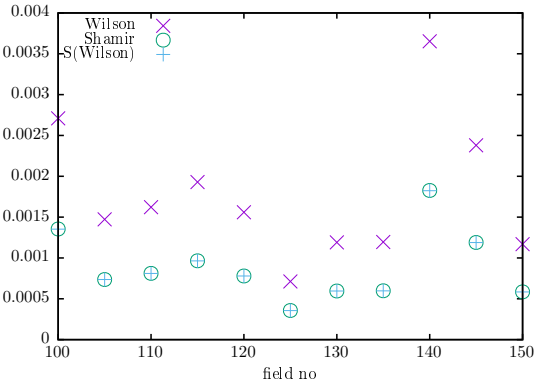

FIGURE 7.7: Minimum eigenvalues for Wilson and Shamir kernels for a range of auxiliary fields. S(Wilson) is the smallest eigenvalue calculated according to eqn. 7.10.

Error plots are included for the compact formulations in fig. 7.8 in which a similar story is borne out, but with greatly improved convergence rates, suggesting that the very high L_s needed for U($2N$) recovery in the critical region of the Thirring model have their origin in the non-unitary nature of the link fields.

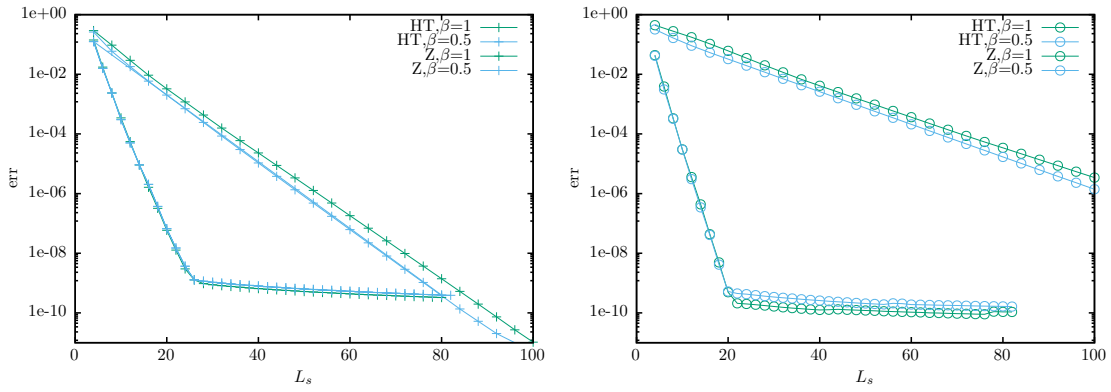

FIGURE 7.8: GW error calculated on a single compact gauge configuration with $m = 0$. Left panel: Wilson. Right panel: Shamir.

We note there are ways to estimate the chiral error which are independent of the random ϕ field. [61] defines $m_{res} = \frac{\mathrm{Tr}[\Delta_{L_s}(D^\dagger D)^{-1}]}{\mathrm{Tr}[(D^\dagger D)^{-1}]}$ and [43] uses $\sigma = \max[(\mathcal{D}^{-1}\gamma_5 + \gamma_5\mathcal{D}^{-1})_{i,j}]$ with $\mathcal{D}^{-1} = \langle q\bar{q}\rangle$.

The GW error gives a measure of how well L_s converged the overlap operator. However, it is limited by the magnitude of the mass term, and it is tempting to assume that in the massive cases we are sufficiently L_s converged when the GW error is dominated by the mass term. However, condensate measurements (in the next sections) show that this mass limited L_s convergence is not sufficient for accurate measurements, and much higher L_s values are required.

Chapter 8

Quenched Overlap Condensate Results

The evaluation of the condensate, attempts to improve the evaluation of the condensate, and calculation of the equation of state constitute the primary focus of this work and take up the next two chapters. This chapter focuses on quenched condensates, from which we learn what we can, before moving to the physically more relevent dynamic cases in the next chapter. We start with a validation of the condensates which were set out in chapter 4. Then we look at the eigenvalue range of the operator kernel which is an essential aspect in achieving L_s-convergence, as well as the condition number of the overlap operator itself, which controls the ease of its inversion. We finally look at the condensates themselves and the equations of state to be constructed from them.

8.1 Validation

As before, we want to ensure that the condensate, measured in the $L_s \to \infty$ limit, is unaffected by choice of sign approximation, HT or Z, or choice of mass type, M1 or M3. We start with sanity checks on $6^2 \times 6$ grids with a free auxiliary field, $A_\mu = 0$. We can see in Figure 8.1 that both the different Wilson and Shamir formulations converge with L_s as expected, for each of the four cases considered. The Wilson formulation solution appears to oscillate around the limit rather than converge only from above as is the case for Shamir, as has been previously noted [3]. The Zolotarev range, eqn. 3.72, was calculated as designated by the eigenvalue range of the overlap kernel generated with the free auxiliary field, explored further in the next section. The point method (see appendix B.3) was used for exact results. The overlap regularisation parameter, M, eqn. 3.54 is set to 0.9 for consistency with earlier work [44] (unless otherwise stated it is set to 1.0 by default).

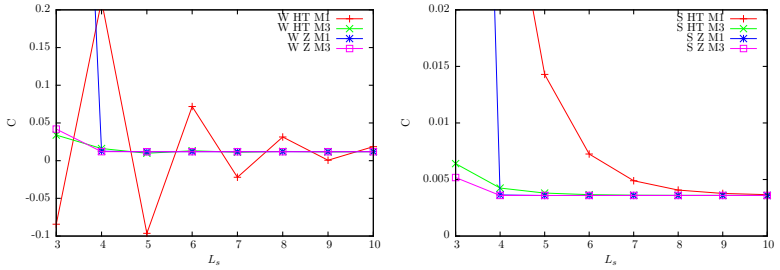

FIGURE 8.1: Condensates $C = \langle\bar{\psi}\psi\rangle$ vs L_s with free auxiliary field $A_\mu = 0$. HT denotes hyperbolic tangent formulations, Z denotes Zolatarev. Left panel: Wilson kernel. Right panel: Shamir kernel.

Moving to stronger coupling, we consider single fixed quenched auxiliary fields with link values given by gaussian random numbers with standard deviation s, $A_{i,\mu} \sim N(0, s^2) = sN(0, 1)$, and $\beta = 1/s^2$, i.e. in accordance with eqn. 5.19. The noisy estimation method is used (again see appendix B.3), and plots for $s = 0.5$ and $s = 1.0$ are shown in figure 8.2. Somewhat alarmingly the standard mass formulation, designated M1, with the HT rational function, in the stronger coupling case does not *appear* to converge to the other values. Again M=0.9, and the Zolotarev range was calculated for each designated auxiliary field.

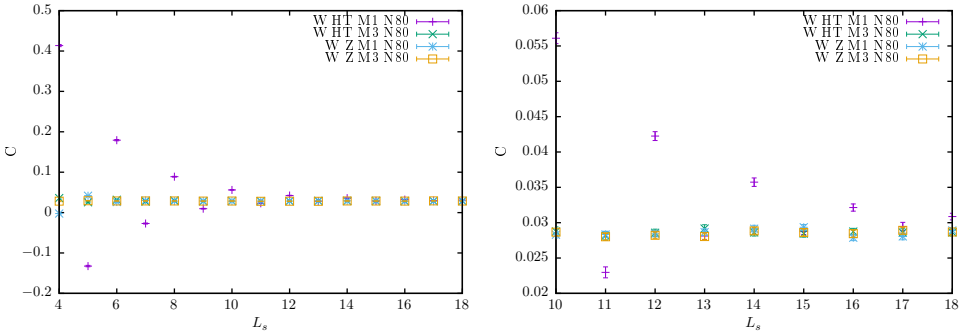

FIGURE 8.2: Condensates with Wilson kernel, denoted W in the legend. N80 specifies 80 fields were used for the noisy estimation. Left panel: auxiliary field with s=0.5. Right Panel: auxiliary field with s=1.0. Note both x and y axis scales differ.

Figure 8.3 continues to show this more distinctly on another $s = 1.0$ configuration. However, as the right panel shows, the problem is merely than the L_s value was not large enough. The plot further indicates that the solution is *not* oscillating around the asymptotic limit, but oscillating around a monotonic curve with the same asymptotic limit instead. We note care must be taken in extrapolating to the L_s limit.

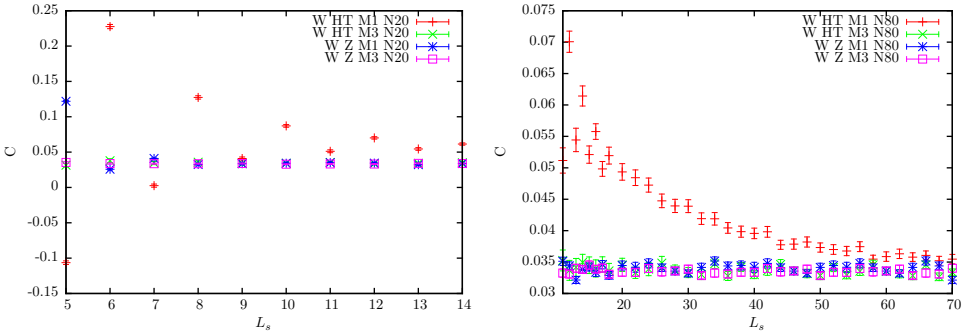

FIGURE 8.3: Condensates with Wilson kernel, denoted W in the legend. N20 specifies 20 fields were used for the noisy estimation, and N80 specifies 80 fields. Left panel: the problem. Right panel: the solution.

Considering a $N_s^2 \times N_t$ mesh, we find the thermodynamic limit as the lattice spatial extent N_s goes to infinity, keeping the temporal extent fixed at a lattice size $N_t = 12$. The left panel of fig. 8.4 shows the quenched condensate for three different values of $\beta = 1/s^2$, and suggests that the spatial extent of $N_s = 12$ lattice vertices is sufficient for our purposes, with the potential to even move to a smaller mesh. The right panel shows the condensates for mesh sizes varying the time extent equally with the spatial extents. Sending $N_t \to \infty$ corresponds to zero temperature. We suggest a 12^2x12 mesh is (close to) sufficient to investigate zero temperature cases in the thermodyamic limit.

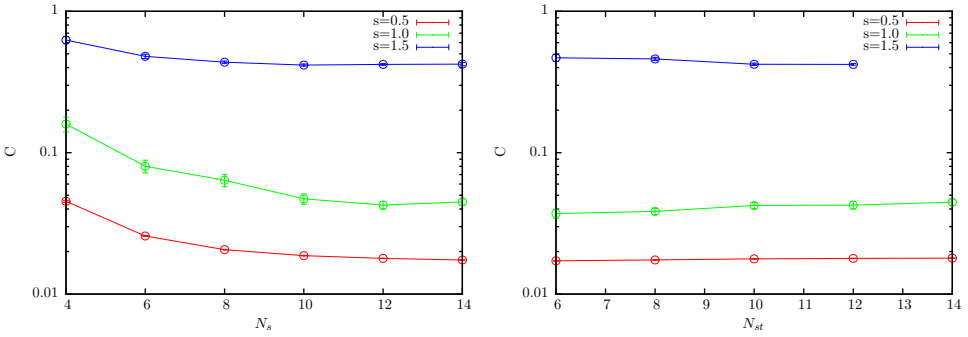

FIGURE 8.4: Quenched Condensates calculated with the Wilson kernel. Left panel: thermodynamic limit varying N_s, and $N_t = 12$. Right panel: Varying both $N_s = N_t$ together, denoted N_{st} in the x-axis.

8.2 Eigenvalue Extrema and Condition Number of Kernel

The evaluation of the overlap operator requires the evaluation of the sign function. The relative computational ease or difficulty of evaluation of the sign function is in part dependent on the condition number and extrema of the eigenvalues of the sign function kernel. The Wilson Dirac operator D_W has complex eigenvalues and is γ_5-hermitian, i.e. $\gamma_5 D_W$ is hermitian, and hence $\gamma_5 D_W$ has real eigenvalues, and $\gamma_5 D_W \gamma_5 D_W =$

$D_W^\dagger D_W$ has real semi-positive eigenvalues. Figure 8.5 shows the eigenvalue extrema of the Wilson and Shamir overlap kernels, given by $H_W = \gamma_3 D_W(-M)$, and $H_S = \gamma_3 \frac{D_W(-M)}{2+D_W(-M)}$ respectively, where now we use (the domain wall height) $M = 1$. Since quenched auxilliary fields are generated independently from the fermions, the quenched kernel has no dependence on the fermion mass m.

There is a lattice size independent increase in the upper bound for the Wilson kernel, which continues to increase as $\beta \to 0$. Noting from section 8.9 ahead that the critical region is in the vicinity of $\beta = 0.7$, we observe that for the Shamir kernel, the upper bound is largely lattice size independent only on the symmetry unbroken side. Only the top halves of the standard deviation is plotted, since the values are too large on a log plot. The lower bounds for both kernels are strongly dependent on lattice size as β moves into the strongly coupled region. The lower bounds reach a minimum value somewhere around the critical region and then increase again. Similarly for the strongly coupled side for Shamir kernel, the maximum eigenvalue decreases again. However, the upper bound for the Wilson kernel is monotonic. Whether the trends in these volume effects continue arbitrarily is unclear from this data, although if continued it would suggest an unbounded maximum eigenvalue for the Shamir case around the critical region.

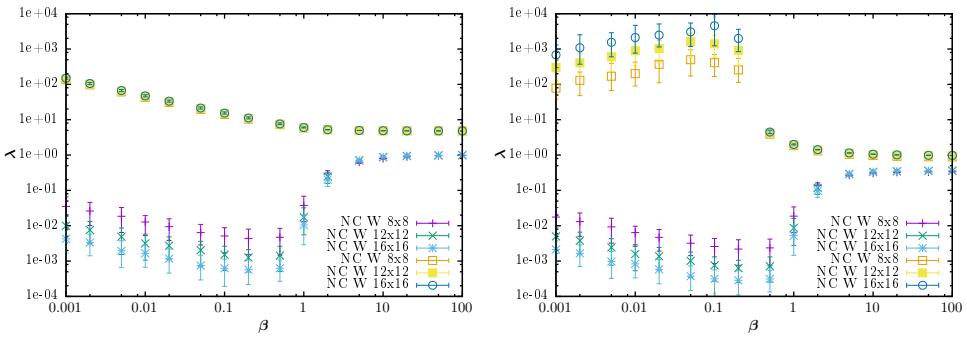

FIGURE 8.5: Minimum and maximum eigenvalues with standard deviation on different grid sizes. NC denotes non-compact links. 8x8 denotes gird extents $N_s = 8$, $N_t = 8$. Left panel: Wilson kernel. Right panel: Shamir kernel.

Figure 8.6 shows the condition numbers. In the weakly coupled limit the Shamir kernel has the lower condition number, and hence better numerical properties, whereas moving towards the stronger coupling and through the critical point the Wilson kernel has a much smaller condition number, although the value declines again for the Shamir kernel.

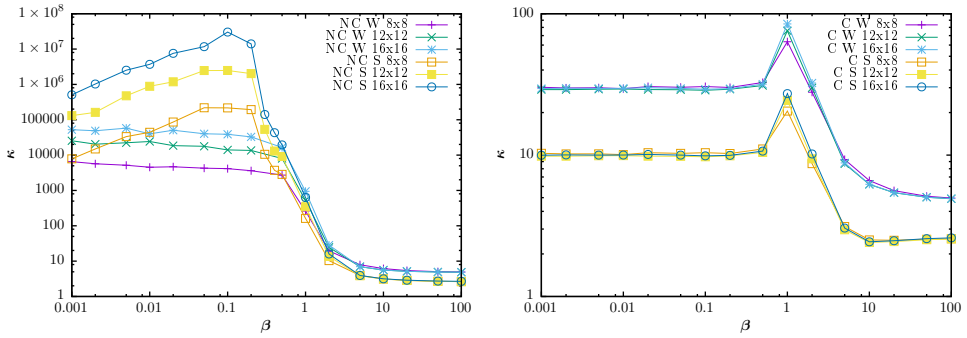

FIGURE 8.6: Condition number. Left panel: Non-compact link fields, eqn. 2.8. Right panel: Compact link fields, eqn. 2.7.

Fig 8.7 shows a similar plot for the compact link formulation. The bounds appear to be largely independent of the lattice size. The plots are qualitatively similar for both Wilson and Shamir, being bounded above, and bounded below in both the strong and weak coupling limit. It is unclear if the spike is bounded. The condition number shown in the right panel of figure 8.6 suggests that the Shamir kernel is numerically advantantageous under all coupling strengths.

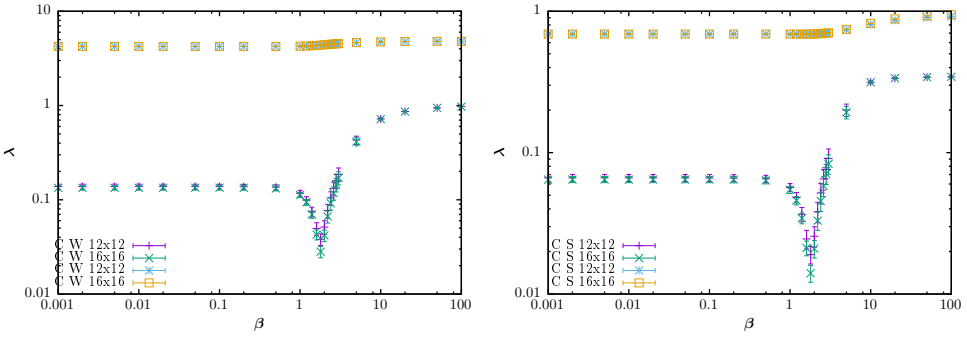

FIGURE 8.7: Minimum and maximum eigenvalues for compact quenched cases. Left panel: Wilson kernel. Right panel: Shamir kernel.

The effect of the domain wall height is considered in fig. 8.8, and the results are stark. Although the maximum eigenvalue on average becomes slightly higher with decreasing M, the minimum eigenvalue becomes significantly larger around stronger couplings, with the consequent improvement in condition number shown in the left panel of fig. 8.10. There are similar improvements with the Shamir kernel, as shown in fig. 8.9 and the right panel of fig. 8.10. The Shamir plots have a greater extent in the strong coupling region, and the benefits, although still there, are reduced. As will be seen this is a region beyond the critical coupling strength.

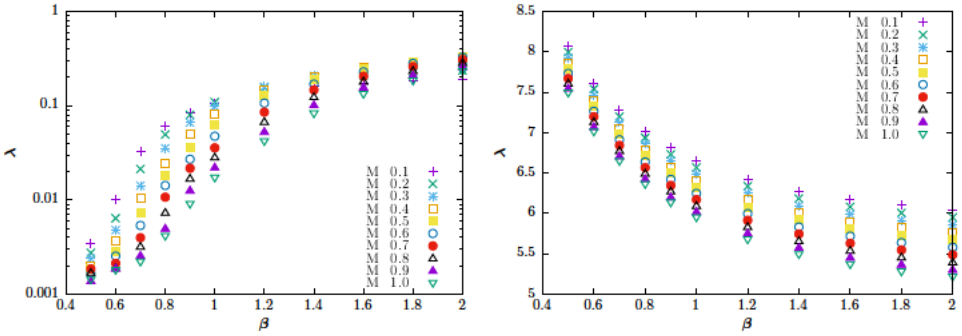

FIGURE 8.8: Average eigenvalues for quenched Wilson kernels, varying domain wall height M. Left panel: Minimums. Right panel: Maximums.

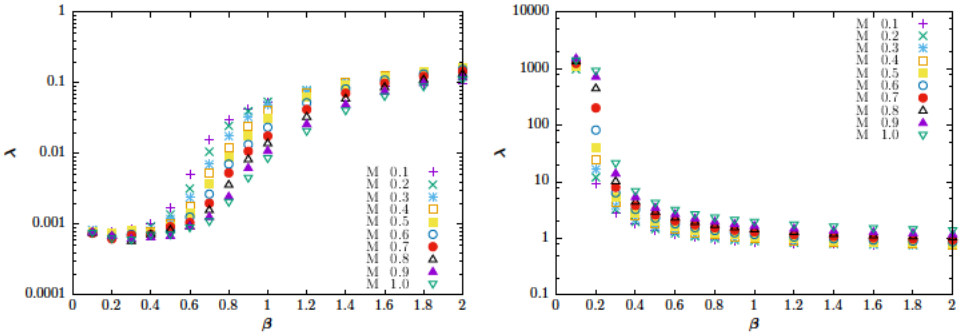

FIGURE 8.9: Average eigenvalues for quenched Shamir kernels, varying domain wall height M. Left panel: Minimums. Right panel: Maximums.

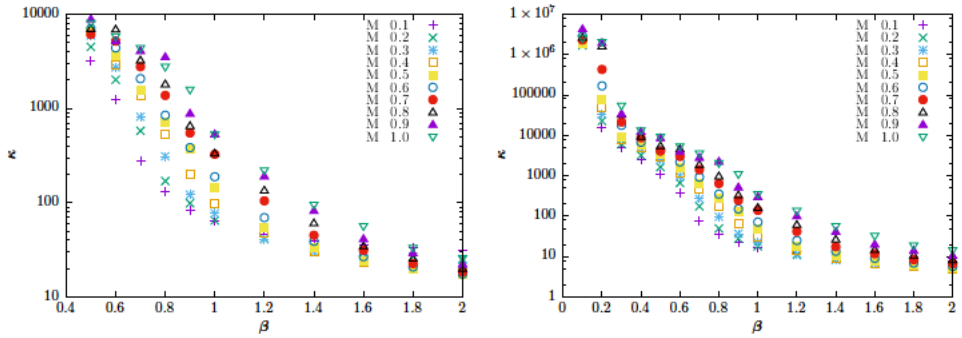

FIGURE 8.10: Average condition number for quenched kernels, varying domain wall height M. Left panel: Wilson kernel. Right panel: Shamir kernel.

8.3 Eigenvalues of Overlap Operator

We turn to eigenvalue ranges of the overlap Dirac operators, eqns. 3.60, 3.59, 3.57, with the twisted mass variant and both the Wilson and Shamir formulations. The left panel of fig. 8.11 shows the average minimum eigenvalues for $m = 0$ and $m = 0.03$, and for

Zolotarev with $L_s = 24$ (Z24) and HT with $L_s = 36$ (H36) for the Wilson cases. We see that the mass term controls the minimum value as the coupling gets stronger, and this allows for the H36 case giving equal results to the Z24 case. For $m = 0$ we see that H36 is not sufficient and curtails the smallest eigenvalues, which are better captured by the Z24 case. Shamir cases are shown in the right panel, and again show the suppression of the smallest eigenvalues when the L_s limit has not been reached.

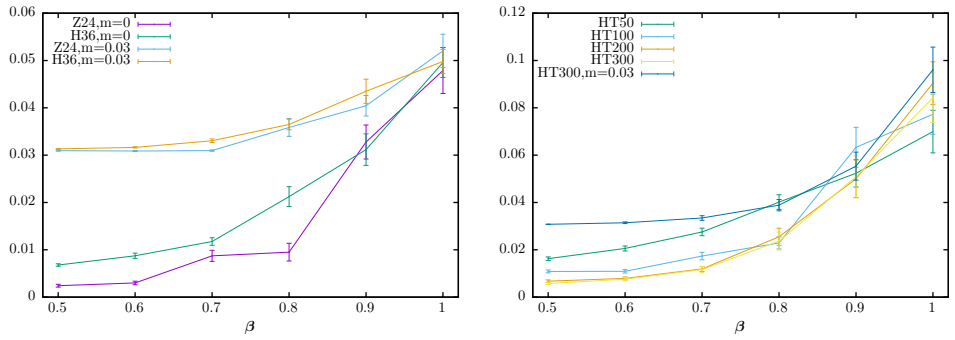

FIGURE 8.11: Average minimum eigenvalues of the overlap operator using $12^2 \times 12$ quenched auxiliary fields. Left panel: Wilson kernel. Right panel: Shamir kernel.

8.4 Computational Cost of Overlap Operator

We want to evaluate the computational cost of inverting the overlap operator. This can very roughly be done by counting the number of times the Dirac Wilson operator, D_W or $D_W^\dagger$, is called. The inversion includes an outer loop for which we count the number N_o of applications of $D_{OL}^\dagger D_{OL}$ in the CG algorithm. For the inner loop we count the number N_i of calls to the multishift CG [38] routine used for the calculation of the sign function with each application of D_{OL}. Each inner loop has a twin application of the Wilson Dirac operator $D_W^\dagger D_W$, and hence the total number of calls to D_W or $D_W^\dagger$ is $N_t = 4N_oN_i$.

Fig. 8.12 shows for the direct calculation with the Wilson kernel (eqn. 3.66). The outer loop count demonstrates a dependence beyond the condition number, although for the larger masses at stronger coupling the condition number dependence on the mass does appear to be the dominant factor. However, surprisingly and contrary to the condition number, the HT formulation requires more outer loops than the accurate Zolotarev formulation. Further the Zolotarev formulation at smallest mass requires more outer loops with zero mass. On the other hand, the right panel shows the significantly increased inner loop count with Zolotarev and strong coupling. Of course, since in the quenched case the auxiliary field is independent of the mass term, the inner loop is independent of the mass term, which is reflected in the plot.

The indirect method[1] is used to calculate the overlap operator with the Shamir formulation (eqn.3.93). This requires the inversion of the domain wall operator (eqns.3.42 and 3.44) which only has outer loops for the CG algorithm, each loop calling $D^{\dagger}_{DW}D_{DW}$. Each call to the domain wall operator has L_s calls to either of the Wilson Dirac operators D_W or $D^{\dagger}_W$. The total count is then $N_t = 2N_sL_s$.

In the left panel of fig.8.13 we see the CG loop count N_s increasing as L_s increases. Further we see that the addition of a small mass term further increases the loop count, but again larger mass terms constrain the loop count, which we see at stronger couplings. The right panel shows the total Wilson Dirac operator counts. While not a fair comparison on which to base the choice of one method over the other, it is interesting to note that both the nominally L_s converged formulations, H300 for the Shamir case, and Z24 for the Wilson case, have the same order of magnitude in counts at the stronger couplings. The increase in cost with the addition of a small mass is further demonstrated in the total count.

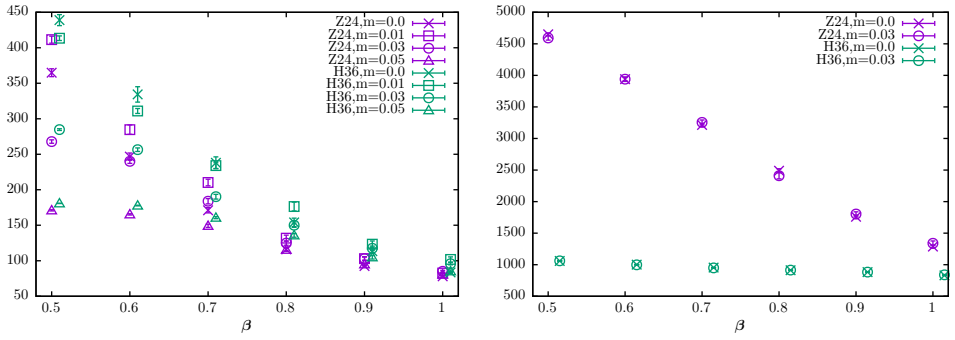

FIGURE 8.12: Average Dirac operator application count for direct Wilson inversion. The HT results are slightly offset for clarity. Left panel: Outer loop count. Right panel: Inner loop count.

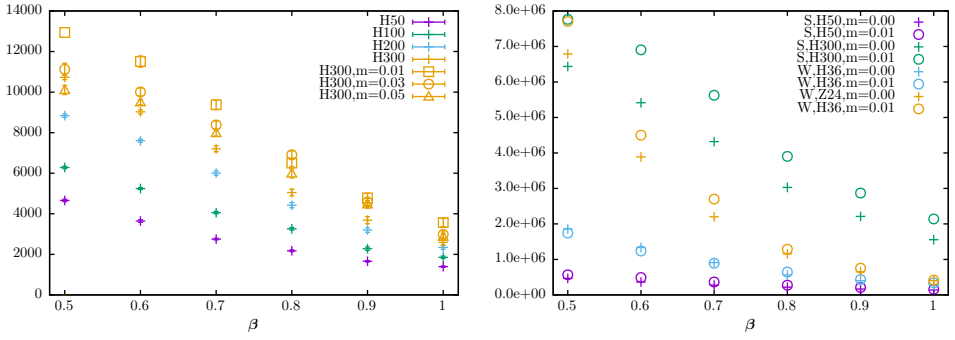

FIGURE 8.13: Average Dirac operator application count for Dirac inversion. Left panel: Indirect Shamir loop count. Right panel: Total loop count.

[1]Meaning the domain wall formulation including Paulli-Villars terms and the compacting matrices, eqn. 3.92

8.5 Wilson Condensates

We are interested in the condensate $C = \langle\bar{\psi}\psi\rangle$, which is the order parameter. Beyond the critical point, $\beta < \beta_c$, and at $m = 0$, we expect the value to become non zero. Unfortunately we cannot calculate this directly using $m = 0$, and must instead consider the $\lim_{m\to 0}$ curves in order to find the critical point, as has been done for the (dynamic) Shamir case [46].

Convergence with L_s is shown in the left panel of Figure 8.14 for $m = 0.05$ for $L_s = 60$ for the HT formulation and $L_s = 24$ for the Zolotarev formulation. $L_s = 60$ is shown to be insufficient for the HT case with $m = 0.01$. The right panel, showing $m = 0.005$ cases, similarly indicates that $L_s = 84$ is not sufficiently converged in the HT case, although the Zolotarev formulation may be converged.

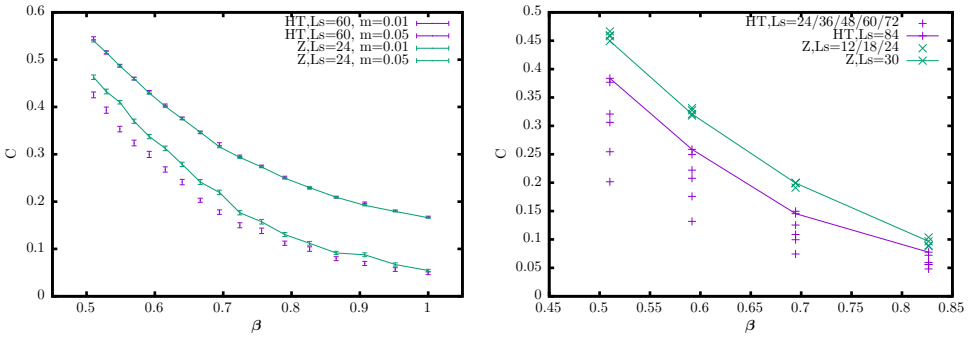

FIGURE 8.14: Condensate for non-compact Wilson. Zolotarev cases use range $[0.001, 10]$. Left panel: HT and Zolotarev cases for $m = 0.01$ and $m = 0.05$. Right panel: Ls convergence for m=0.005.

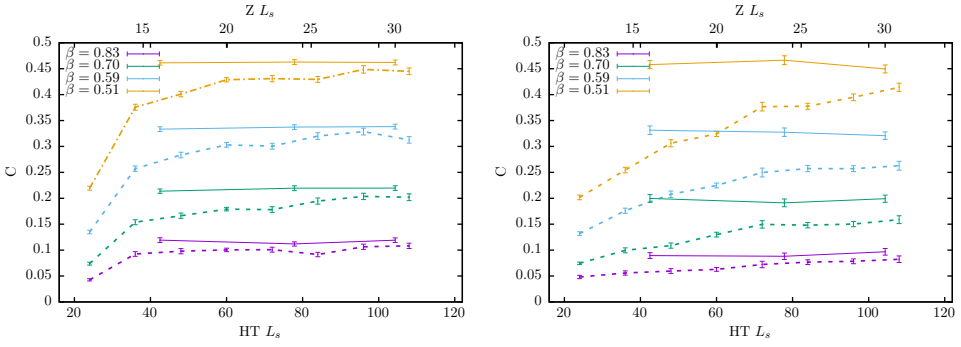

FIGURE 8.15: Wilson condensates vs L_s for different coupling strengths. The solid line is for the Zolotarev approximation and corresponds to the upper x-axis. The dashed line is for the HT approximation and corresponds to the lower x-axis. Left panel: $m = 0.01$. Right panel: m=0.005.

Despite the kernel eigenvalues being independent of the mass (since quenched there is no dependence on any aspect of the fermion), the condensate L_s convergence is clearly

highly dependent on the mass value, as can be seen in fig. 8.15. The left panel indicates that with $L_s > 100$ at $m = 0.01$ the HT formulation is reasonably L_s converged for all the coupling strnegths considered. However, for $m = 0.005$, shown in the right panel, L_s convergence has not been achieved, and is still a way off. The Zolotarev formulations, noting that they are plotted at 3 times their L_s value seem to be converged.

The set of Zolotarev results are shown in the left panel of Figure 8.16. The right panel shows the extrapolation to $m = 0$ and clearly indicates the non broken phase at β=1.56 and the broken phase at β=0.51.

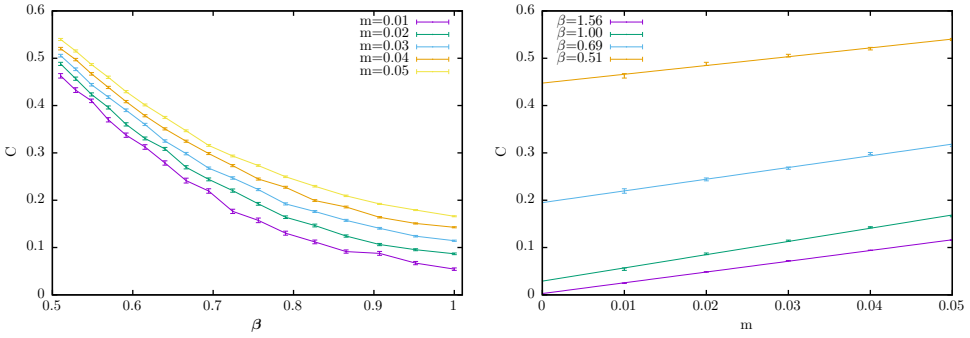

FIGURE 8.16: Wilson. Non-compact. Zolotarev range $[0.001, 10]$, $L_s = 24$. Left panel: C vs β. Right panel: C vs m.

8.6 Compact Wilson Condensate

We also consider the compact formulation for comparison, and because they are found with considerably less computational requirements than for the non-compact cases. We find the somewhat surprising results indicated in Figure 8.17, comparable to the non-compact cases in Figure 8.16. Now the left plot shows the magnitude of the condensate decreasing with coupling strength, contrary to expectation. All mass fit lines go through the origin (or at least significantly closer to the origin than for NC) in the right panel, suggesting that there is no spontaneous chiral symmetry breaking, at least with the mass as the order parameter.

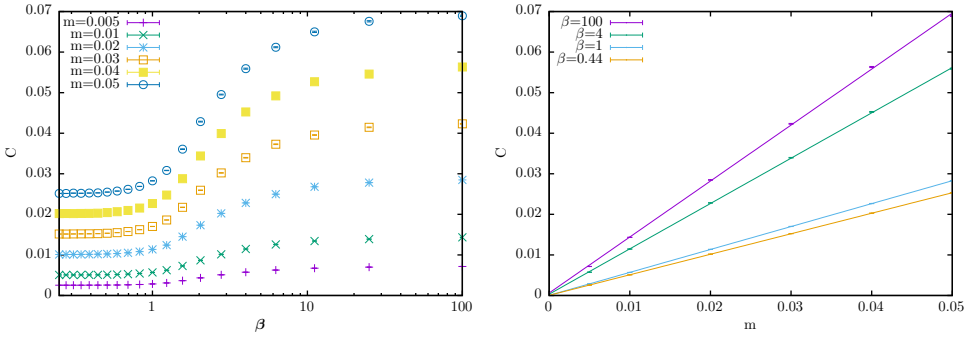

FIGURE 8.17: Wilson. Compact. Zolotarev range $[0.01, 10]$, $L_s = 16$. 96 aux fields. 10 noise. Left panel: Vs β. Right panel: vs m.

8.7 Shamir Condensates

We may surmise from the kernel eigenvalue ranges given in the right panel of fig. 8.5, and the accuracy plots of the hyperbolic tanh approximation given in fig. 3.4, that an L_s value of around 300 may be sufficient to capture the stronger couplings we are interested in. Fig. 8.18 shows the L_s convergence for $m = 0.01$ and $m = 0.05$. $L_s = 300$ does appear to be sufficient for strong coupling and the smaller mass values, although is unnecessarily large for weaker coupling and larger masses. This is in alignment with the findings of Hands [46], although the larger meshes used in that work would require yet higher values of L_s.

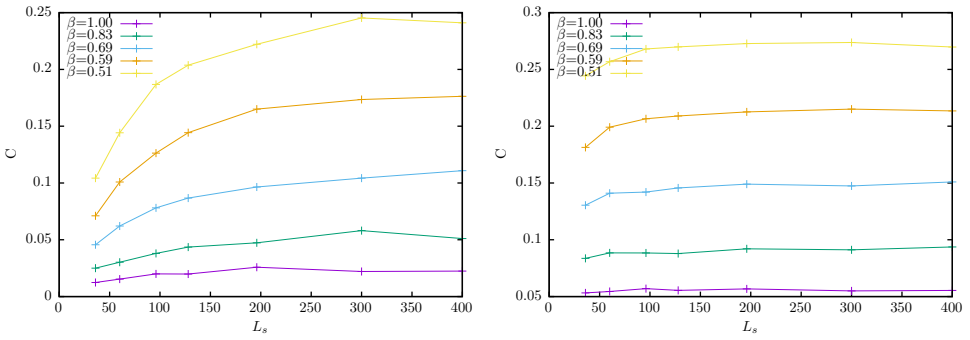

FIGURE 8.18: Quenched condensates with Shamir kernel. Left panel: m=0.01. Right panel: m=0.05.

Fig. 8.19 shows the condensates, both with $L_s = 300$, with the domain wall height $M = 1.0$ in the left panel and $M = 0.5$ in the right panel. There is a very clear shift and increase in the gradient, suggesting a rescaling so that $m_{M=0.5} < m_{M=0.5}(m_{M=1.0})$. It would be interesting to see if any potential computational cost increases trade off more or less than the likely cost advantages provided in the improved eigenvalue range of the kernel indicated earlier in section 8.2.

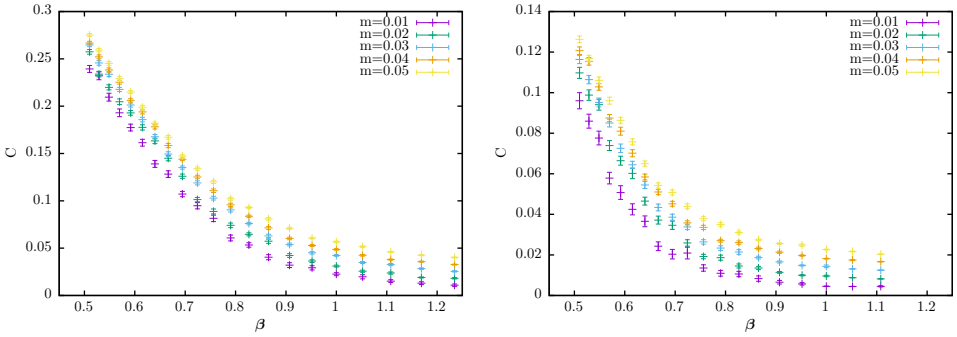

FIGURE 8.19: Quenched condensates with Shamir kernel, $L_s = 300$. Left panel: M=1.0. Right panel: M=0.5.

8.8 Compact Shamir Condensate

Again we turn to the compact formulation for comparison, and find the same absence of spontaneous chiral symmetry breaking. Fig. 8.20 shows similar behaviour to that of the Wilson formulation but is no longer monotonically decreasing with coupling strength. Fig. 8.21 shows a comparison of the Shamir and Wilson data, multiplying the Shamir condensates by a factor of 3. Results with the Shamir kernel have a sharper gradient through the transitional region, perhaps giving a hint of the difference in scaling between the models.

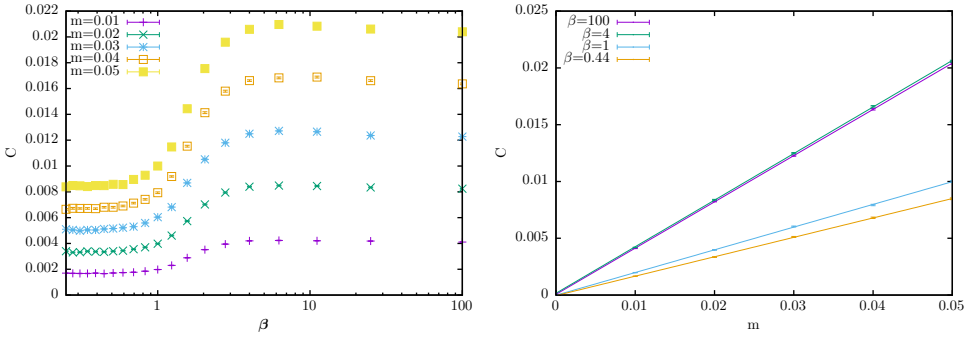

FIGURE 8.20: Quenched condensates with compact Shamir kernel. $L_s = 64$. 96 auxiliary fields. 10 noisy estimates per field. Left panel: Vs β. Right panel: vs m.

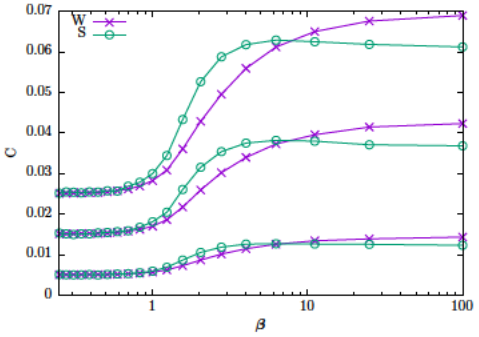

FIGURE 8.21: Compact quenched condensates comparing Shamir and Wilson kernels. Masses are $m = 0.01, 0.03, 0.05$.

8.9 Wilson EOS

We turn to the evaluation of the equation of state, and the critical exponents. We use the $n_p = 5$ parameter EoS $\equiv$ EoS$(C, m, \beta; \mathbf{p})$ introduced in section 5.2, with $C = \langle\bar{\psi}\psi\rangle$, where the 5 parameters are $\mathbf{p} = \{\mathrm{A}, \mathrm{B}, \beta_\mathrm{c}, \beta_\mathrm{m}, \delta\}$, including the two critical exponents β_m, and δ, and also the critical coupling strength β_c.

$$\mathrm{EoS} \equiv A(\beta - \beta_c)C^{\delta - 1/\beta_m} + BC^\delta - m = 0 \tag{8.1}$$

We have simulation data $\{C_i, m_i, \beta_i, \sigma_i^c\}$ where σ_i^c is the error in the calculation of C_i. We wish to find the best parameters for the EoS to fit this data with a least squares minimisation of χ^2 according to eqn. 8.2.

$$\chi^2_k(\mathbf{p}) = \sum_{\mathrm{i}=1}^{\mathrm{k}} (\mathrm{EoS}(\mathrm{C_i}, \mathrm{m_i}, \beta_\mathrm{i}; \mathbf{p})/\sigma_\mathrm{i}^2 \tag{8.2}$$

σ_i^2, the error in the fit, is given by $\frac{\partial \mathrm{EoS}}{\partial C}\sigma_i^c$. The reconstructions are carried out using a python script[2], providing a least squares fit using the Levenberg-Marquardt algorithm [62]. A goodness of fit is given by χ^2/dof, where the degrees of freedom is given by $dof = k - n_p$, where 1 is the ideal fit, greater than 1 has the data overprescribing the problem, and less than 1 indicating the errors in the data are large relative to the amount of data available.

Fig. 8.22 shows the fit with the data taken in the ranges $m \in (0.01, 0.05)$, $\beta \in (0.5, 1)$, which gives critical exponents

[2]Courtesy of S. Hands

$$\begin{aligned} \beta_c &= 0.777(23) \\ \beta_m &= 1.09(10) \\ \delta &= 2.344(117) \end{aligned} \tag{8.3}$$

and the corresponding exponents $\eta = \frac{5-\delta}{1+\delta}$ and $\nu = 2\beta_m/(1+\eta)$ given by

$$\begin{aligned} \eta &= 0.796(46) \\ \nu &= 1.214(116) \end{aligned} \tag{8.4}$$

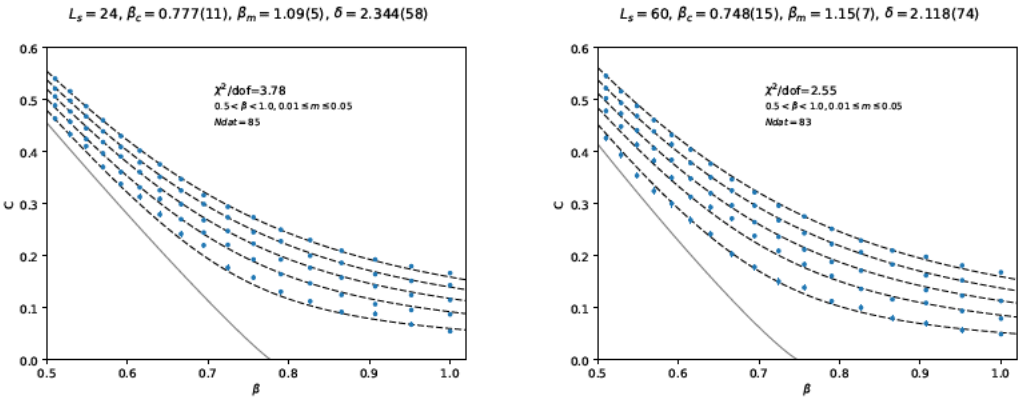

FIGURE 8.22: Quenched Wilson. Mass range $m = [0.01, 0.5]$. Data range $\beta = [0.5, 1]$. Left panel: Zolotarev $L_s = 24$. Right panel: HT $L_s = 60$.

Although the goodness of fit value χ^2/dof is an important parameter and improves from case qwz1, defined below, from case qwz2 by changing the window of reconstruction with the addition of the $m = 0.005$ data, looking at the data (left panel, fig. 8.23) suggests we should not consider this parameter blindly. In particular, if some data region is overprescribed (small error bars and lots of localised data points leading to values much greater than 1) and some data region is underprescribed (large error bars and few data points leading to values much less than 1), these effects may cancel to misleadingly good (close to 1) goodness of fit values. And hence we must be judicious in choosing our data ranges. It was with this in mind that qwz1 was singled out for representative presentation above.

Corresponding to the seven Zolotarev cases with $L_s = 24$ plotted in the left panels of figs. 8.22 through 8.28, the right panels hold plots with HT $L_s = 60$ cases. As has been pointed out with staggered formulations [1], the calculation of the exponents is sensitive to the window used for the reconstruction, although ballpark figures are reasonably

id	L_s	β	m	β_c	β_m	δ	gof	gof_2	N_d
qwz1	Z24	0.5-1.0	0.01-0.05	0.777(11)	1.09(5)	2.344(58)	3.782	0.945	85
qwz2	Z24	0.5-1.0	0.005-0.05	0.810(12)	1.22(5)	2.231(51)	3.984	0.987	101
qwz3	Z24	0.5-1.0	0.01-0.04	0.813(15)	1.20(7)	2.225(68)	2.266	0.567	68
qwz4	Z24	0.5-0.99	0.005-0.05	0.837(14)	1.32(6)	2.131(52)	3.044	0.761	95
qwz5	Z24	0.5-0.99	0.01-0.05	0.800(13)	1.18(6)	2.248(61)	2.867	0.717	80
qwz6	Z24	0.5-1.0	0.02-0.05	0.739(12)	0.96(5)	2.474(76)	3.396	0.849	68
qwz7	Z24	0.5-0.99	0.02-0.05	0.762(15)	1.05(7)	2.361(81)	2.570	0.643	64
qwz8	Z24	0.5-0.92	0.01-0.05	0.819(16)	1.25(7)	2.185(65)	2.12	-	75
qwh1	HT60	0.5-1.0	0.01-0.05	0.748(15)	1.15(7)	2.118(74)	2.55	0.638	83
qwh2	HT60	0.5-1.0	0.005-0.05	0.752(15)	1.37(8)	1.908(56)	8.76	2.19	100
qwh3	HT60	0.5-1.0	0.01-0.04	0.813(24)	1.46(12)	1.833(80)	1.72	0.43	66
qwh4	HT60	0.5-0.99	0.005-0.0.05	0.750(15)	1.37(8)	1.926(59)	9.03	2.26	95
qwh5	HT60	0.5-0.99	0.01-0.05	0.756(16)	1.19(8)	2.097(77)	2.09	0.523	79
qwh6	HT60	0.5-1.0	0.02-0.05	0.708(16)	0.94(8)	2.377(109)	2.58	0.645	66
qwh7	HT60	0.5-0.99	0.02-0.05	0.714(18)	0.96(8)	2.375(118)	1.91	0.477	63
qwh8	HT60	0.5-0.92	0.01-0.05	0.771(18)	1.25(9)	2.033(79)	1.9	-	75

TABLE 8.1: Critical exponents. Numbers in brackets are the errors. Goodness of fit $gof \equiv \chi^2/dof$.

consistent (within error bars) for both Zolotarev and HT formulations, although there is better consistency for the Zolotarev formulation.

With the removal of the $m = 0.05$ curve, cases qwz3 and qwh3 nominally provide the best results respectively, although it should be noted that removing the $m = 0.01$ curves also improves the nominal results for cases qwz7 and qwh7.

In the 6th and 7th cases, where mass ranges of 0.02-0.05 are chosen and where it is thought the HT60 cases are also reasonably well L_s-converged, the HT exponents still differ from the Zolotarev generated exponents. They should be near identical with sufficiently good statistics, and we conclude that more data points are needed to improve the consistency of the results.

It appears from looking at the data that the errors are smaller than they should be. There are kinks in the constant mass curves, which the error bars suggest are real, and we may presume are not. Scaling the errors σ_i in eqn.8.2 does not change the exponent values, but does scale the error values of those exponents, and also the goodness of fit. As such we may work backwards to find an inferred error in the source data. For example, the error scaling required to find $gof = 1$ for case qwz1 is 1.945, whereas the scaling for case qhz1 is 1.598.

Using unweighted least squares, and working backwards to estimate the error we have for qwz1, $\beta_c = 0.808(20)$, $\beta_m = 1.20(8)$, $\delta = 2.257(80)$, and for qwh1, $\beta_c = 0.752(23)$, $\beta_m = 1.18(11)$, $\delta = 2.115(103)$, in reasonable agreement with the weighted versions. It would seem to be a matter of taste at this juncture whether using weighted, with its

unmatched assumptions of equal variance in the data points, is a better choice than unweighted.

We also note in passing that [63] investigated strongly coupled quenched QED in 4d and found critical exponents $\beta_m = 0.8(1)$ and $\delta = 2.2(1)$, who further noted the narrowness of the window around the critical point for which the EoS holds.

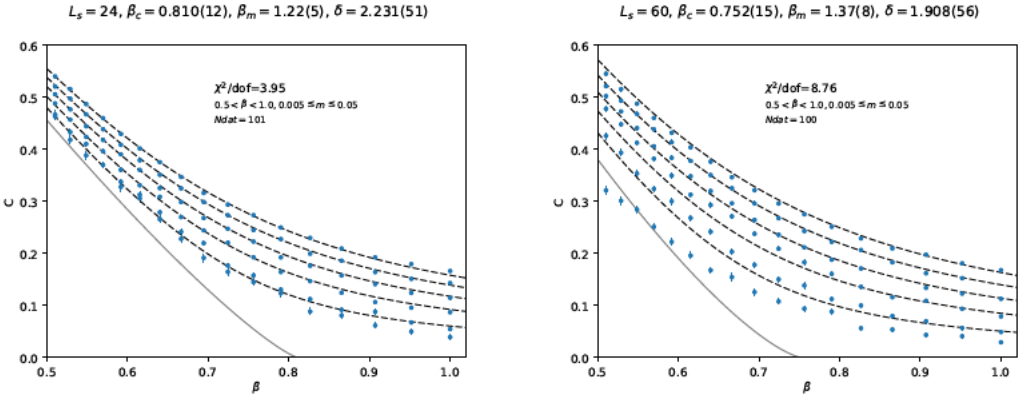

FIGURE 8.23: Quenched Wilson. Window: Mass range $m = [0.005, 0.05]$. Data range $\beta = [0.5, 1]$. Left panel: $ZL_s = 24$. Right panel: HT $L_s = 60$.

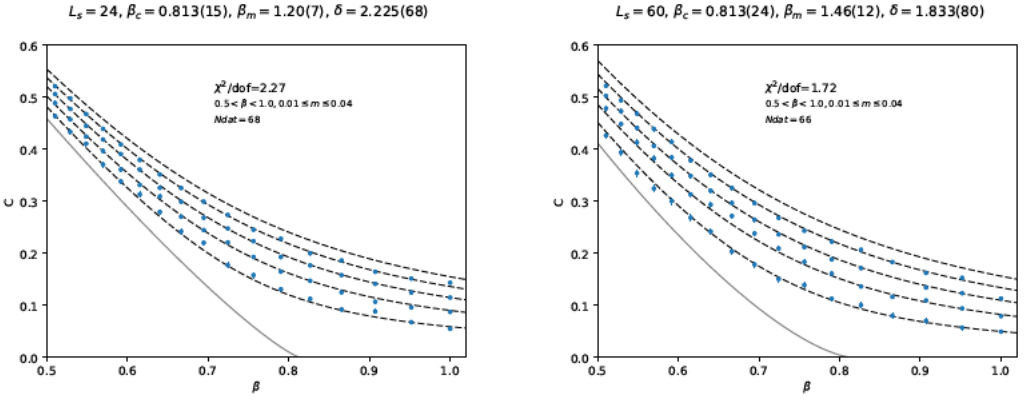

FIGURE 8.24: Quenched Wilson. Window: Mass range $m = [0.01, 0.04]$. Data range $\beta = [0.5, 1]$. Left panel: $ZL_s = 24$. Right panel: HT $L_s = 60$.

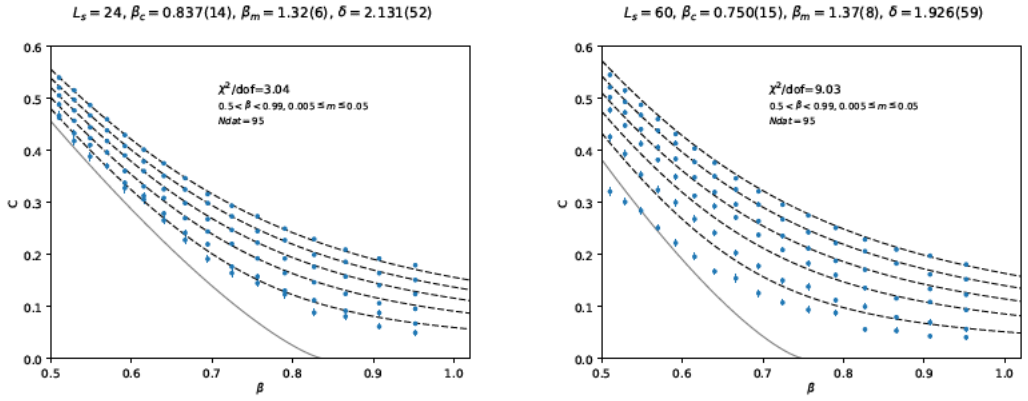

FIGURE 8.25: Quenched Wilson. Window: Mass range $m = [0.005, 0.05]$. Data range $\beta = [0.5, 0.99]$. Left panel: $ZL_s = 24$. Right panel: HT $L_s = 60$.

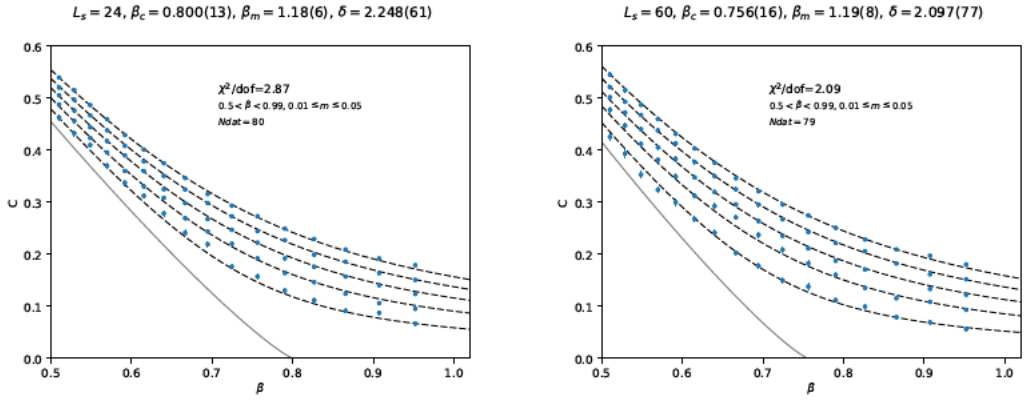

FIGURE 8.26: Quenched Wilson. Window: Mass range $m = [0.01, 0.05]$. Data range $\beta = [0.5, 0.99]$. Left panel: $ZL_s = 24$. Right panel: HT $L_s = 60$.

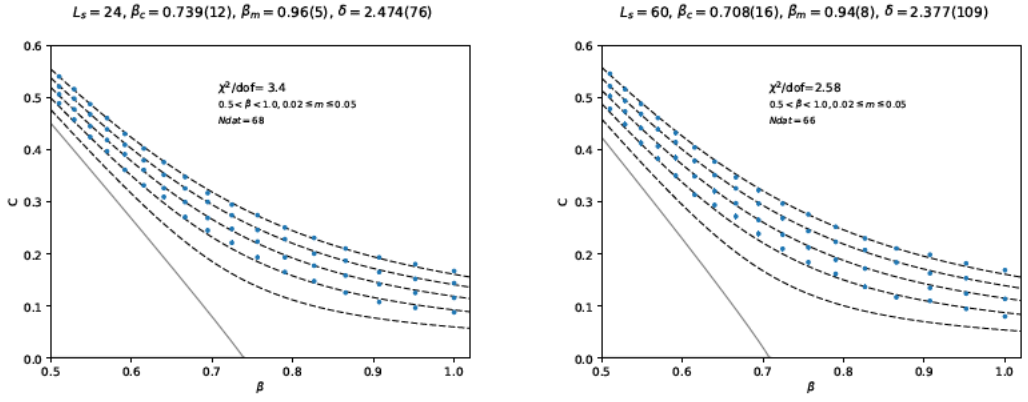

FIGURE 8.27: Quenched Wilson. Window: Mass range $m = [0.02, 0.05]$. Data range $\beta = [0.5, 1]$. Left panel: $ZL_s = 24$. Right panel: HT $L_s = 60$.

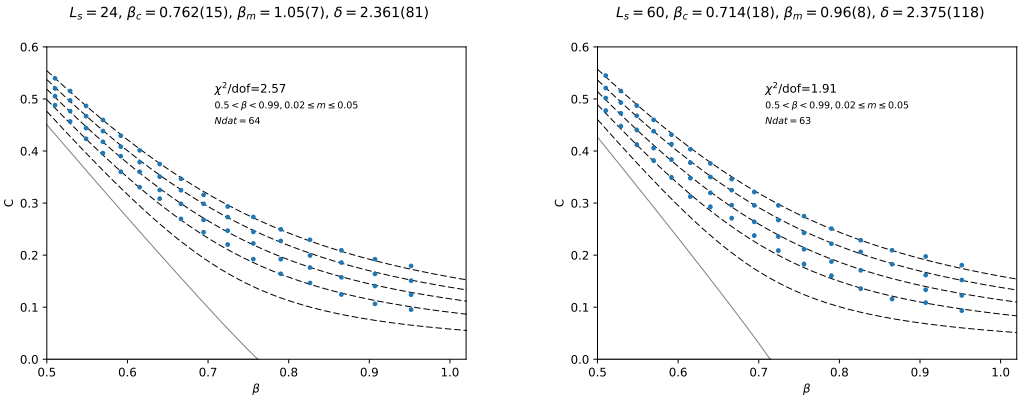

FIGURE 8.28: Quenched Wilson. Window: Mass range $m = [0.02, 0.05]$. Data range $\beta = [0.5, 0.99]$. Left panel: $ZL_s = 24$. Right panel: HT $L_s = 60$.

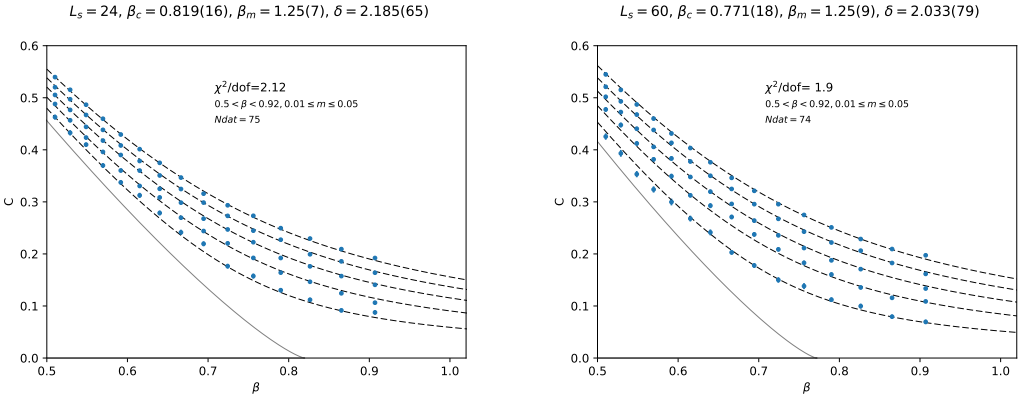

FIGURE 8.29: Quenched Wilson. Window: Mass range $m = [0.01, 0.05]$. Data range $\beta = [0.5, 0.92]$. Left panel: $ZL_s = 24$. Right panel: HT $L_s = 60$.

8.10 Shamir EOS

We turn to the EoS for the Shamir kernel, using the HT $L_s = 300$ formulation. While the first case, qsh1, matches the Wilson cases reasonably well, reducing the analysis window from the weak coupling side appears to reduce δ and increase β_m in a manner not matched by the Wilson cases. Although the data is noisier than for the Wilson cases and the errors relatively large, one would be inclined towards the qsh3/qsh4 cases with $\beta_c \approx 0.9$, $\beta_m \approx 1.48$ and $\delta = 1.84$. However, there is no reason to expect the exponents to match for the non-physical quenched cases, and we shoouldn't be disheartened.

We also consider a couple of cases, qsm3 and qsm7, in which we use a domain wall height of $M = 0.5$. The critical value has shifted to the left, to roughly $\beta_c = 0.6$, δ has increased again to values similar to the Wilson cases, and β_m has dropped lower than both the Shamir and Wilson $M = 1$ cases.

More usefully, we observe that the curves have sharpened significantly, suggesting we are more zoomed in, with the reduced value M, lessening the requirements on $m \to 0$ to find an analysis window independent set of of results.

id	M	β	m	β_c	β_m	δ	gof	N_d
qsh1	1.0	0.5-1.2	0.01-0.05	0.840(12)	1.20(6)	2.099(52)	2.07	100
qsh2	1.0	0.5-1.1	0.01-0.05	0.884(17)	1.39(8)	1.915(64)	1.71	90
qsh3	1.0	0.5-1.0	0.01-0.05	0.904(20)	1.48(9)	1.838(68)	1.63	85
qsh4	1.0	0.5-0.99	0.01-0.05	0.905(22)	1.48(10)	1.843(77)	1.68	80
qsh5	1.0	0.54-1.0	0.01-0.05	0.908(25)	1.50(13)	1.839(88)	1.72	75
qsh6	1.0	0.54-1.1	0.01-0.05	0.884(21)	1.39(11)	1.931(84)	1.8	80
qsm3	0.5	0.5-1.0	0.01-0.05	0.599(10)	0.91(10)	2.157(125)	6.17	85
qsm7	0.5	0.5-0.95	0.01-0.05	0.625(11)	0.92(11)	2.285(144)	1.87	75

TABLE 8.2: Critical exponents. Numbers in brackets are the errors. $L_s = 300$. Goodness of fit $gof \equiv \chi^2/dof$.

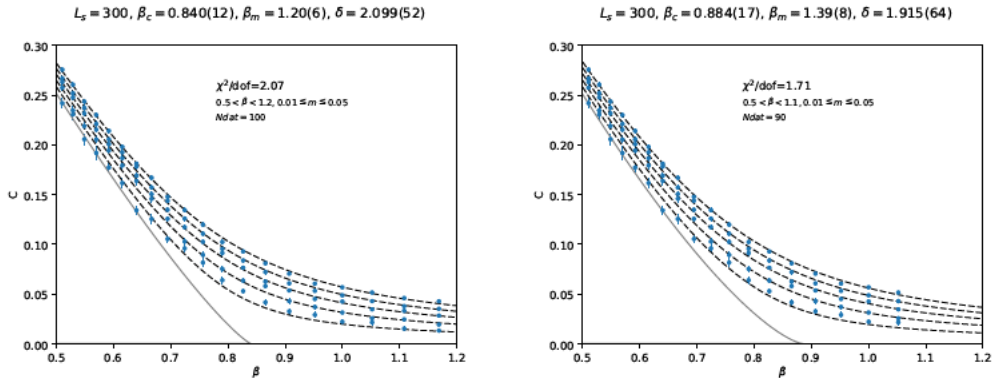

FIGURE 8.30: Shamir. $L_s = 300$. Mass range $m = [0.01, 0.05]$. Left panel: Data range $\beta = [0.5, 1.2]$. Right panel: Data range $\beta = [0.5, 1.1]$.

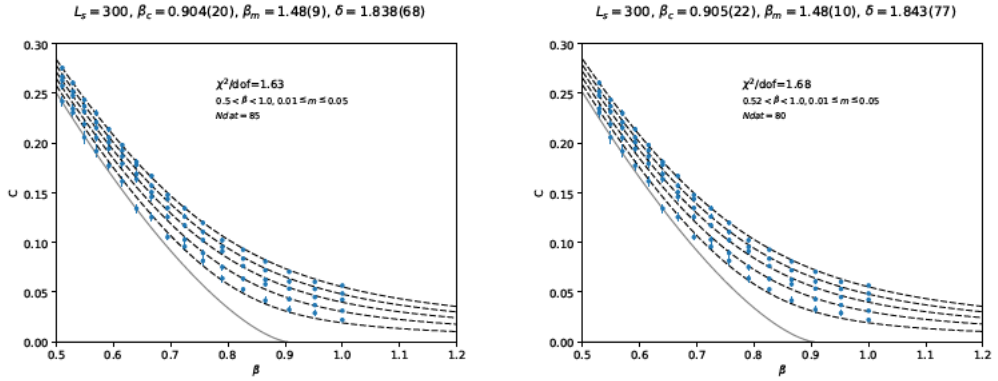

FIGURE 8.31: Shamir. $L_s = 300$. Mass range $m = [0.01, 0.05]$. Left panel: Data range $\beta = [0.5, 1.0]$. Right panel: Data range $\beta = [0.52, 1.0]$.

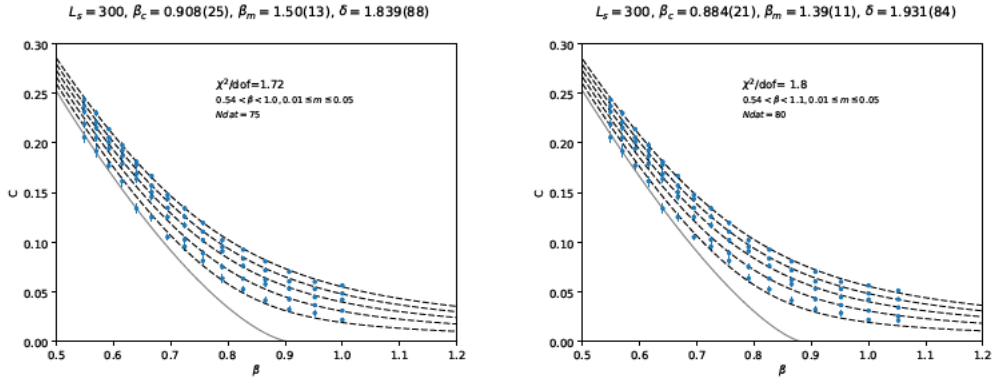

FIGURE 8.32: Shamir. $L_s = 300$. Mass range $m = [0.01, 0.05]$. Left panel: Data range $\beta = [0.54, 1.0]$. Right panel: Data range $\beta = [0.54, 1.1]$.

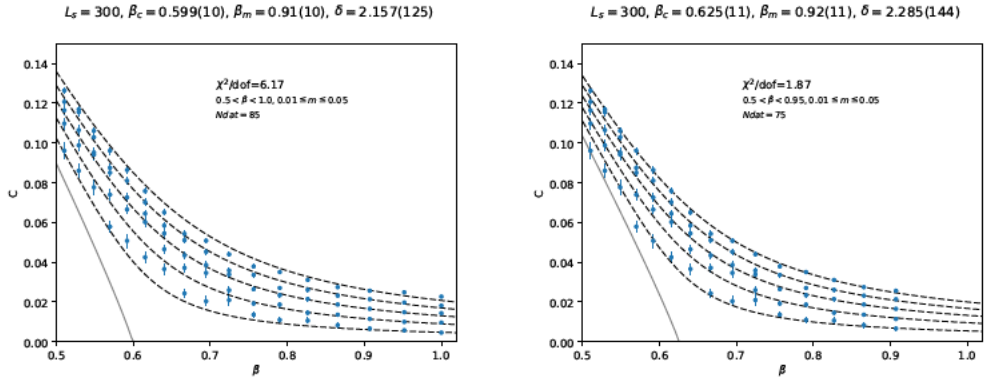

FIGURE 8.33: Shamir. $L_s = 300$. Domain wall height $M = 0.5$. Mass range $m = [0.01, 0.5]$. Left panel: Data range $\beta = [0.5, 1.0]$. Left panel: Data range $\beta = [0.5, 0.95]$.

8.11 Summary

Although quenched measurements are not physical, they still provide a good foundation in which to explore numerical techniques. Importantly in this section we went through the prototype analysis to be carried out on the dynamical fermions in the next chapter. The importance of the eigenvalue range of the kernel was highlighted, and most significantly the unboundedness of the largest Shamir kernel eigenvalue was established which is part of the explanation of why the Thirring model is as computationally challenging as it is. That the Wilson formulation is a computationally advantageous method rather than the Shamir formulation was indicated, although we will continue to compare both methods. That the Shamir and Wilson kernel formulations should be physically equivalent was not borne out in the EoS results, although the statistical challenges of the associated calculational methods were highlighted, especially the difficulty of getting critical exponents independent of the chosen window of analysis. Disappointed by the lack of apparent physical equivalence it is hoped that this is either a non-physical consequence of the quenched approximation or due to insufficient data for the statistical analysis.

Also, computational costs of the methods were considered and although not a fair comparison, in outcome from this data it would be recommended to use the Wilson Zolotarev method rather than the Shamir HT scheme for the the condensate measurement. It was also shown that there is potential benefit to be gained from using a smaller value of the domain wall height M.

Chapter 9

Dynamic Overlap Condensate Results

We now look at results in which the auxiliary field is dynamically generated using the RHMC algorithm [57] as set out in chapter 6. The FORTRAN90 code, available on github [64], was adjusted in this work for use with the HT Wilson domain wall formulation. This required the change of the domain wall operator from eqn. 3.40 to eqns. 3.45, 3.47, and the addition of extra force terms accompanying those changes, also in chapter 6. A corresponding new condensate measurement routine was also implemented. All results are on a $12^2 \times 12$ mesh unless otherwise stated. Extensive work [3, 50, 65] has demonstrated the numerical advantage of the γ_3 twisted mass formulation, and hence that is used in the following.

We provide some validation of the code, before looking at the autocorrelation of the condensates and the acceptance rates in the hamiltonian dynamics steps. Then following a similar approach as in the quenched case we look at the kernel eigenvalue extrema and condition numbers. Then we look at the L_s-convergence of the condensates before moving on to the evaluation of the equation of state for the different formulations. Finally we look at the overall computational cost of the methods.

9.1 Validation

Validation of the Wilson kernel domain wall measurement routine was achieved by checking the condensate results could be reproduced using the direct overlap formulation as shown in Figure 9.1. The results aren't identical due to the use of noisy estimators (see section B.3) and the use of the left formulation of the direct overlap (eqn. 4.16), rather than the right formulation (eqn. 4.15) which has exact correspondence to the domain wall formulation used in the software. Nevertheless, it indicates that the results

are aligned, and that we may proceed to use the methods interchangably, and more particularly to take fields generated with the domain wall formulation and remeasure with overlap formulations.

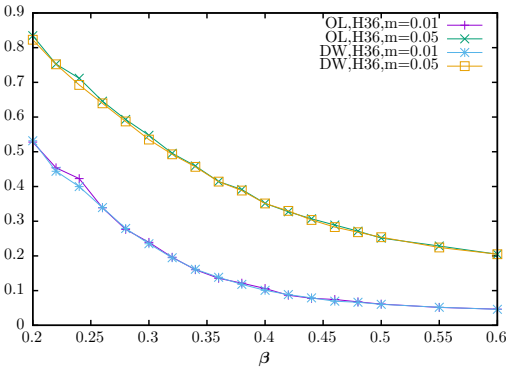

FIGURE 9.1: Condensate measurements using domain wall (DW) and overlap (OL) formulations. Auxiliary fields generated with domain wall formulation. H36 denotes HT scheme with $L_s = 36$.Twisted mass formulations are used in all cases.

Validation of the generation of the auxiliary fields is more difficult, but we gain some confidence from consideration of the history of $h_g = 0.5\beta\theta^2_{i,\mu}/N_v$ calculated at the end of each RHMC trajectory. Plots of the h_g history with cold starts ($A_\mu = 0$ at beginning of simulation) are shown in Figure 9.2 and we see that choosing different parameters leads to different times to reach equilibrium (thermalisation). The stronger the coupling, the slower it is to reach equilibrium. When they have reached equilibrium, we see that it is still auto-correlated.

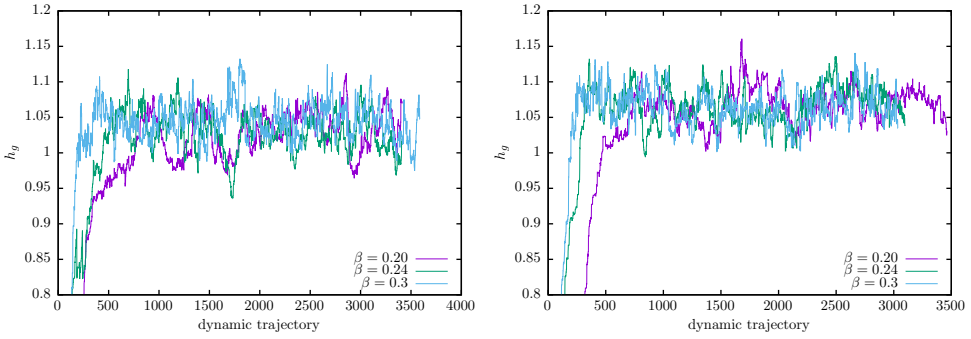

FIGURE 9.2: h_g calculated at the end of each dynamic trajectory. Average trajectory length is 0.5 with 10 steps. Left panel: $m = 0.01$. Right panel: $m = 0.05$.

Following [50] we show the averages of h_g, plotted against β, in Figure 9.3. The left panel takes the averages from trajectory 1000, and the right panel from trajectory 2000. The right panel, despite significantly less data, seems to match the trend of [50] in which at coupling strengths stronger than the critical point there is an upturn in the

avarage value. This is less clear in the left panel data. We now go on to look at the autocorrelation in the data.

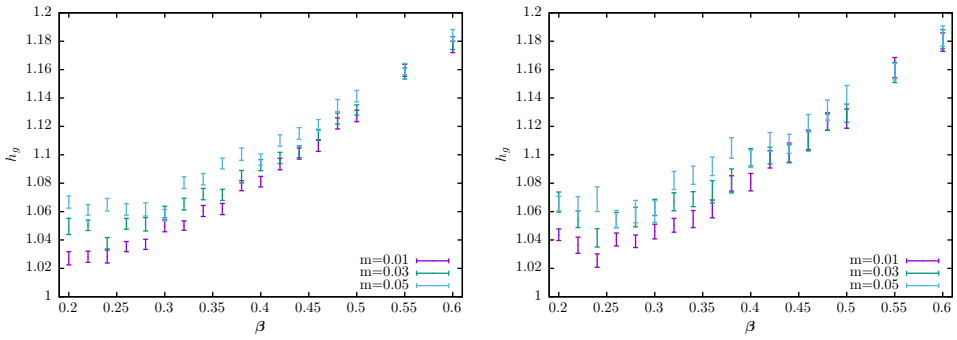

FIGURE 9.3: h_g plotted with standard deviation. Left panel: Averages taken from trajectories 1000-3000. Right panel: Averages taken from trajectories 2000-3000.

9.2 Autocorrelation

Fig. 9.4 shows the autocorrelation of the auxiliary field metric h_g for varying β and m. There is not sufficient data for numerically precise statements, as indicated by the difference in results between the left and right panels. However, it would appear that the autocorrelation increases strongly with coupling strength, and the impact of mass being inconclusive. As in the previous section, equilibirium is deemed to be achieved when the average value of h_g reaches a constant value.

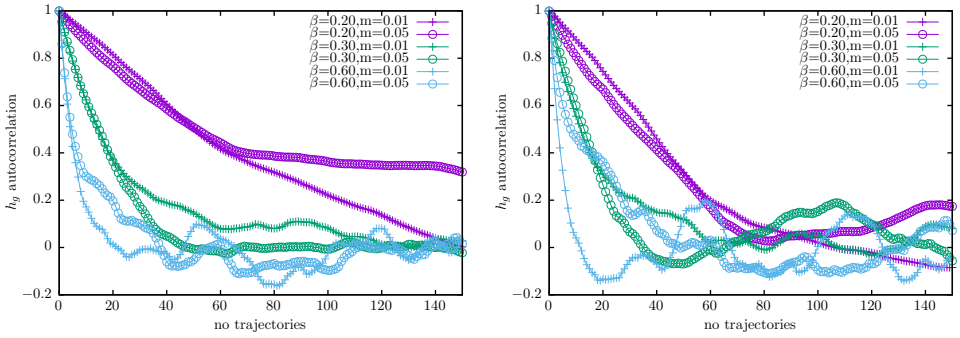

FIGURE 9.4: Autocorrelation time of h_g. Time scale is the number of hamiltonian trajectories. Left panel: calculated from trajectories 1000-3000. Right panel: calculated from trajectories 2000-3000.

We further look directly at the histories of some condensates for the Wilson formulation in fig. 9.5 and for the Shamir formulation in fig. 9.6. The hamiltonian dynamics steps are the same for both Shamir and Wilson cases, using a timestep of 0.05 and an average number of 10 steps before the acceptance step[1]. The only cases which differ are the

[1]There is a fixed probability of the trajectory coming to an end after each dynamic step.

$\beta = 0.20$ and $\beta = 0.22$ Wilson cases which use an average number of 9 steps. There appears to be a stark increase in the autocorrelation in the strongly coupled Wilson case. Fig. 9.7 confirms this, calculating the autocorrelation directly, with the Shamir case in the left panel, and Wilson case in the right panel. Although the β value is smaller for the Wilson case, as we will see more clearly in chapter 10, we probably do not want to push the β values significantly lower. We also note that it appears to be mass independent for the given range.

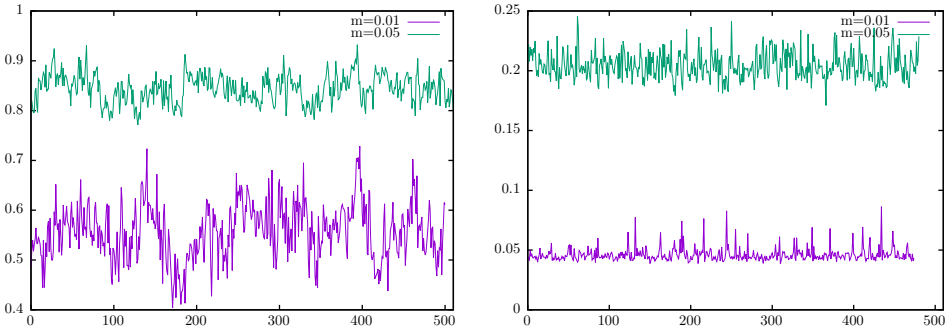

FIGURE 9.5: Condensate histories for Wilson with $L_s = 36$. Left panel: $\beta = 0.2$. Right panel: $\beta = 0.6$

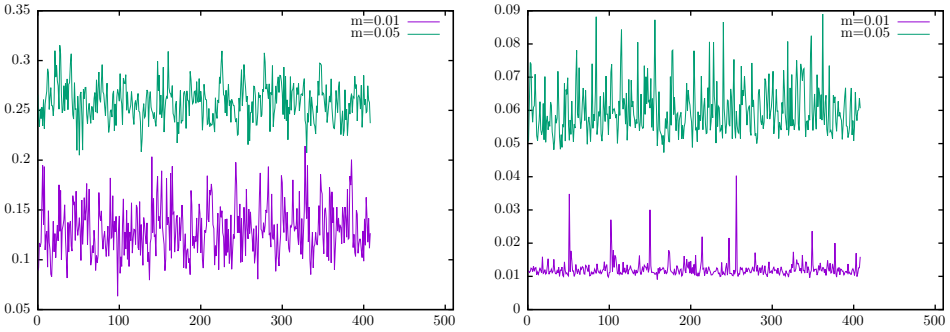

FIGURE 9.6: Condensate histories for Shamir with $L_s = 96$. Left panel: $\beta = 0.26$. Right panel: $\beta = 0.6$

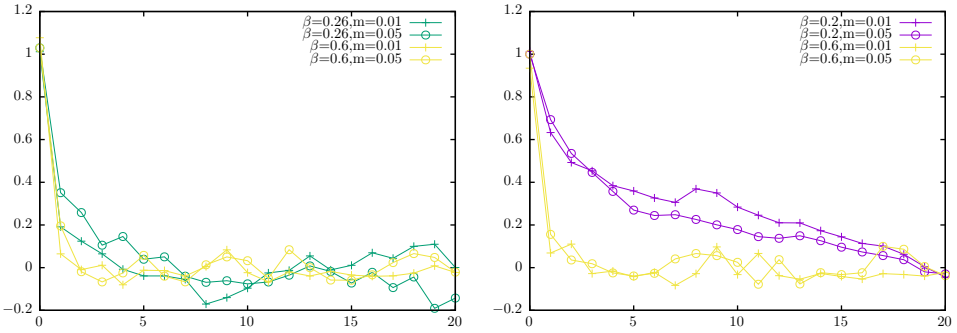

FIGURE 9.7: Condensate autocorrelation. Left panel: Shamir, $L_s = 96$. Right panel: Wilson, $L_S = 36$.

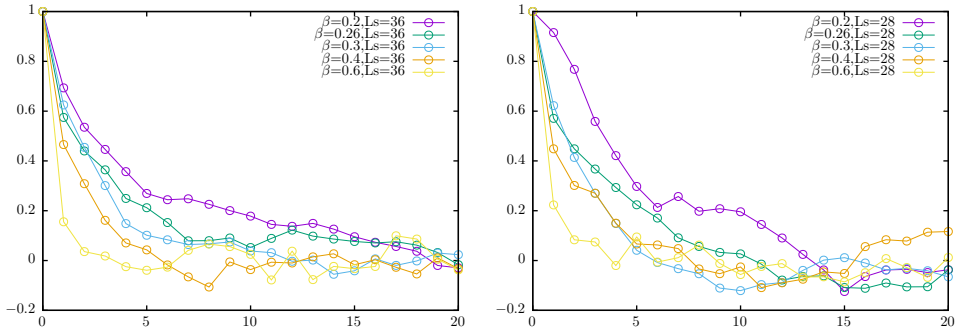

FIGURE 9.8: Condensate autocorrelation. Left panel: Wilson, $L_s = 36$. Right panel: Wilson, $L_s = 28$.

We compare L_s values of 36 and 28 in the left and right panels of fig. 9.8. While it appears that there is mostly no dependence, the $\beta = 0.2$ lines differ, although it is difficult to conclude that this difference would not vanish with more data. For the condensate autocorrelation, the Shamir measurements were based on trajectories 500-2500, and the Wilson measurements on trajectories 1000-3000, and measurements of the condensate taken every 5 trajectories.

While with correlated data the mean data continues to be calculated in the same way we should no longer assume reliance on the usual calculation of the standard error $se = \sigma/\sqrt{(N)}$, although in the condensate measurements with the Shamir kernel we do exactly that since the correlation decay rate is large. A formal remedy to the error calculation is to multiply the error of uncorrelated formula by a timescale based on the correlation, $se = \sqrt{\frac{2\tau}{N}}\sigma$ where τ is the correlation time scale as described in appendix B.4.

9.3 Acceptance Rates

We look at the acceptance rates of the Monte Carlo step in fig. 9.9. The hamiltonian dynamics controls are the same for both Wilson and Shamir setups as decribed in section 9.2 above. It is clear that under these conditions the Wilson formulation has a lower acceptance rate. In the weaker coupling range, the acceptance rate is between 0.9 and 0.95 for the Wilson formulation and between 0.95 and 1 for the Shamir formulation, and dropping to 0.65 to 0.75 and 0.8 to 0.95 respectively at the stronger coupling end of the plots. The acceptance rates make a difference to the autocorrelation, but we would suggest that this factor is not sufficient alone to provide a complete explanation. How far a single trajectory "moves" the auxiliary field relative to the starting point also controls the autocorrelation time. Hence we suggest that for the Wilson case the auxiliary field

generated at the end of a single trajectory is relatively closer to it's starting point than for the Shamir case. The trajectory distance may be increased by taking more steps.[2]

It is also notable that the acceptance rate decreases with L_s. This could be a L_s volumetric effect, due to the momentum marching term in the hamiltonian dynamics step, $\dot{P} = -\frac{\partial S[A]}{\partial A}$, eqn. 6.1b, getting larger since the action[3] seems to scale with L_s. Whether it is also connected to the accuracy, or rather the damping effect of lower L_s would be interesting to explore. In this case it might be expected to find the acceptance rate stops decreasing after achieving sufficient L_s.

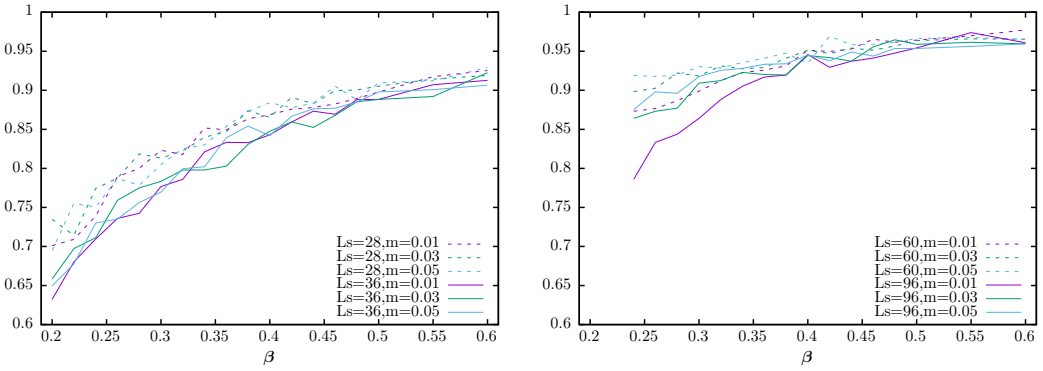

FIGURE 9.9: Acceptance Rate in the Monte Carlo Step. Left panel: Wilson kernel. Right panel: Shamir kernel.

9.4 Eigenvalue Extrema and Condition Number of Kernel

Again it is very useful to look at the eigenvalue range of the kernels. Since the auxiliary fields are now generated dynamically, they are dependent on the L_s extent of the domain wall. When viewed from the overlap perspective this is not considered an extra physical dimension, but merely an expression of the level of accuracy of approximation. Figure 9.10 shows the maximum and minimum eigenvalues for the Shamir kernel, and we see that the average values are largely independent of either the mass or the value of L_s. The bars are for the maximum and minimum rather than the standard deviation. At least 100 fields were used for each data point. As with the quenched non compact case, the eigenvalues are no longer bounded from above and there is a significant increase in the maximum eigenvalue beyond the critical β value, roughly 0.3. The compact values are, however, bounded from above, and also have much larger smallest eigenvalues with very little variance. This parallels the qualtitative behaviour of the quenched field kernels, although we have not taken β to strong enough couplings to confirm that the maximum value will fall again.

[2]Simplectic integrators bind the solution to a shadow hamiltonian, limiting the long term accumulation of time step discretisation errors.

[3]At least the variance of the action

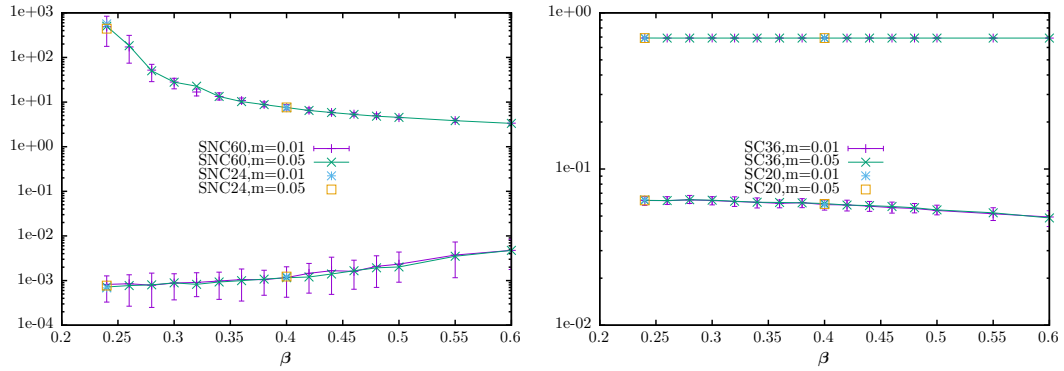

FIGURE 9.10: Min/max Shamir kernel eigenvalues. Left panel: Noncompact. Right panel: Compact (using non-compact generated auxiliary fields)

Plots for the Wilson kernel are shown in Figure 9.11, again with the bars showing the data point maxima and minima rather than standard deviation. These eigenvalues provide a guide for choosing the Zolotarev range to be used in the overlap operator, unless the range is to be reset for every auxiliary configuration. Since the latter is costly, especially for the dynamic step, it is generally preferable to choose a fixed range. Although the eigenvalues are strictly only bounded below by zero, a practical range can be identified from the plots. In practice, we have found stricter adherence to the upper bound is more important to the evaluation of the condensate than the lower bound.

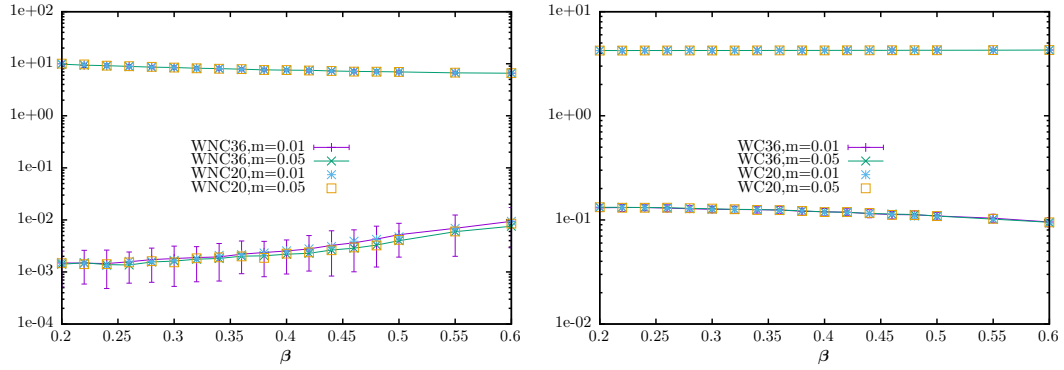

FIGURE 9.11: Min/max Wilson kernel eigenvalues. Left panel: Noncompact. Right panel: Compact (using non-compact generated auxiliary fields)

The independence from L_s, at least for all L_s above an unexplored lower bound, combined with our a priori belief that the condensate measurements will require significantly higher L_s values, suggests the possibility of using different L_s values for the sea-fermions (the Dirac operator used in the generation of the auxiliary fields) and the valence fermions (the Dirac operator used for the condensate measurements).

9.5 Eigenvalues of Overlap Operator

The condition number for the Wilson kernel overlap operator is briefly considered via fig. 9.12 where the smallest eigenvalues are plotted. The largest eigenvalues in all instances are just short of 1. Again, the minimum eigenvalue is constrained by the mass term, although in the HT36 case is only just reaching this limit as $\beta \to 0.24$. The same limits apply for the Z30 case, but the minimum eigenvalues are lower when the calculations are with m=0 (still with the massive auxiliary fields) compared with the HT36 case. Similar to the quenched case, when setting the valence mass to 0, the higher auxiliary mass terms correspond to a reduction in the lowest eigenvalue. A similar situation is shown in the left panel of Fig. 9.13.

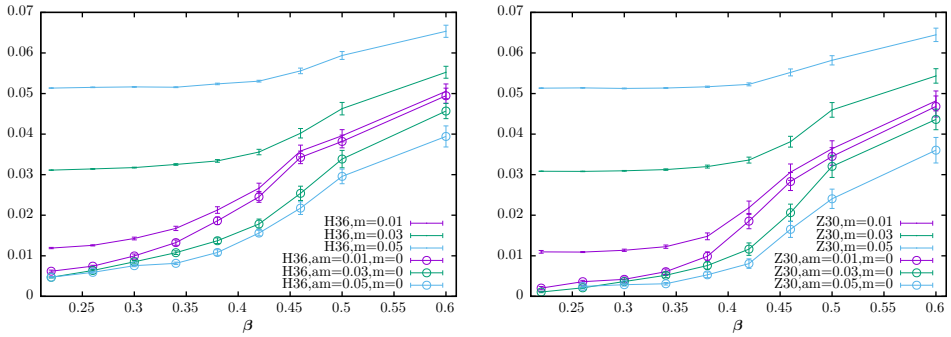

FIGURE 9.12: Wilson Overlap Minimum Eigenvalues. $am = 0$ denotes the mass that the auxiliary fields were generated with, if different from the measurement mass m. Left panel: HT approximations. Right panel: Zolotarev approximations.

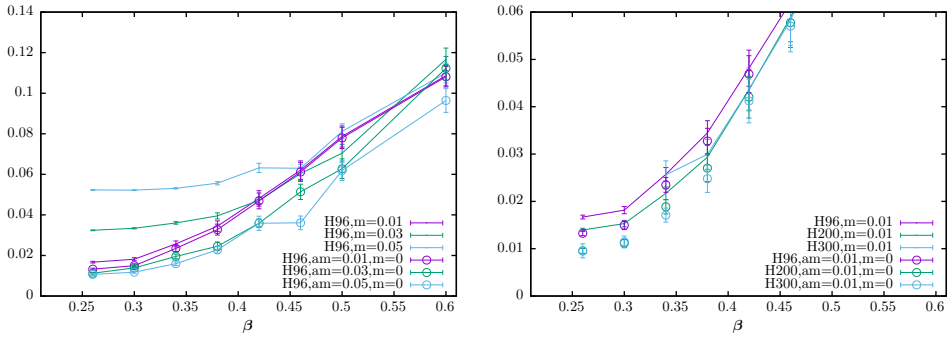

FIGURE 9.13: Shamir Overlap Minimum Eigenvalues. $am = 0$ denotes the mass that the auxiliary fields were generated with, if different from the measurement mass m. Left panel: HT approximation with $L_s = 96$. Right panel: HT appromimation varying L_s.

9.6 Computational Cost of Overlap Operator

We again look at the Wilson Dirac operator count required by inversion of the overlap operator. As in section 8.4 the total count is given by $N_t = 4N_oN_i$ for the direct evaluation using the Wilson kernel, and the indirect formulation has $N_t = 2N_sL_s$ which is used for the Shamir kernel. The outer loop operation count for the Wilson inversion is in fig. 9.14, and find the count in accordance with the condition number for the H36 cases. For the Z30 cases this only holds for $m = 0.03$ and $m = 0.05$. Fig. 9.15 shows the inner count in the left panel, indicating the significant increase in cost with the Zolotarev formulation, especially at strong coupling. For the HT36 case there is essentially no difference for either mass term, or whether the calculation matched the auxiliary field mass. However there is a little auxiliary mass dependence in the Zolotarev cases. The right panel shows the average count for the indirect Shamir loop at HT200 for which setting the measurement mass to zero reduces the computational cost. Further Shamir plots are in the left panel of fig. 9.16. The right panel gives the total costs in terms of number of calls to the Wilson Dirac operator per inversion of the overlap operator. The absence of the HT300 Shamir plots for the $m = 0.01$ (in the 12hr computational window allowed[4] these did not complete - no cases were run for Shamir at $\beta = 0.24$ for this plot) highlights that there are more factors than just this count. Nevertheless, they are a useful indicator, and support the use of the direct Wilson Zolotarev formulation.

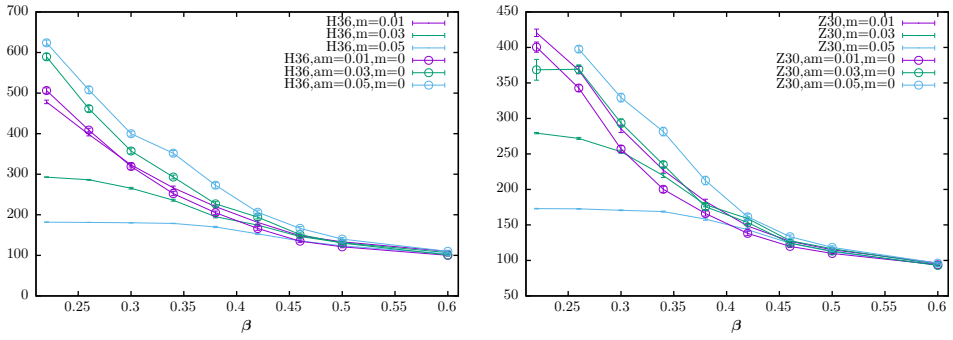

FIGURE 9.14: Operator counts for inversion. Outer loop (CG iterations) counts for overlap operator with Wilson kernel. Left panel: HT36. Right panel: Z30.

[4]Simulations were run on the Skylake nodes of the Dirac supercomputing cluster.

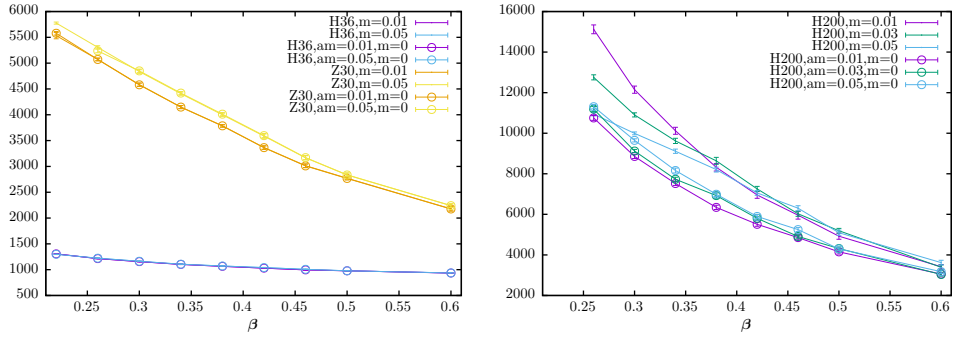

FIGURE 9.15: Operator counts of inversion. Left panel: Z30 Wilson overlap (direct calculation) inner loop (multishift CG iterations) operator count. Right panel: HT200 Shamir overlap (indirect calculation) loop count (multishift CG iterations).

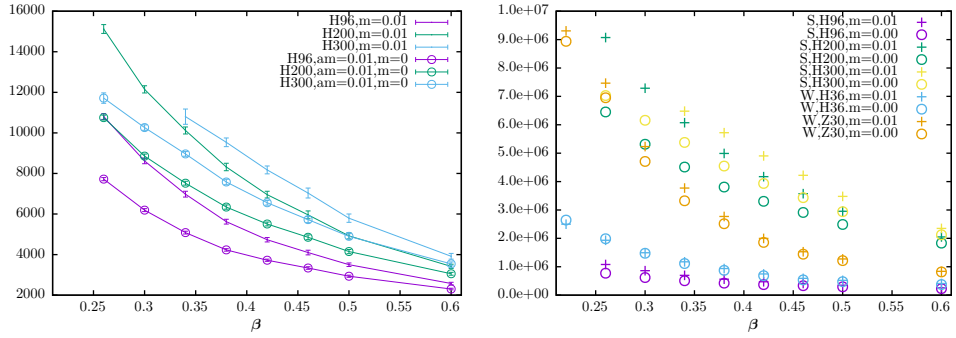

FIGURE 9.16: Operator counts of inversion. Left panel: Shamir overlap (indirect calculation) loop count (multishift CG iterations). Right panel: Total count of applications of Wilson Dirac operator for indirect Shamir overlap and direct Wilson overlap operators.

9.7 Shamir Condensates

Following in the footsteps of [46, 50] we look again at the condensates evaluated with the Shamir kernel, but here we continue to use the smaller $12^2 \times 12$ mesh size rather than the $16^2 \times 16$ meshes in those works. This is computationally beneficial not only from the decreased mesh size, but also the expected decrease in eigenvalue range of the kernel, as noted from the quenched cases (see fig. 8.5). Although diminished, the L_s-limit challenges remain, and indeed the condensates plotted in the left panel of fig. 9.17, which include L_s values of 24, 60, and 96 for mass values 0.01, 0.03, and 0.05, do not suggest convergence in the strongly coupled region, even for the larger masses. The right hand panel replots two β values against m reemphasising this. We scale the error bars by a factor of 3 uniformly over the β range, somewhat more than would be suggested by the autocorrelation even in the strong coupling region, but the lack of smoothness in the curves suggests smaller error bars would be highly improbable.

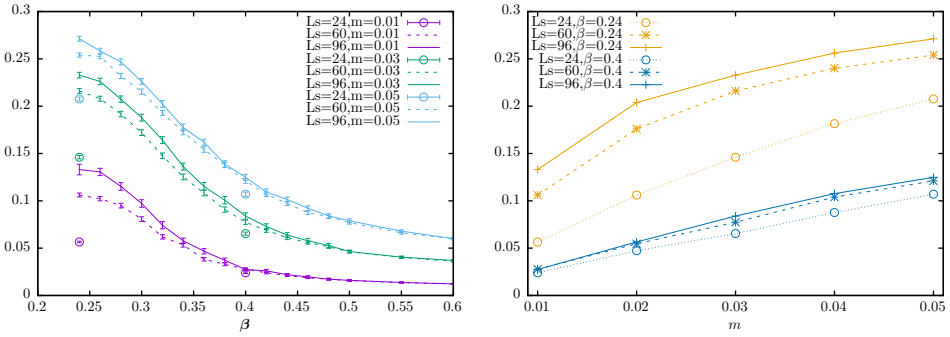

FIGURE 9.17: Dynamic condensate plots with the Shamir kernel varying L_s. Left panel: C vs β. Right panel: C vs m.

Following the intuition that there may be no requirement for the auxiliary field to be generated with such a stringent L_s value, we look at partially quenched condensates in fig. 9.18. In the left panel, the $\beta = 0.4$ case is considered. Fig. 9.17 indicates that the solution is L_s converged by $L_s = 60$. To the two curves with sea and valence fermions calculated with the same L_s values, are added curves where the valence fermions, and hence the condensate is measured, with a different L_s value. In the first additional curve, the auxiliary fields are generated with $L_s = 24$ and the measurements are made with $L_s = 60$. In the second, we reverse the procedure and generate the auxiliary fields with $L_s = 60$ and measure with $L_s = 24$. Pleasingly, it seems sufficient to use the $L_s = 24$ auxiliary field to capture the converged L_s measurement. On the other hand, there seems to be nothing to be gained from overextending the L_s value of the auxiliary field if it is not to be matched in the measurement. This pattern seems to be matched in the right panel, considering the $\beta = 0.24$ case, although slightly less convincingly at the $m = 0.01$ datapoint, even though the L_s limit has not been reached. Given the high costs of dynamically generating the auxiliary fields, this represents a significant potential in compuational cost cutting.

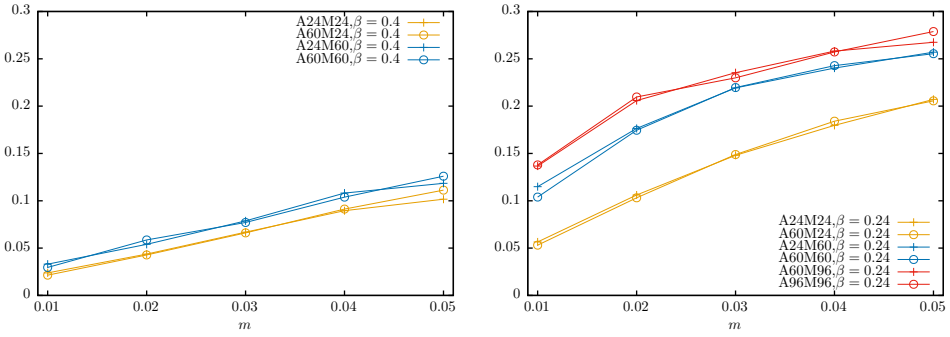

FIGURE 9.18: Partially quenched Shamir condensates. AXMY in the legend denotes the auxiliary fields were generated with $L_s = X$, and the measurements were taken with $L_s = Y$. Left panel: $\beta = 0.4$. Right panel: $\beta = 0.24$.

There is a certain inevitability that utilising different but sufficiently large L_s values for valence and sea fermions should give the same measurement results, given the nature of L_s convergence. Beyond high enough values of L_s the limits of machine precision will be reached. Given any measurements will only ever be wanted to a certain accuracy it seems quite reasonable that different parts of the measurement process require differing levels of accuracy, which is what varying L_s represents, at least when using the domain wall formulation as an equivalent of the overlap operator - the claim that L_s is a parameter of accuracy may not hold for more general domain wall formulations, such as the non-bulk formulation.[5]

So we take our own advice, and choose $L_s = 300$ for the condensate measurements, justified to a certain extent by the apparent convergence in the quenched cases (fig. 8.18) and the kernel accuracy requirements shown in fig. 9.10. We use the auxiliary fields generated with $L_s = 96$, and think the solution should feasibly be close to covering the necessary range. Fig. 9.19 shows the results. The left panel continues to show that the convergence continues well beyond the $L_s = 96$ value even at relatively weak coupling and at the larger mass values. The right hand panel shows the full results, denoted A96M300 (Auxiliary $L_s = 96$, Measurement $L_s = 300$), reemphasizing the same points.

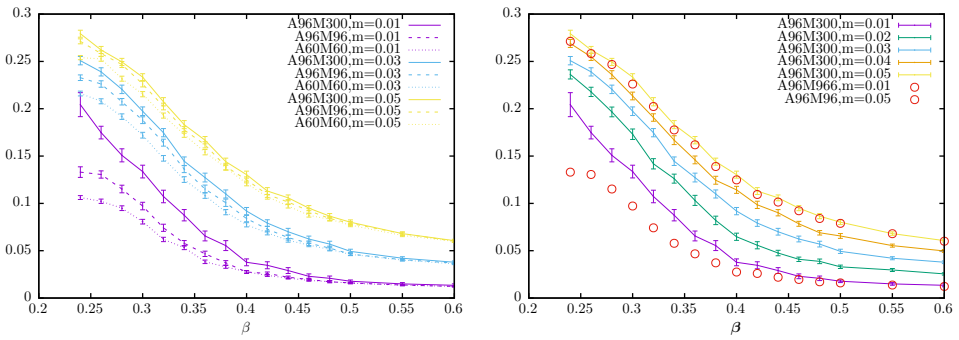

FIGURE 9.19: Partially quenched Shamir condensates. AXMY in the legend denotes the auxiliary fields were generated with $L_s = X$, and the measurements were taken with $L_s = Y$.

Fig. 9.20 vindicates this L_s quenching approach, demonstrating that the A96M300 results are satisfactorily L_s converged, since the results are close enough to being the same as the A60M300 results. The measurements are taken every 10 trajectories of the hamiltonian step (every other auxiliary field used in the non partially quenched results above).

[5] We define the non-bulk domain wall operator to be one in which the auxiliary field is *not* constant in the extra dimension.

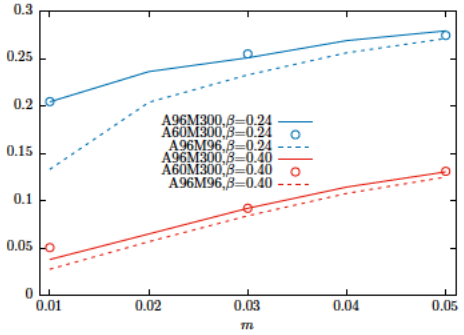

FIGURE 9.20: Partially quenched Shamir condensates. AXMY in the legend denotes the auxiliary fields were generated with $L_s = X$, and the measurements were taken with $L_s = Y$. Plots vs m.

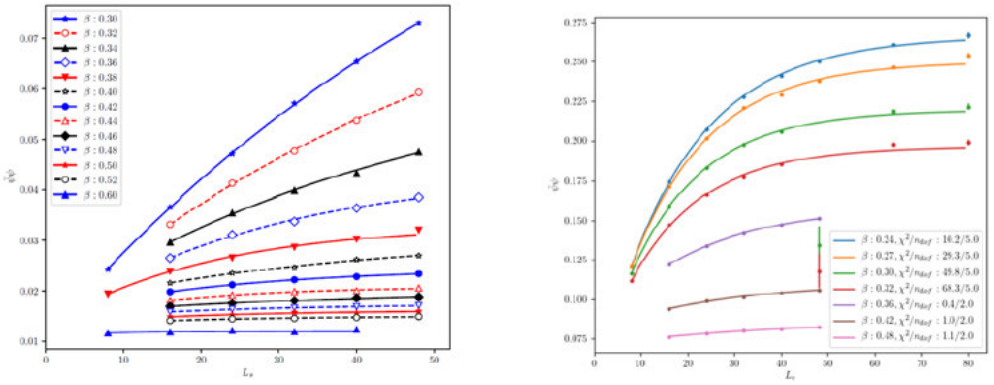

FIGURE 9.21: Reprinted from [7, 8]. The Shamir condensates used in these plots were generated using a 16x16 mesh, with the same code base [64]. Left panel: $m = 0.01$. Right panel: $m = 0.05$.

In fig. 9.21 data from collaborators is reprinted. Convergence plots are provided from [7] in the left panel, and [8] in the right panel. The requirement of large L_s-values had already been amply demonstrated to be beyond the computing resources available. Instead these papers use the extrapolation

$$\langle\bar{\psi}\psi\rangle_\infty - \langle\bar{\psi}\psi\rangle = A(g^2, m)\mathrm{e}^{-\triangle(g^2,m)L_s} \tag{9.1}$$

It was troublingly found that the decay rate coefficient, $\triangle$, goes to zero as $m \to 0$, suggesting that eqn. 9.1 is not a suitable curve fit since this corresponds to the hopefully unreasonable requirement that $L_s \to \infty$ as $m \to 0$. (While this would be the case for any auxiliary field resulting in an overlap kernel with a zero eigenvalue, this would be an exceptional ocurrence.) We worried about the meandering convergence discussed in the quenched results validation section 8.1. What initially appeared to be exponentially convergent according to eqn. 9.1, turned out to require considerably larger L_s. This may

simply be explained by the nature of HT approximation, and the uneven distribution of its accuracy over the kernel eigenvalue range. Alternatively, with the Zolotarev approximation, suitably tuned to the eigenvalue range, one may perhaps more reasonably expect to find convergence of that form eqn. 9.1 but without a vanishing decay rate.

9.8 Wilson Condensates

Plots of the condensate generated with the Wilson condensate are shown in Figure 9.22. The left panel shows measurements of the condensate taken every 5 trajectories over at last 1500 trajectories, with the HT formulation at various L_s. Error bars are shown for the $L_s = 36$ cases but are of similar magnitude for the other L_s curves. The $m = 0.05$ case seems to be well L_s convereged already at $L_s = 20$, and it appears that it may be close to satisfactory convergence for $L_s = 28/36$ for $m = 0.01$ and $m = 0.03$. Preliminary calculations misleadingly hinted that the L_s may already be sufficiently convergered to look at the equation of state since the critical exponents found for $L_s = 28$ and $L_s = 36$ were very similar. The right panel shows the full $L_s = 36$ data set. The error bars are scaled according to appendix B.4.

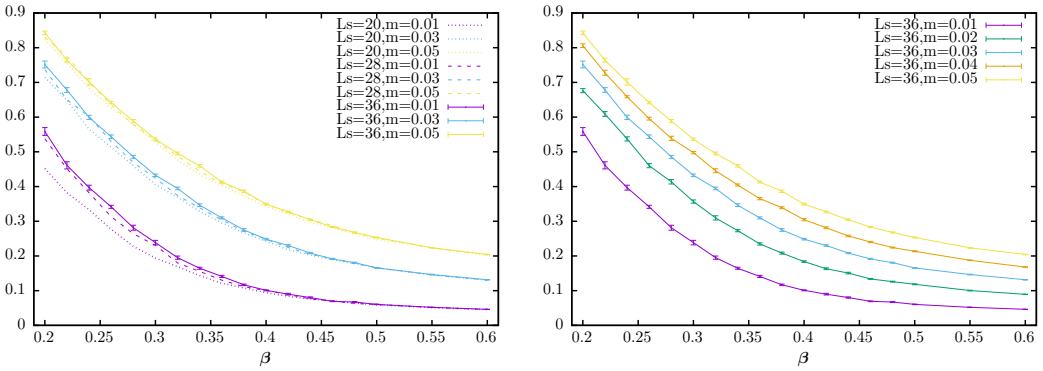

FIGURE 9.22: Dynamic Condensate with Wilson kernel. Left panel: HT formulation with various L_s and m. Right panel: HT formulation for $L_s = 36$.

The left panel of Figure 9.23 shows measurements using the Zolotarev formulation with $L_s = 24$ and a range $[0.001, 10]$, against two different mass plots of the HT formulation. While we see again that at $m = 0.05$ the condensate appears L_s converged, we see that the HT formulation is not for $m = 0.01$. We argue that similarly to the Shamir case, we do not require the L_s convegence in the generation of the auxiliary field to match that in the measurements, and hence move forwards with the HT generated auxiliary fields. We also want to see that the Zolotarev range and L_s value is sufficient. The right panel of Figure 9.23 shows the condensates measured (still using the $L_s = 36$ generated auxiliary fields) with Zolotarev range $[0.001, 20]$ for $L_s = 18$ and $L_s = 24$, expanded to $[0.0005, 20]$ for $L_s = 30$. Based on the errors of the scalar sign function approximation

we might have expected more stringent conditions to be necessary, but it appears that reasonable L_s convergence is already achieved with the $L_s = 18$ case.

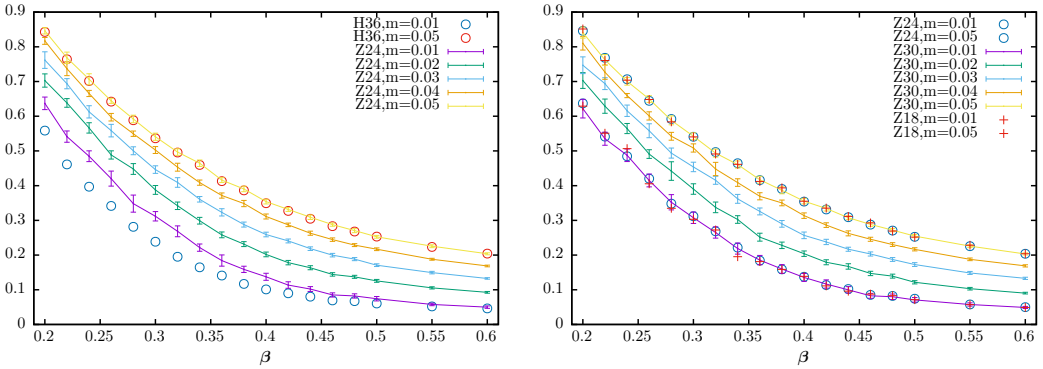

FIGURE 9.23: Dynamic Condensate with Wilson kernel. Auxiliary fields dynamically generated with HT and $L_s = 36$. Left panel: Measurements with Zolotarev ($L_s = 24$, Range=$[0.001, 20]$) and HT ($L_s = 36$) formulations at different m. Right panel: Measurements with Zolotarev ($L_s = 18/24$, Range=$[0.001, 20]$, $L_s = 30$, Range=$[0.0005, 20]$)

Partial quenching with the sea fermions calculated using higher masses has been carried out in the past [10], and our kernel eigenvalue range seems somewhat bare mass independent, so it seemed worthwhile to see whether such partial quenching could produce equivalent results, similarly to the L_s partial quenching and plots are shown in Figure 9.24. Somewhat disappointingly, although we can see that while there is some indication this may be acceptable in the weakly coupled region, it is clearly not acceptable in the strongly coupled region, with the partially quenched results rapidly diverging from their non-quenched counterparts. Of course, there is no physical justification for this sort of partial quenching, unlike the differing L_s case, where it may be viewed as different levels of accuracy in different parts of the calculation.

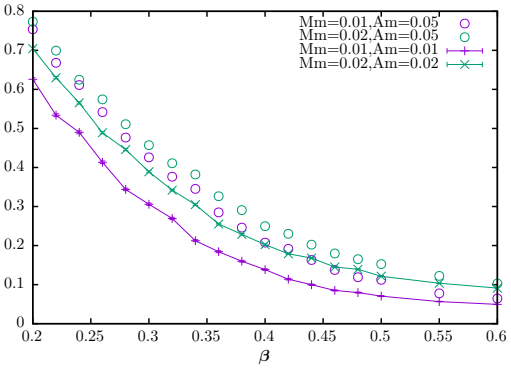

FIGURE 9.24: Auxiliary fields dynamically generated with HT and $L_s = 36$ with $m = 0.01$ designated by "Am=01". Mesurements calculated with Zolotarev $L_s = 24$ with $m = 0.01$ designated by "Mm=0.01". Partial quenching with $m = 0.05$ in the auxiliary field is considered.

9.9 Wilson EOS

We are now in the position, or at least we are closer than prior work, to be able to estimate the critical exponents via the equation of state, eqn. 5.10, generated from dynamic condensate measurements, *without the need for further non-trivial (constant) extrapolation of those condensate measurements to their L_s limit.* This constitutes the primary step forward this thesis takes from previous work in this area. Fig. 9.25 shows a number of such EOS fits. The upper panels have $\beta \in [0.2, 0.6]$, the middle panels have $\beta \in [0.22, 0.55]$, and the bottom panels have $\beta \in [0.22, 0.50]$. The auxiliary fields used are dynamically generated with $L_s = 36$ with the HT formulation. In the left hand panels, the measurements are taken with a $L_s = 24$ Zolotarev scheme, and in the right hand panels with a $L_s = 30$ Zolotarev scheme. The mass range is fixed in all cases $m \in [0.01, 0.05]$. The critical exponent values for the different cases are also tabulated in table 9.1. We see that the results between the two Zolatarev schemes are very similar, and suggest that we have found a satisfactory level of L_s convergence, although it cannot be ruled out that auxiliary fields generated with higher L_s values might provide further convergence. Although the results differ with the choice of window, the errors are quite wide and the results remain within the errors of each other. Nevertheless, it seems that the weaker coupling points, $\beta = 0.60$ especially, but also perhaps $\beta = 0.55$ are too far from the critical point to be sensibly included. The strongest coupling point $\beta = 0.20$ appears to fit the curves better, although condensate data errors are larger here. As such, despite the measure of fit being best for cases dw1/dw2 defined below, we somewhat arbitrarily choose the middle panel as representative to designate our critical exponents. Then we have

$$\begin{aligned} \beta_c &= 0.336(33) \\ \beta_m &= 1.04(29) \\ \delta &= 2.078(325) \end{aligned} \tag{9.2}$$

and correspondingly the hyperscaled values

$$\begin{aligned} \eta &= 0.95(15) \\ \nu &= 1.1(3) \end{aligned} \tag{9.3}$$

case id	L_s	β	β_c	β_m	δ	χ^2/dof
dw1	24	[0.20,0.6]	0.328(22)	1.06(19)	2.111(208)	0.189
dw2	30	[0.20,0.6]	0.326(26)	1.01(23)	2.132(267)	0.151
dw3	24	[0.22,0.55]	0.339(30)	1.07(27)	2.067(287)	0.106
dw4	30	[0.22,0.55]	0.336(33)	1.04(29)	2.078(325)	0.0899
dw5	24	[0.22,0.50]	0.355(37)	1.19(32)	1.942(294)	0.0738
dw6	30	[0.22,0.50]	0.349(40)	1.13(33)	1.979(339)	0.0694

TABLE 9.1: Equation of state critical exponents found with partially quenched (auxiliary fields generated with HT approximation with $L_s = 36$ and measurements generated using Zolotarev approximation) for different β data range windows. Mass range is $[0.01, 0.05]$.

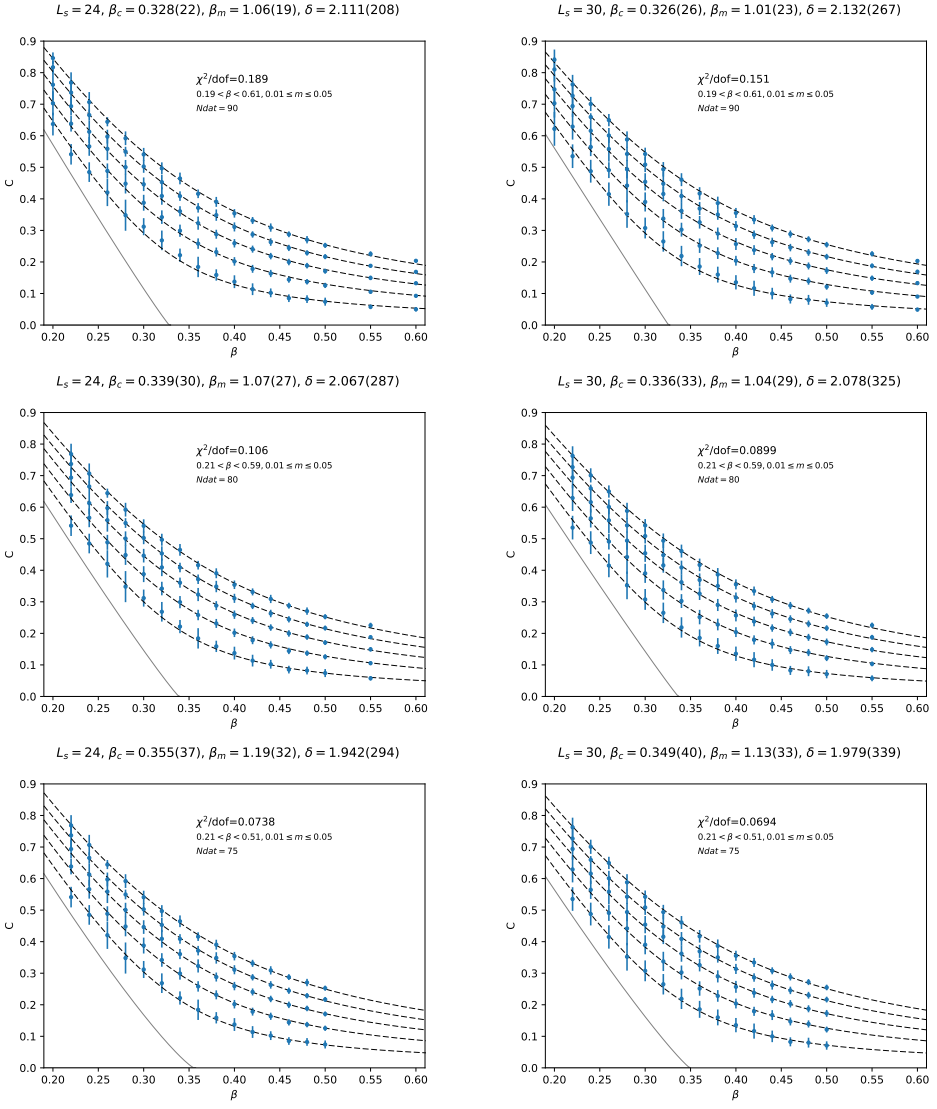

FIGURE 9.25: Equation of State fits with different condensate data windows for Wilson Zolotarev formulations. The critical coefficients at the top of each plot are tabulated in table 9.1. Left panel: uses $L_s = 24$ for measurements. Right panel: uses $L_s = 30$ for measurements.

Note we have doubled the errors of the condensate measurement in the fit. As noted for the quenched cases this only affects the χ^2 value and does not affect any of the exponent values.

9.10 Shamir EOS

Turning to the EOS for the Shamir cases, again we plot a number of β range window fits in fig. 9.26 and tabulate them in table 9.2. Again eyeballing the plots suggests that despite case ds1 having the highest χ^2/dof, a better fit is found by discarding the values at the strongest and weakest coupling. Indeed, it looks like $L_s = 300$ may still not be sufficient for the strongest couplings. So we take case ds5 to present the critical values.

case id	β	β_c	β_m	δ	χ^2/dof	N
ds1	0.24-0.60	0.299(9)	0.50(8)	3.057(350)	0.426	80
ds2	0.26-0.55	0.318(14)	0.68(15)	2.456(360)	0.324	75
ds3	0.26-0.50	0.333(19)	0.80(18)	2.171(343)	0.298	65
ds4	0.26-0.46	0.344(24)	0.88(21)	1.988(355)	0.322	55
ds5	0.28-0.50	0.339(24)	0.89(26)	2.069(399)	0.171	60
ds6	0.28-0.46	0.347(29)	0.95(30)	1.950(428)	0.186	50

TABLE 9.2: Equation of state critical exponents found with partially quenched Shamir HT kernel for different β data range windows. Mass range is $[0.01, 0.05]$.

Then we have

$$\begin{aligned} \beta_c &= 0.339(24) \\ \beta_m &= 0.89(26) \\ \delta &= 2.069(399) \end{aligned} \tag{9.4}$$

and correspondingly the hyperscaled values (eqn. 5.13)

$$\begin{aligned} \eta &= 0.96(18) \\ \nu &= 0.91(28) \end{aligned} \tag{9.5}$$

Despite the haphazard method of choosing the case, and in part thanks to the relatively large errors, the critical exponents are consistent between the Shamir and Wilson formulations. This is particularly pleasing because early results had suggested otherwise, which would have been a disappointing result. Of course, this data only hints at the similarity of the results, and more and better data is required. Results in the next chapter will suggest a further refinement of the window should be considered, ie smaller m values with a more focused β range around the critical value.

We note the significant difference with the values given in [8]. The exponents found with a Shamir kernel on $16^2 \times 16$ mesh were $\beta_c = 0.320(5)$, $\beta_m = 0.320(5)$, $\delta = 4.17(5)$, corresponding to $\nu = 0.55(1)$ and $\eta = 0.16(1)$. Further comparison with a staggered formulation may be considered which give $\beta_m = 0.57(2)$, $\delta = 2.75(9)$, corresponding to $\nu = 0.60(4)$ and $\eta = 0.71(3)$. We attribute the difference to the lack of L_s convergence in earlier work. Although extrapolation techniques were utilized, as hinted at in section 8.1, we suspect the L_s convergence curves may not be amenable to such techniques.

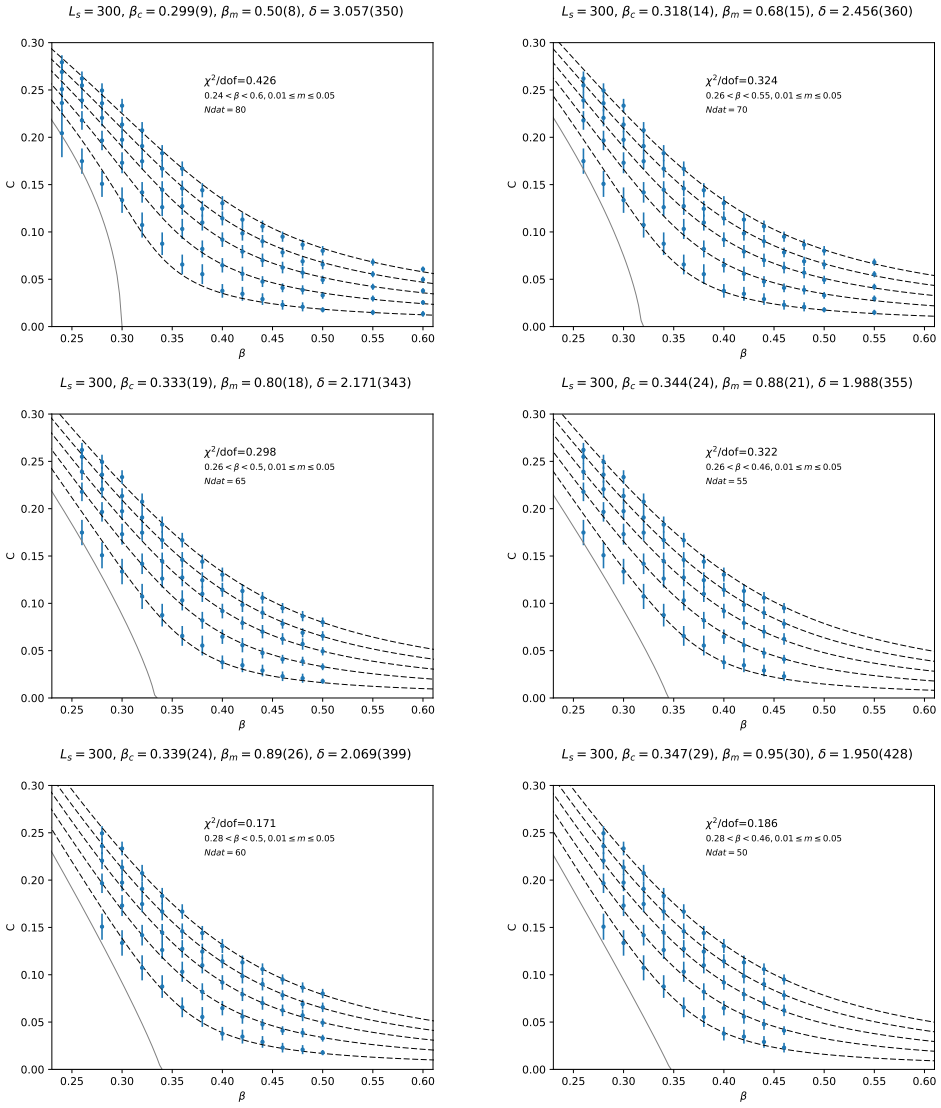

FIGURE 9.26: Equation of State fits with different condensate data windows for Shamir HT formulations. The critical coefficients at the top of each plot are tabulated in table 9.2. $L_s = 300$ for the measurements in all cases.

9.11 Summary

Using different L_s values for the sea and valence fermions we have been able to calculate an EoS and critical exponents relating to symmetry breaking condensates measured in the large L_s limit of the overlap operator, a task not achieved before in the context of the Thirring model, albeit on a relatively small $12^2 \times 12$ lattice. This was achieved through the use of an efficient partial quenching scheme, using the HT approximation in the generation of the auxiliary fields, and the Zolotarev approximation for measurements, which loses none of the physics. Although greater refinement of the calculation should be carried out in the future, the compatible results stemming from the Wilson and

Shamir formulations give confidence in the process. Counts of the computational costs suggest that the Wilson formulation is preferable, although without an equivalent scaling window comparisons are not entirely fair.

Chapter 10

Further Measurements

Finally, we explore two measurements which have proven challenging in the past, namely the axial ward identity, which relates meson correlators to the condensate via eqn. 10.1. The ratio of the left and right terms should be equal to one both in the lattice formulation and hence also in the continuum limit, which was not found to be the case [46, 65]. Suggestions for the cause of this discrepancy included a lack of U(2) symmetry on the lattice, ie insufficient L_s. The relation was also found to be independent of the bare mass leading to the suggestion that the bare mass is not correct to plug into eqn. 10.1 but that a physical mass should be used. Also the suggestion that the field identification, eqn. 3.41, be altered through renormalisation in some way was put forward, although this is ruled out when using the domain wall formulation in strict adherence to the overlap operator.

The chiral susceptibility defined as the derivative of the condensate wrt m, eqn. 10.3, and equivalently calculated as the variance of Σ, eqn. 10.4, has also previously been calculated [7]. In that work the correct qualitative behaviour as a function of β was successfully demonstrated for each mass value, but when evaluated with eqn. 10.4 the magnitudes increased with increasing m, contrary to the value derived from eqn. 10.3 via the equation of state.

We return to these measurements in the less challenging environment of $12^2 \times 12$ meshes where we are able to push closer to the large L_s limit, using the auxiliary fields and partially quenched condensate results generated for the results of the previous chapter.

10.1 Axial Ward Identity

Continuous symmetries of the theory are identified with conserved currents, and consideration of infinitessimal transforms of the standard measurements, eqn. 2.1, leads to the Ward identities [10]. We want to calculate the axial Ward identity, associated

with the $U(2)$ symmetry of the Thirring model, given by eqn. 10.1 [46], where C is the condensate.

$$\frac{C}{m} = \sum_x \langle \bar{\psi}(0)\gamma_5\psi(0)\bar{\psi}(x)\gamma_5\psi(x)\rangle \tag{10.1}$$

We already have the data for the condensate of the left hand component and need to evaluate the series of of meson-like propagators on the rhs, to which end we use eqn. A.11, and via $M^{-1}_{yx} = \gamma_5(M^{-1}_{xy})^\dagger\gamma_5$ we have

$$\frac{C}{m} = \sum_x \langle \mathrm{Tr}[(M^{-1}_{x0})^\dagger M^{-1}_{x0}]\rangle \tag{10.2}$$

This is readily calculable. Although the correlator is defined from 0 to x in eqn. 10.1 we may choose any starting value y instead since it has translational invariance. Indeed, statistics may be improved using more than one location for each auxilary field, although all the results presented below just use $y = 0$. Having chosen y, we then use four point estimators, one for each Dirac index, to calculate aM^{-1}_{x0} for all x, where $M = D_{OL}$. We note that using the overlap formulation directly eliminates the need to patch together the meson correlator from distinct components on each wall as is the case for the domain wall formulation.

We provide plots for both the ratio, $\frac{C}{mR}$ where R is the rhs of eqn. 10.1. In fig. 10.1 we consider the dynamic Wilson case. To match the condensate measurement, we similarly use the auxiliary fields generated with HT $L_s = 36$, and measure with Zolotarev $L_s = 30$ in the generation of the rhs term. An increase with increasing β is found, with the identity getting close to 1 at the stronger end of the range, although at weaker coupling the ratio falls off significantly. In figs. 10.2 and 10.3 we show results from the Shamir cases. The curves also ascend through the critical point with a value of around 0.5. L_s improvement does not seem to make a significant difference.

Overall, the ratios we have achieved are closer to one than previous results although something is clearly still amiss. Perhaps the neglected (disconnected) term in the evaluation of eqn. 10.1 is more significant than assumed. Despite the limited statistics it looks like the underlying issues will not be resolved simply by better data and a more fundamental remedy will be required.

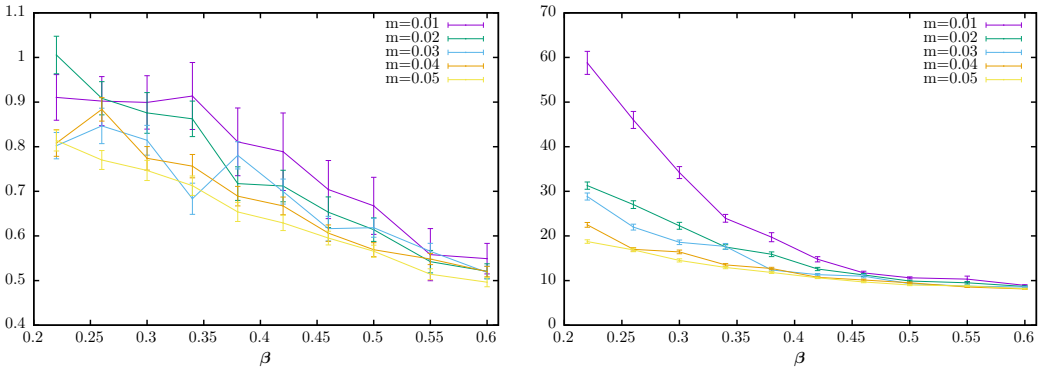

FIGURE 10.1: Axial Ward identity for dynamic Wilson formulation. Left panel: Ratio $\frac{C}{mR}$. Right panel: RHS term (eqn.10.1).

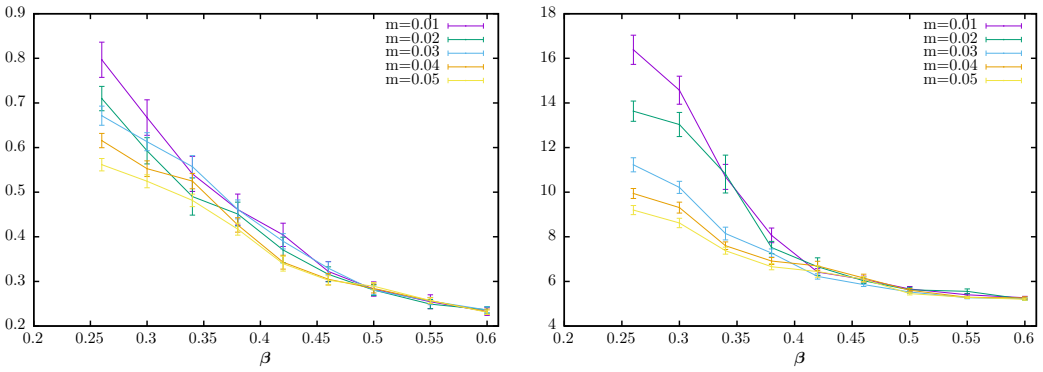

FIGURE 10.2: Axial Ward identity for dynamic Shamir formulation ($L_s = 96$ for measurement). Left panel: Ratio $\frac{C}{mR}$. Right panel: RHS term (eqn.10.1).

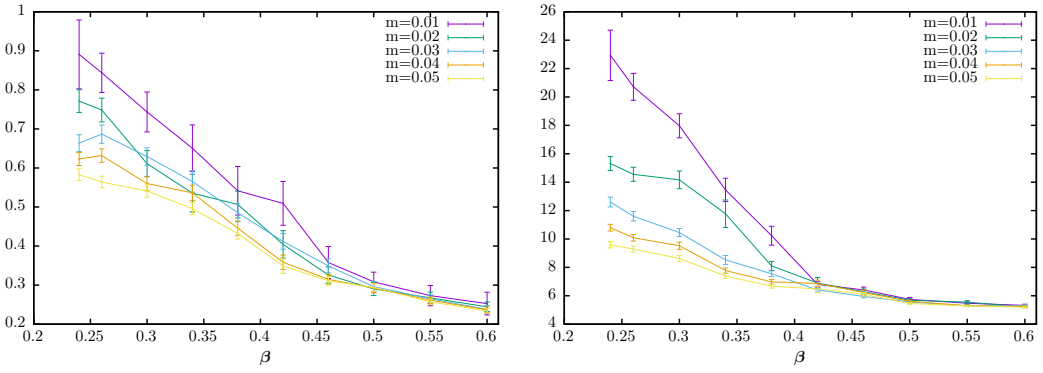

FIGURE 10.3: Axial Ward identity for dynamic Shamir formulation ($L_s = 300$ for measurement). Left panel: Ratio $\frac{C}{mR}$. Right panel: RHS term (eqn.10.1).

10.2 Chiral Susceptibility

We move on to the *chiral susceptibility* χ, defined by eqn. 10.3 [7], and detailed in appendix A.5

$$\chi \equiv \frac{\partial^2 \ln Z}{\partial m^2} = \frac{\partial C}{\partial m} \tag{10.3}$$

We may calculate this directly either as the numerical derivative of the condensate data or as the derivative of our equation of state. Alternatively, denoting the condensate instances Σ via the the condensate, $C = \langle \Sigma \rangle = \langle \bar{\psi} D^m \psi \rangle$, we may also evaluate the susceptibility as the variance of those instances Σ, eqn. 10.4[1]. Evaluation by either method should match.

$$\chi = \langle \Sigma^2 \rangle - \langle \Sigma \rangle^2 \tag{10.4}$$

Figs. 10.4 and 10.5 show the susceptibility calculated from the derivatives of equation of states chosen from those presented in the previous two chapters. All are qualitatively similar, with the peak magnitude increasingly increasing as $m \to 0$ around the critical point. Since this limit, $\chi_{m \to 0, \beta = \beta_c} = \infty$, this is what we want to see. The peaks for the Wilson cases are somewhat more than double those of the corresponding Shamir cases. This suggests the feasibility of the simple rescaling described in section 5.2.

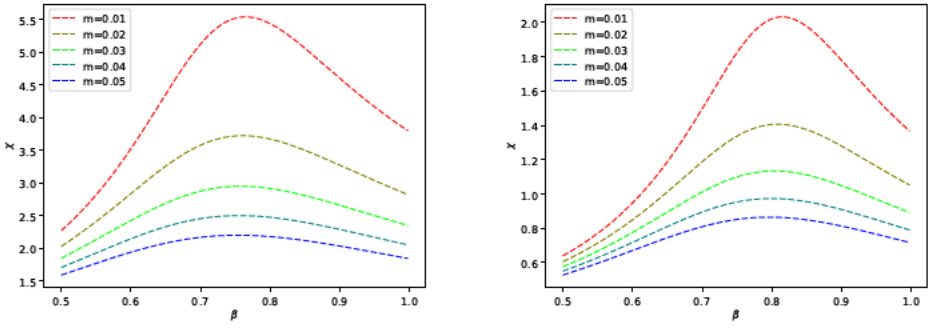

FIGURE 10.4: Quenched susceptibilities from EOS. Left panel: Wilson ZLs24, $\beta \in (0.5, 1.0)$. Right panel: Shamir Ls300, $\beta \in (0.52, 1.2)$.

[1] This calculation omits the connected components as set out in appendix A.5

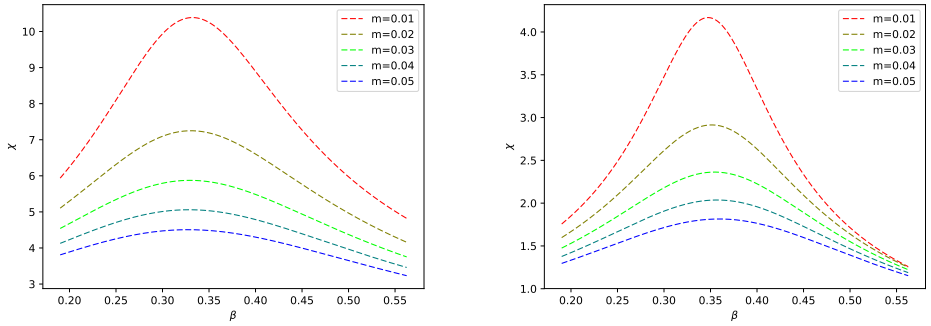

FIGURE 10.5: Dynamic susceptibilities from EOS. Left panel: Wilson ZLs30 (AH36). Right panel: Shamir Ls300 (AH96).

However, calculations based on eqn. 10.4 are less neat. Of course, variance calculations are more computationally demanding that mean value calculations, and the data is rather noisy again. Plots for the quenched Wilson and quenched Shamir cases are shown in figs.10.6 and 10.7 respectively. The data used in the evaluation is noisy, and of course, one should mitigate against the use of noisy estimators in the evaluation of Σ, but this data was not preserved, and the following is based on a naive evaluation only. The left panel Wilson plot uses Zolotarev with $L_s = 24$, and the right panel uses HT with $L_s = 36$. The left panel Shamir plot uses HT with $L_s = 300$, and the right panel uses HT with $L_s = 96$. While in all cases we find the correct increase in magnitude with decreasing m in the strongly coupled region, for the Wilson case with $HL_s = 36$ the $m = 0.01$ curve gives the smallest magnitude in the weakly coupled region. Overall it seems that limiting the L_s dampens the condensate instances, which makes sense since this has the effect of reducing the magnitude of eigenvalues in the sign function of the overlap operator to less than one beyond the range of the approximation. Further, the susceptibilities increase with decreasing β, and do not show the downturn beyond the critical point, although there are hints of this when the better L_s approximations are used. We believe this is a consequence of ignoring the noisiness of the data.

The calculations using the dynamic data, shown in figs. 10.8, 10.9, 10.10 paint a similar picture, but perhaps more strongly suggest that the inversion of the magnitude with decreasing m is simply a consequence of sufficient L_s. We suggest that away from the critical point, lattice artifacts may be stronger and are a potential reason for stronger discrepancies for β-values further from the critical point.

Overall, however, these results suggest that better L_s resolution and better statistical data is likely to be sufficient to have matching calculations of the susceptibility as we require.

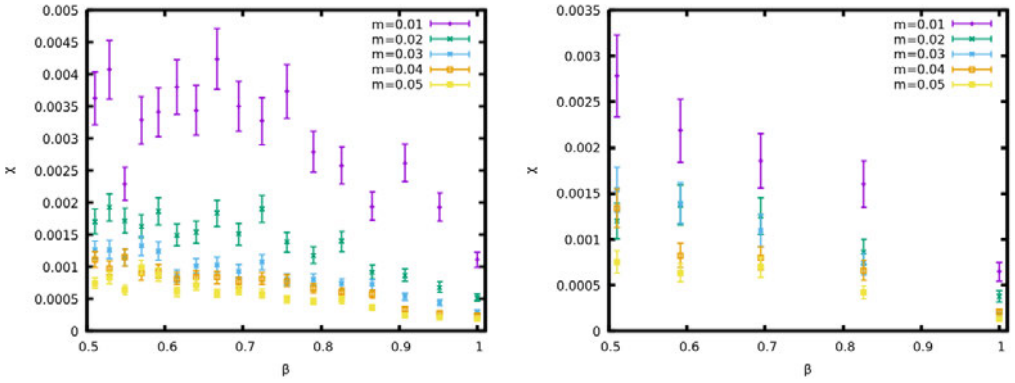

FIGURE 10.6: Quenched Wilson susceptibilities calculated with eqn. 10.4. Left panel: Z $L_s = 24$ formulation. Right panel: HT $L_s = 36$ formulation.

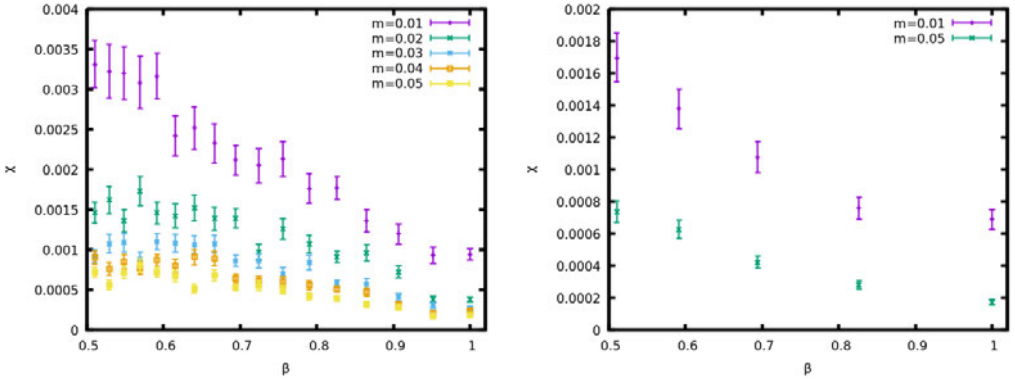

FIGURE 10.7: Quenched Shamir susceptibilities calculated with eqn. 10.4. Left panel: HT $L_s = 300$ formulation. Right panel: HT $L_s = 96$ formulation.

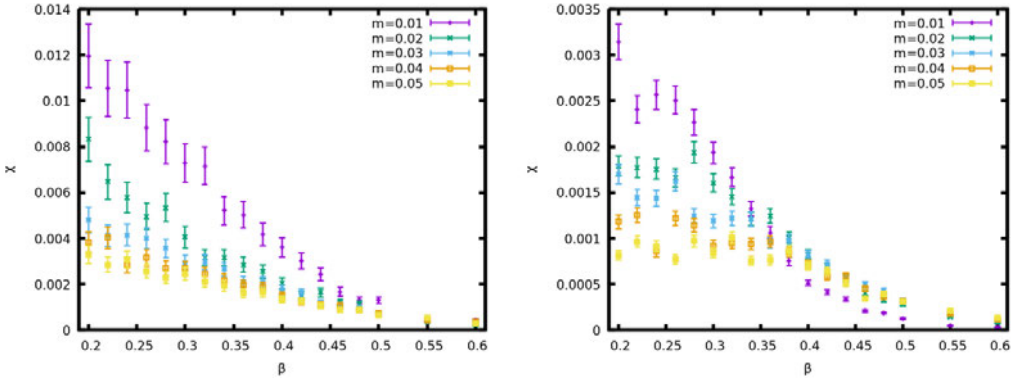

FIGURE 10.8: Dynamic Wilson susceptibilities calculated with eqn. 10.4. Left panel: Partially quenched Z $L_s = 24$ formulation. Right panel: HT $L_s = 36$ formulation.

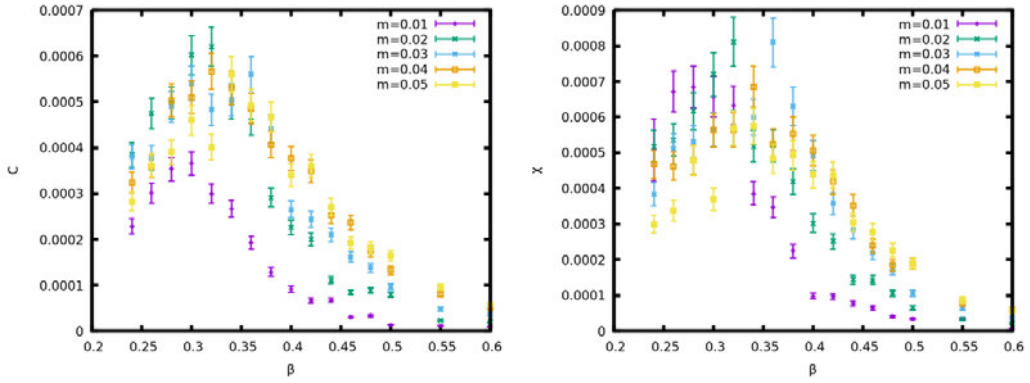

FIGURE 10.9: Dynamic Shamir susceptibilities calculated with eqn. 10.4. Left panel: HT $L_s = 60$. Right panel: HT $L_s = 96$ formulation.

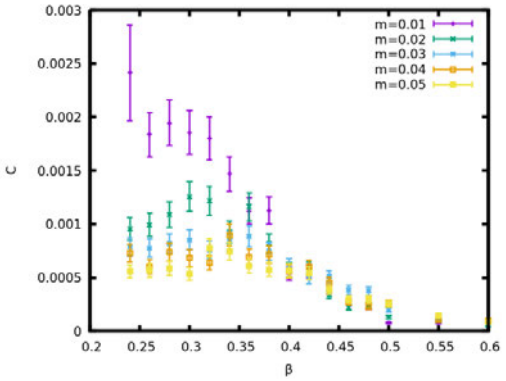

FIGURE 10.10: Dynamic Shamir susceptibilities calculated with eqn. 10.4. Partially quenched HT $L_s = 300$.

Chapter 11

Conclusion

11.1 Summary

This work has investigated different formulations of lattice Dirac operators which obey the GW relations and recover the U(2) symmetry in the continuum limit; namely the overlap operator and the equivalent domain wall operator. These have been explored in the context of the 2+1d Thirring model.

Code development has primarily been a standalone Fortran code implementing a range of Dirac operators and measurements thereof utilising either quenched or imported auxiliary fields. Dynamically generated auxiliary fields were produced with the freely available Fortran code [64]. This is a Shamir kernel domain wall code, and it was altered to provide the option of generating fields with the Wilson kernel.

As a modest contribution on the theoretical side, the twisted mass formulation of the overlap condensate, eqn.4.15 was introduced in this work, corresponding to the twisted mass formulation of the domain wall condensate introduced in [3].

The locality of the overlap operator was numerically demonstrated for the strongly coupled 2+1d Thirring model. It had only been demonstrated for a weakly coupled region with a bounded auxiliary field before. That the Zolotarev formulation improves L_s convergence is not new, it being optimal, but this work contributes to the body of knowledge on convergence rates and the GW error.

A number of different aspects of the Dirac operators and their implementations were investigated. Eigenvalue ranges of the overlap kernel were explored, and a key finding is that the non-compact link fields leads to apparently unbounded from above eigenvalue ranges in the overlap kernel, whereas these are clearly bounded with compact link fields. This has very significant (detrimental) implications on the computational difficulty of inverting the Dirac operator. Further, the Shamir formulation appears to become more

challenging as the mesh gets larger in a way that the Wilson kernel doesn't. That is, that the kernel eigenvalue range increases with mesh size around and beyond the critical coupling strength.

Varying the domain wall height was briefly explored in the quenched cases, and was found to signifcantly improve kernel eigenvalue ranges for fixed β, and the improvement is most pronounced around β_c. This benefit may be reduced somewhat since we subsequently show that β_c moves with M, but there is clearly benefit to be exploited here. Further, we suggest that reducing the domain wall height appears to zoom in on the mass scaling in the Shamir formulated EoS.

Using the relatively small mesh size of 12x12 we were able to achieve reasonably well L_s converged quenched results with the Zolotarev approximation for the Wilson formulation with a low $L_s = 24$ and the utilisation of $L_s = 300$ was achievable for the Shamir formulation using the indirect domain wall formulation (eqn.3.91). Shamir cases were run with both $M = 1.0$ and $M = 0.5$. It is clear that M has a significant impact on the results, and one hopes corresponds to a rescaling of the equation of state variables.

In the dynamic generation of auxililary fields, it was found that the Wilson formulation had a lower acceptence rate in the hamiltonian dynamics steps, becoming more pronounced at the stronger coupling. Fitting with the perspective that the Shamir results are rescaled from the Wilson results, we speculate that we might expect to find the same acceptance rates with suitably rescaled Shamir mass and β values.

Another key finding, or observation, was that the level of accuracy corresponding to the large L_s limit required in the measurement of the condensate, is not required in the generation of the auxiliary fields. Given that the bulk of computational effort in dynamic simulations is in the generation of the auxiliary fields this has the potential to save significant computational cost.

Condensates with compact link fields were also considered, largely due to the celerity of their calculation, and were found not to have a phase change at least not with the mass as the order parameter. The significance of this is unclear and unexplored, but was a surprising result.

We calculated an equation of state and critical exponents for both Wilson and Shamir kernels, using low accuracy for the generation of the auxiliary fields and high accuracy for the measurements. Although better statistics would be desirable, the results are consistent between the formulations, as we would hope. This was particularly good news as lower L_s-range preliminary work had hinted that consistency may not have been found. This would not have been possible without the partial quenching.

Finally we looked at the axial ward identity and chiral susceptibility, calculations which have been found challenging in the past. It appears that difficulties in the calculation of the chiral susceptibility can simply be attributed to insufficient L_s resolution. While

it seems some improvements are made here in the calculation of the axial ward identity, it does not suggest that the better L_s combined with better statistics will be enough to resolve the discrepancies found in the data.

A couple of comments are to be made before concluding with the outlook for future work. At the outset one of the simple question was which kernel to use. It seems to the author that both should be used, providing a valuable crosscheck. Although we were able to get away with using the HT scheme with the Shamir formulation in this work, this will be limited in general since the requirements seem to become more stringent with increasing lattice size. We see via the denominator coefficients of the partial fraction representation that the HT approximation needs to achieve a similar smallest coefficient to the Zolotarev approximation to match its accuracy, but has very many wasteful partial fraction terms. And hence Zolotarev should almost always be used *from that perspective*, notwithstanding the scaled HT formulation may be preferable for relatively small eigenvalue ranges.

The phrase partially quenched has been used to describe differing L_s values between the sea fermions (those used to dynamically generate the auxiliary fields) and the valence fermions. This is somewhat misleading, as it may more simply be viewed as relative accuracy between two different parts of the overall calculation, and there is no quenching, partial or otherwise, of any of the physics, when suitable L_s values are found.

11.2 Outlook

Inevitably, there is much more to do, too many stones were left unturned, and better statistics would be beneficial in almost all of the simulations. Nevertheless we may set out the following goals following on the work carried out in this thesis, continuing to work with a 12^2x12 mesh for the moment.

- Generate more dynamic Wilson fields with $M = 1$ and include $m = 0.005$, $m = 0.075$ data. Double the number of β data points to improve EoS χ^2 value, continuing with the same range. We want to see a very clearly window independent EoS.
- Repeat the process with $M = 0.5$.
- Generate Shamir auxiliary fields with a narrower window (smaller m, β closer to β_c). Explore whether this is better achieved with $M \neq 1.0$.
- Establish scaling relations between the different Dirac operator configurations. This would provide a significant boost to the confidence in the validity of the EoS.

There are further issues which we would like to explore.

Designer sign approximations Can we find non-optimal approximations which include higher order polynomial terms which allow a larger smallest denominator coefficient for the rational part. Explicitly, can we extend eqn. 3.77 to the form $\mathrm{sgn}(r) = \sum_j c_j r^j + dr(b_0 + \sum_{m=1}^{N_d} \frac{b_m}{r^2+d_m})$ and choose c_j so that the smallest values d_m are increased, leading to faster evaluation overall.

GW correction term It would be affirmative to look at eqn. 7.9 for dynamic formulations. We expect it to vanish as we go to critical coupling.

Appendix A

Formulational Issues

A.1 Matthews-Salam Relations

To ensure the correct Fermi statistics the spinors ψ,$\bar{\psi}$ must be made up of Grassmann numbers. We make use of the Matthews-Salam formula to integrate these which is given by [10]

$$\int \mathcal{D}[\eta,\bar{\eta}]e^{\bar{\eta}M\eta} = \det[M] \tag{A.1}$$

where $\mathcal{D}[\eta,\bar{\eta}] = d\eta_N d\bar{\eta}_N \cdots d\eta_1 d\bar{\eta}_1$, we have the vectors of Grassmann variables $\eta = \{\eta_1,\cdots,\eta_N\}$, , $\bar{\eta} = \{\bar{\eta}_1,\cdots,\bar{\eta}_N\}$, and the complex valued $N \times N$ matrix M. We then have Wick's theorem, for n twin Grassmann numbers,

$$\int \mathcal{D}[\eta,\bar{\eta}]\ \eta_{i_1}\bar{\eta}_{j_1}\cdots\eta_{i_n},\bar{\eta}_{j_n}e^{\bar{\eta}M\eta} = f(i_1,j_1,\cdots,i_n,j_n,M)\det[M] \tag{A.2}$$

where

$$f(i_1,j_1,\cdots,i_n,j_n,M) = (-1)^n \sum_{P(1,\cdots,n)} \text{sign}(P)(M^{-1})_{i_1 j_{P_1}}(M^{-1})_{i_2 j_{P_2}}\cdots(M^{-1})_{i_n j_{P_n}} \tag{A.3}$$

where we sum over all the permutations of the set $P = \{1,\cdots,n\}$, and sign(P) is $+1$ if the number of element swaps to reach the identity permutation is even, and -1 if odd. Hence we have the Matthews-Salam relations

$$f(i_1,j_1,M) = -(M^{-1})_{i_1 j_1} \tag{A.4}$$

$$f(i_1,j_1,i_2,j_2,M) = (M^{-1})_{i_1 j_1}(M^{-1})_{i_2 j_2} - (M^{-1})_{i_1 j_2}(M^{-1})_{i_2 j_1} \tag{A.5}$$

If terms of our Dirac operator, each spinor has 4 components, although for notational brevity we consider below a 2 component spinor,

$$\psi(i) = \begin{pmatrix} \eta_{i,1} \\ \eta_{i,2} \end{pmatrix} \quad \bar{\psi}(j) = \begin{pmatrix} \bar{\eta}_{j,1} & \bar{\eta}_{j,2} \end{pmatrix} \tag{A.6}$$

so the propagator $\langle \psi(i)\bar{\psi}(j) \rangle$ is

$$\begin{aligned} \langle \psi(i)\bar{\psi}(j) \rangle &= \begin{pmatrix} \langle \eta_{i,1}\bar{\eta}_{j,1} \rangle & \langle \eta_{i,1}\bar{\eta}_{j,2} \rangle \\ \langle \eta_{i,2}\bar{\eta}_{j,1} \rangle & \langle \eta_{i,2}\bar{\eta}_{j,2} \rangle \end{pmatrix} = \begin{pmatrix} \langle \eta_k\bar{\eta}_l \rangle & \langle \eta_k\bar{\eta}_{l+1} \rangle \\ \langle \eta_{k+1}\bar{\eta}_l \rangle & \langle \eta_{k+1}\bar{\eta}_{l+1} \rangle \end{pmatrix} \\ &= \begin{pmatrix} -(M^{-1})_{k,l} & -(M^{-1})_{k,l+1} \\ -(M^{-1})_{k+1,l} & -(M^{-1})_{k+1,l+1} \end{pmatrix} = -(M^{-1})_{i,j} \end{aligned} \tag{A.7}$$

and further

$$\langle \Gamma\psi(i)\bar{\psi}(j) \rangle = \Gamma \langle \psi(i)\bar{\psi}(j) \rangle = -\Gamma(M^{-1})_{i,j} \tag{A.8}$$

Conversely we have

$$\begin{aligned} \langle \bar{\psi}(j)\psi(i) \rangle &= \langle \bar{\eta}_{j,1}\eta_{i,1} \rangle + \langle \bar{\eta}_{j,2}\eta_{i,2} \rangle \\ &= \langle \mathrm{Tr}[(M^{-1})_{ij}] \rangle \end{aligned} \tag{A.9}$$

and

$$\langle \bar{\psi}(j)\Gamma\psi(i) \rangle = \langle \mathrm{Tr}[\Gamma(M^{-1})_{ij}] \rangle \tag{A.10}$$

For second order terms, corresponding to eqn. A.5, we have a meson like propagator.

$$\begin{aligned} \langle \bar{\psi}(i)\Gamma\psi(i)\bar{\psi}(j)\Gamma\psi(j) \rangle = &- \langle \mathrm{Tr}[\Gamma(M^{-1})_{i,j}\Gamma(M^{-1})_{j,i}] \rangle \\ &+ \langle \mathrm{Tr}[\Gamma(M^{-1})_{i,i}]\mathrm{Tr}[\Gamma(M^{-1})_{j,j}] \rangle \end{aligned} \tag{A.11}$$

The second term, the disconnected term, is often neglected [10]. The eqns. A.9, A.10, A.11 are the Matthews-Salam relations.

A.2 Parity Invariance

The parity of a system describes its "evenness" or "oddness". A parity invariant system has its lagrangian remain constant under a parity transformation, defined below.[1] We confirm parity of the three different mass terms, transcribing from [44]. For an active

[1] We invert an odd number of axes. Inverting an even number corresponds to a rotation of the coordinates.[3]

frame of reference transform we have

$$\begin{aligned} x &\to \Lambda x \\ \psi(x) &\to P[\Lambda]\psi(\Lambda^{-1}x) \\ \bar{\psi}(x) &\to \bar{\psi}(\Lambda^{-1}x)P[\Lambda]^{-1} \\ \partial_\mu\psi(x) &\to \Lambda^{-1}P[\Lambda]\partial_\mu\psi(\Lambda^{-1}x) \\ A(x) &\to \Lambda A(\Lambda^{-1}x) \end{aligned} \tag{A.12}$$

where Λ is the space-time transform, and the form $P[\Lambda]$ is to be determined. We choose our parity transform to reflect all 3 space-time dimensions, so the coordinate transform matrix is $\Lambda = -I_3$. We find two suitable forms, $P_1[\Lambda] = \gamma_3$ and $P_2[\Lambda] = \gamma_5$. This is distinct from 3+1d where $P[\Lambda] = \gamma_0$. Noting

$$\begin{aligned} \mathcal{P}[S^1] &= \mathcal{P}[\bar{\psi}(D+m)\psi] \\ &= \mathcal{P}[\bar{\psi}\gamma_\mu\partial_\mu\psi] + \mathcal{P}[\bar{\psi}\gamma_\mu iA_\mu\psi] + \mathcal{P}[\bar{\psi}m\psi] \end{aligned} \tag{A.13}$$

we can then show parity invariance of the individual terms

$$\begin{aligned} \mathcal{P}_1[\bar{\psi}\gamma_\mu\partial_\mu\psi] &= \bar{\psi}P_1[\Lambda]^{-1}\gamma_\mu\Lambda^{-1}P_1[\Lambda]\partial_\mu\psi \\ &= \bar{\psi}\gamma_3\gamma_\mu(-1)\gamma_3\partial_\mu\psi \\ &= \bar{\psi}\gamma_\mu\partial_\mu\psi \end{aligned} \tag{A.14}$$

$$\begin{aligned} \mathcal{P}_1[\bar{\psi}\gamma_\mu iA_\mu\psi] &= \bar{\psi}P_1[\Lambda]^{-1}\gamma_\mu i\Lambda A_\mu P_1[\Lambda]\psi \\ &= \bar{\psi}\gamma_3\gamma_\mu(-i)A_\mu\gamma_3\psi \\ &= \bar{\psi}\gamma_\mu iA_\mu\psi \end{aligned} \tag{A.15}$$

$$\begin{aligned} \mathcal{P}_1[\bar{\psi}m\psi] &= \bar{\psi}P_1[\Lambda]^{-1}mP_1[\Lambda]\psi \\ &= \bar{\psi}m\psi \end{aligned} \tag{A.16}$$

$\mathcal{P}_2$ follows an identical process since γ_5 also anticommutes with $\gamma_0, \gamma_1, \gamma_2$ similarly to γ_3. For S^3 we need only consider the mass terms, which are only invariant under one of the two parity transforms.

$$\mathcal{P}[S^3] = \mathcal{P}[\bar{\psi}(D - i\gamma_3 m)\psi)] \tag{A.17}$$

$$\begin{aligned} \mathcal{P}_1[\bar{\psi}(-i\gamma_3 m)\psi] &= \bar{\psi}P_1[\Lambda]^{-1}(-i\gamma_3 m)P_1[\Lambda]\psi \\ &= \bar{\psi}\gamma_3(-i\gamma_3 m)\gamma_3\psi \\ &= \bar{\psi}(-i\gamma_3 m)\psi \end{aligned} \tag{A.18}$$

which is invariant, but

$$\begin{aligned} \mathcal{P}_2[\bar{\psi}(-i\gamma_3 m)\psi] &= \bar{\psi}P_2[\Lambda]^{-1}(-i\gamma_3 m)P_2[\Lambda]\psi \\ &= \bar{\psi}\gamma_5(-i\gamma_3 m)\gamma_5\psi \\ &= \bar{\psi}(i\gamma_3 m)\psi \end{aligned} \tag{A.19}$$

is not, since the sign of mass term has been flipped. This situation is reversed for S^5.

To see that the irreducible formulation is not parity invariant, note that parity demonstrated above was contingent on the anti-commutivity of the γ_3 and γ_5 matrices with the γ_0,γ_1,γ_2 matrices. For the irreducible formulation we would need to find an anti-commuting matrix equivalent to γ_3 or γ_5 for the Pauli matrices. The Pauli matrices possess $\sigma_1^2 = \sigma_2^2 = \sigma_3^2 = -i\sigma_1\sigma_2\sigma_3 = I$. If we require some M that anti-commutes with all $\sigma_i M = -M\sigma_i$ then $-i\sigma_1\sigma_2\sigma_3 M = iM\sigma_1\sigma_2\sigma_3$, i.e. $M = -M$, which only holds if $M = 0$.

A.3 Equivalence of Domain Wall and Overlap Operators

We demonstrate the equivalence of the determinant of the domain wall operator and the overlap operator. We choose the Wilson kernel and the twisted mass term for the illustration. The overall approach is taken from [39], and the twisted mass form derivation was initially provided in [35] for the Shamir kernel.

A.3.1 Some Linear Algebra

Consider [39] the LDU decomposition of a matrix $M = L\Lambda U$ with the following structure, where the T_i and $C_\pm$ are square matrices,

$$M = \begin{pmatrix} 1 & 0 & 0 & -T_1^{-1}C_+ \\ -T_2^{-1} & 1 & 0 & 0 \\ 0 & -T_3^{-1} & 1 & 0 \\ 0 & 0 & -T_4^{-1} & C_- \end{pmatrix} \tag{A.20}$$

then with $T = T_1T_2T_3T_4$,

$$L\Lambda U = \begin{pmatrix} 1 & 0 & 0 & 0 \\ -T_2^{-1} & 1 & 0 & 0 \\ 0 & -T_3^{-1} & 1 & 0 \\ 0 & 0 & -T_4^{-1} & 1 \end{pmatrix} \begin{pmatrix} 1 & 0 & 0 & 0 \\ 0 & 1 & 0 & 0 \\ 0 & 0 & 1 & 0 \\ 0 & 0 & 0 & C_- - T^{-1}C_+ \end{pmatrix} \begin{pmatrix} 1 & 0 & 0 & -T_1^{-1}C_+ \\ 0 & 1 & 0 & -T_2^{-1}T_1^{-1}C_+ \\ 0 & 0 & 1 & -T_3^{-1}T_2^{-1}T_1^{-1}C_+ \\ 0 & 0 & 0 & 1 \end{pmatrix} \tag{A.21}$$

with the Schur complement $S = C_- - T^{-1}C_+$ and

$$L^{-1} = \begin{pmatrix} 1 & 0 & 0 & 0 \\ -T_2^{-1} & 1 & 0 & 0 \\ (-T_2)^{-1}(-T_3)^{-1} & -T_3^{-1} & 1 & 0 \\ (-T_2)^{-1}(-T_3)^{-1}(-T_4)^{-1} & (-T_3)^{-1}(-T_4)^{-1} & -T_4^{-1} & 1 \end{pmatrix} \tag{A.22}$$

$$\Lambda^{-1} = \begin{pmatrix} 1 & 0 & 0 & 0 \\ 0 & 1 & 0 & 0 \\ 0 & 0 & 1 & 0 \\ 0 & 0 & 0 & S^{-1} \end{pmatrix} \tag{A.23}$$

$$U^{-1} = \begin{pmatrix} 1 & 0 & 0 & -T_1^{-1}C_+ \\ 0 & 1 & 0 & -T_2^{-1}T_1^{-1}C_+ \\ 0 & 0 & 1 & -T_3^{-1}T_2^{-1}T_1^{-1}C_+ \\ 0 & 0 & 0 & 1 \end{pmatrix} \tag{A.24}$$

so $M^{-1} = U^{-1}\Lambda^{-1}L^{-1}$ and

$$(M^{-1})_{44} = S^{-1} = (C_- - T^{-1}C_+)^{-1} \tag{A.25}$$

is the inverse of the Schur complement S. The example 4×4 M matrix given can be extended to a $N \times N$ with the same structure. For any Dirac operator that we can put into this form with suitable T, we can connect to an approximation of the sign function and hence the overlap operator. The salient feature of the LDU decomposition is that the determinants of the lower and upper diagonal matrices are 1, so that

$$\det[M] = \det[\Lambda] = \det[S] \tag{A.26}$$

A.3.2 Wilson Domain Wall M3

Choosing not to simplify[2] with $P_-\gamma_3 = -P_-$, $P_+\gamma_3 = P_+$, we have

$$D_{DW}^{M3} = \begin{pmatrix} \omega_1 D^{\|} + I & (\omega_1 D^{\|} - I)P_+ & 0 & -(\omega_1 D^{\|} - I)im\gamma_3 P_- \\ (\omega_2 D^{\|} - I)P_- & \omega_2 D^{\|} + I & (\omega_2 D^{\|} - I)P_+ & 0 \\ 0 & (\omega_3 D^{\|} - I)P_- & \omega_3 D^{\|} + I & (\omega_3 D^{\|} - I)P_+ \\ -(\omega_4 D^{\|} - I)im\gamma_3 P_+ & 0 & (\omega_4 D^{\|} - I)P_- & \omega_4 D^{\|} + I \end{pmatrix} \tag{A.27}$$

Using the compacting matrix

$$C = \begin{pmatrix} P_- & 0 & 0 & P_+ \\ P_+ & P_- & 0 & 0 \\ 0 & P_+ & P_- & 0 \\ 0 & 0 & P_+ & P_- \end{pmatrix} \tag{A.28}$$

[2] for future algbraic consistency and simplicity

$$D_{DW}^{M3}C = \begin{pmatrix} (\omega_1 D^{\parallel} + I)P_- + (\omega_1 D^{\parallel} - I)P_+ & 0 & 0 & (\omega_1 D^{\parallel} + I)P_+ - (\omega_1 D^{\parallel} - I)im\gamma_3 P_- \\ (\omega_2 D^{\parallel} - I)P_- + (\omega_2 D^{\parallel} + I)P_+ & \cdots & 0 & 0 \\ 0 & \cdots & \cdots & 0 \\ 0 & 0 & \cdots & -(\omega_4 D^{\parallel} - I)im\gamma_3 P_+ + (\omega_4 D^{\parallel} + I)P_- \end{pmatrix} \tag{A.29}$$

Let

$$\begin{aligned} Q_i^+ &= (\omega_i D^{\parallel} + I)P_- + (\omega_i D^{\parallel} - I)P_+ \\ Q_i^- &= (\omega_i D^{\parallel} + I)P_+ + (\omega_i D^{\parallel} - I)P_- \end{aligned} \tag{A.30}$$

$$\begin{aligned} C_+ &= P_+ - im\gamma_3 P- \\ C_- &= P_- - im\gamma_3 P+ \end{aligned} \tag{A.31}$$

so that

$$D_{OL}^{M3}C = \begin{pmatrix} Q_1^+ & 0 & 0 & Q_1^- C_+ \\ Q_2^- & Q_1^+ & 0 & 0 \\ 0 & Q_3^- & Q_3^+ & 0 \\ 0 & 0 & Q_4^- & Q_4^+ C_- \end{pmatrix} \tag{A.32}$$

Let

$$V = \begin{pmatrix} Q_1^+ & 0 & 0 & 0 \\ 0 & Q_2^+ & 0 & 0 \\ 0 & 0 & Q_3^+ & 0 \\ 0 & 0 & 0 & Q_4^+ \end{pmatrix} \tag{A.33}$$

then

$$V^{-1} D_{DW}^{M3} C = M \tag{A.34}$$

We have $\det[C] = 1$ but $\det[V] \neq 1$. However, V is independent of m, unlike D_{OL}^{M3}, and hence while $\det[V^{-1} D_{OL}^{M3}(m) C] \neq \det[M(m)]$ we do have

$$\det[M(1)^{-1} M(m)] = \det[(D_{DW}^{M3}(1))^{-1} D_{DW}^{M3}(m)] \tag{A.35}$$

This will provide the crucial link relating the determinants of the overlap operator to the domain wall operator. Now M has elements $C^{\pm}$ as given in eqns. A.43 and T_i given by

$$T_i = -\frac{Q_i^+}{Q_i^-} = \frac{1 - H_i}{1 + H_i} \tag{A.36}$$

where

$$H_i = \omega_i \gamma_3 D^{\parallel} \tag{A.37}$$

Eqn. A.36 is found via

$$\begin{aligned} T_i &= -(Q_i^-)^{-1}(Q_i^+) \\ &= -[(\omega_i D^{\|} + I)P_+ + (\omega_i D^{\|} - I)P_-]^{-1}[(\omega_i D^{\|} + I)P_- + (\omega_i D^{\|} - I)P_+] \\ &= -[(\omega_i D^{\|}) + (P_+ - P_-)]^{-1}[(\omega_i D^{\|}) - (P_+ - P_-)] \\ &= -[(\omega_i D^{\|}) + \gamma_3]^{-1}[(\omega_i D^{\|}) - \gamma_3] \\ &= -[(\omega_i \gamma_3 D^{\|}) + 1]^{-1}[(\omega_i \gamma_3 D^{\|}) - 1] \\ &= \frac{1 - H_i}{1 + H_i} \end{aligned} \tag{A.38}$$

The Shamir variants have the same structure with $H_i = \gamma_3 \frac{\omega_i D^{||}}{2+\omega_i D^{||}}$.

A.3.3 Overlap from Domain Wall

Having laid the groundwork, the final step is to show that

$$\det[D_{DW}^{M1}(1)^{-1} D_{DW}^{M3}(m)] = \det[D_{OL}^{M3}] \tag{A.39}$$

indicating that operators $D_{DW}^{M1}(1)^{-1} D_{DW}^{M3}(m)$ and D_{OL}^{M3} are physically equivalent. Approximations to the sign function, designated ϵ may be expressed as

$$\mathrm{sgn}(\gamma_3 D^{||}) \approx \epsilon = \frac{1 - \prod_i \frac{1-H_i}{1+H_i}}{1 + \prod \frac{1-H_i}{1+H_i}} = \frac{1-T}{1+T} \tag{A.40}$$

Then the overlap operator may be given by

$$D_{OL}^{M3}(m) = \frac{1 + im\gamma_3}{2} + \gamma_3 \frac{1-T}{1+T} \frac{1 - im\gamma_3}{2} \tag{A.41}$$

The Shur complement of M is $S = (C_- - T^{-1}C_+)$. So then we will show that

$$S^{M3}(m) = -(1 + T^{-1})\gamma_3 \times \frac{1}{2}[(1 + im\gamma_3) + \gamma_3 \mathrm{sgn}(\gamma_3 D^{||}(1 - im\gamma_3)] \tag{A.42}$$

We may reexpress eqn. A.43 as

$$\begin{aligned} C_+ &= P_+ - im\gamma_3 P- = \frac{1 + im}{2} - \frac{1 - im\gamma_3}{2}\gamma_3 \\ C_- &= P_- - im\gamma_3 P+ = \frac{1 - im}{2} - \frac{1 + im\gamma_3}{2}\gamma_3 \end{aligned} \tag{A.43}$$

so then

$$\begin{aligned} 2S^{M3}(m) &= [(1-im\gamma_3)-(1+im\gamma_3)\gamma_3 - T^{-1}((1-im\gamma_3)+(1+im\gamma_3)\gamma_3)] \\ &= [(1-T^{-1})(1-im\gamma_3)-(1+T^{-1})(1+im\gamma_3)\gamma_3] \\ &= (1+T^{-1})[\frac{T-1}{T+1}(1-im\gamma_3)-(1+im\gamma_3)\gamma_3] \\ &= -(1+T^{-1})[\epsilon(1-im\gamma_3)+(1+im\gamma_3)\gamma_3] \\ &= -(1+T^{-1})\gamma_3 \times [(1+im\gamma_3)+\gamma_3\epsilon(1-im\gamma_3)] \end{aligned} \tag{A.44}$$

In the standard mass case, we just replace $im\gamma_3$ with m and get

$$2S^{M1}(m) = -(1+T^{-1})\gamma_3 \times [(1+m)+\gamma_3\epsilon(1-m)] \tag{A.45}$$

which we see has

$$S^{M1}(1) = -(1+T^{-1})\gamma_3 \tag{A.46}$$

Hence we get the result the expression for the overlap in terms of the Schur complement of domain wall operators

$$D_{OL}^{M3}(m) = (S^{M1}(1))^{-1}S^{M3}(m) \tag{A.47}$$

from which we see the relationship between the domain wall and overlap operators via their determinants

$$\begin{aligned} \det[D_{OL}^{M3}(m)] &= \det[(S^{M1}(1))^{-1}S^{M3}(m)] \\ &= \det[(M^{M1}(1))^{-1}M^{M3}(m)] \\ &= \det[(D_{DW}^{M1}(1))^{-1}D_{DW}^{M3}(m)] \end{aligned} \tag{A.48}$$

The relation between the full overlap and domain wall operators is given in the main text.

A.4 Thirring Model

The physical equivalence of the original Thirring model $\mathcal{L}_{\text{Thir}} = \bar{\Psi}(\gamma_\mu\partial_\mu+m)\Psi+\frac{g^2}{2}\bar{\Psi}\gamma_\mu\Psi$ with its auxiliary field form $\mathcal{L}_A = \bar{\Psi}(\gamma_\mu\partial_\mu + m + igA_\mu\gamma_\mu)\Psi + \frac{1}{2}A_\mu A_\mu$ can be seen via

$$\begin{aligned} \mathcal{L}_A &= \bar{\Psi}(\not{\partial} + m + igA_\mu\gamma_\mu)\Psi + \frac{1}{2}A_\mu A_\mu \\ &= \bar{\Psi}(\not{\partial}+m)\Psi + igA_\mu\bar{\Psi}\gamma_\mu\Psi + \frac{1}{2}A_\mu A_\mu + \frac{g^2}{2}(\bar{\Psi}\gamma_\mu\Psi)^2 - \frac{g^2}{2}(\bar{\Psi}\gamma_\mu\Psi)^2 \\ &= \bar{\Psi}(\not{\partial}+m)\Psi + \frac{g^2}{2}(\bar{\Psi}\gamma_\mu\Psi)^2 + (\frac{A_\mu}{\sqrt{2}} + \frac{ig}{\sqrt{2}}\bar{\Psi}\gamma_\mu\Psi)^2 \\ &= \mathcal{L}_{\text{Thir}} + \frac{\tilde{A}_\mu^2}{2} \end{aligned} \tag{A.49}$$

where $\tilde{A}_\mu = A_\mu + ig\bar{\Psi}\gamma_\mu\Psi$. Now we have the auxiliary form partition function

$$\begin{aligned} Z_A &= \int \mathcal{D}[\Psi,\bar{\Psi}]\mathcal{D}[A_\mu]e^{-\int_x \mathcal{L}_A} \\ &= \int \mathcal{D}[\Psi,\bar{\Psi}]e^{-\int_x \mathcal{L}_{\text{Thir}}} \int \mathcal{D}[A_\mu]e^{-\int_x \frac{\tilde{A}_\mu^2}{2}} \\ &= const\ Z_{Thir} \end{aligned} \tag{A.50}$$

The last step holds since $\tilde{A}_\mu$ is linear in A_μ, so $\mathcal{D}[\tilde{A}_\mu] = \mathcal{D}[A_\mu]$ and hence

$$\int \mathcal{D}[A_\mu]e^{-\int_x \frac{\tilde{A}_\mu^2}{2}} = \int \mathcal{D}[\tilde{A}_\mu]e^{-\int_x \frac{\tilde{A}_\mu^2}{2}} = const \tag{A.51}$$

Hence the physics is the same since scaling the partition function does not change the physics. The constant is regularisation dependent.

A.5 Measurement Derivations

The following derivative

$$\begin{aligned} C = \frac{\partial \ln Z}{\partial m} &= \frac{1}{Z}\frac{\partial Z}{\partial m} \\ &= \frac{1}{Z}\frac{\partial}{\partial m}\langle Z_F\rangle_G \\ &= \frac{1}{Z}\langle\frac{\partial Z_F}{\partial m}\rangle_G \end{aligned} \tag{A.52}$$

combined with

$$\begin{aligned} \frac{\partial Z_F}{\partial m} &= \frac{\partial}{\partial m}\int \mathcal{D}[\psi,\bar{\psi}]\exp(-\bar{\psi}D\psi) \\ &= \int \mathcal{D}[\psi,\bar{\psi}]\frac{\partial}{\partial m}[\exp(-\bar{\psi}(D^0 + mD^m)\psi)] \\ &= -\int \mathcal{D}[\psi,\bar{\psi}]\bar{\psi}D^m\psi\exp(-\bar{\psi}D\psi) \\ &= -\langle\bar{\psi}D^m\psi\rangle_F \end{aligned} \tag{A.53}$$

leads to

$$\begin{aligned} C = \frac{\partial \ln Z}{\partial m} &= -\frac{1}{Z}\langle\langle\bar{\psi}D^m\psi\rangle_F\rangle_G \\ &= -\frac{1}{Z}\langle\text{Tr}[D^m D^{-1}]\det[D]\rangle_G \\ &= -\langle\text{Tr}[D^m D^{-1}]\rangle \end{aligned} \tag{A.54}$$

Taking the next derivative

$$\begin{aligned}\chi = \frac{\partial^2 \ln Z}{\partial m^2} &= \frac{\partial}{\partial m}[\frac{1}{Z}\langle\frac{\partial Z_F}{\partial m}\rangle_G] \\ &= \frac{-1}{Z^2}\langle\frac{\partial Z_F}{\partial m}\rangle_G^2 + \frac{1}{Z}\langle\frac{\partial^2 Z}{\partial m^2}\rangle_G \\ &= \frac{1}{Z}\langle\frac{\partial^2 Z_F}{\partial m^2}\rangle_G - (\frac{1}{Z}\langle\frac{\partial Z_F}{\partial m}\rangle_G)^2\end{aligned} \tag{A.55}$$

and

$$\begin{aligned}\frac{\partial^2 Z_F}{\partial m^2} &= -\int \mathcal{D}[\psi,\bar{\psi}]\frac{\partial}{\partial m}[\bar{\psi}D^m\psi\exp(-\bar{\psi}D\psi) \\ &= \int \mathcal{D}[\psi,\bar{\psi}]\bar{\psi}D^m\psi\bar{\psi}D^m\psi\exp(-\bar{\psi}D\psi) \\ &= \langle\bar{\psi}D^m\psi\bar{\psi}D^m\psi\rangle_F \\ &= (\mathrm{Tr}[D^m D^{-1}]^2 - \mathrm{Tr}[(D^m D^{-1})^2])\det(-D)\end{aligned} \tag{A.56}$$

leads to

$$\begin{aligned}\chi = \frac{\partial^2 \ln Z}{\partial m^2} &= \frac{1}{Z}\langle\frac{\partial^2 Z_F}{\partial m^2}\rangle_G - (\frac{1}{Z}\langle\frac{\partial Z_F}{\partial m}\rangle_G)^2 \\ &= \frac{1}{Z}\langle\langle\bar{\psi}D^m\psi\bar{\psi}D^m\psi\rangle_F\rangle_G - (\frac{1}{Z}\langle\langle\bar{\psi}D^m\psi\rangle_F\rangle_G)^2\end{aligned} \tag{A.57}$$

And hence

$$\begin{aligned}\chi = &\frac{1}{Z}\langle\mathrm{Tr}[D^m D^{-1}]^2 Z_F\rangle_G \\ &- \frac{1}{Z}\langle\mathrm{Tr}[(D^m D^{-1})^2])Z_F\rangle_G \\ &- (\frac{1}{Z}\langle\mathrm{Tr}[D^m D^{-1}]Z_F\rangle_G)^2\end{aligned} \tag{A.58}$$

And finally

$$\begin{aligned}\chi &\equiv \langle\bar{\psi}D^m\psi\bar{\psi}D^m\psi\rangle - \langle\bar{\psi}D^m\psi\rangle^2 \\ &= \langle\mathrm{Tr}[D^m D^{-1}]^2\rangle - \langle\mathrm{Tr}[(D^m D^{-1})^2]\rangle - \langle\mathrm{Tr}[D^m D^{-1}]\rangle^2 \\ &= \langle\Sigma^2\rangle - \langle\mathrm{Tr}[(D^m D^{-1})^2]\rangle - \langle\Sigma\rangle^2\end{aligned} \tag{A.59}$$

The middle terms, the connected terms, are typically discarded since they are computationally relatively expensive and assumed to be negligible. We have along the way given the general definition of susceptibility of an observable O, $\chi_O = \langle O^2\rangle - \langle O\rangle^2$.

Note the difference in meaning between $\langle\cdot\rangle$ containing Grassmann variables and those just containing numbers, the former referring to measurement integrals of form eqn. 2.1, and the latter meaning the averages according to eqn. 2.18.

A.5.1 Overlap Condensate with Standard Mass Term

The overlap operator with standard mass term is given by

$$D^1_{OL} = \frac{1+m}{2} + \frac{1-m}{2}V \tag{A.60}$$

We separate the mass term $D^1_{OL} = D^0_{OL} + mD^{M1}_{OL}$ to get

$$D^0_{OL} = \frac{1}{2} + \frac{1}{2}V \tag{A.61}$$

$$D^{M1}_{OL} = \frac{1}{2} - \frac{1}{2}V \tag{A.62}$$

and want to find the trace $\mathrm{Tr}[D^{M1}_{OL}(D^1_{OL})^{-1}]$ and we have, making use of $V = \frac{2D^1_{OL}-1-m}{1-m}$:

$$\begin{aligned} D^{M1}_{OL}(D^1_{OL})^{-1} &= \frac{\frac{1}{2} - \frac{1}{2}V}{\frac{1}{2} + \frac{1}{2}V + m(\frac{1}{2} - \frac{1}{2}V)} \\ &= \{\frac{1+V+m(1-V)}{1-V}\}^{-1} \\ &= \{\frac{1 + \frac{2D^1_{OL}-1-m}{1-m} + m(1 - \frac{2D^1_{OL}-1-m}{1-m})}{1 - \frac{2D^1_{OL}-1-m}{1-m}}\}^{-1} \\ &= \{\frac{D^1_{OL}(1-m)}{1-D^1_{OL}}\}^{-1} \\ &= \frac{1}{(1-m)}\frac{1-D^1_{OL}}{D^1_{OL}} \\ &= \frac{1}{1-m}((D^1_{OL})^{-1} - 1) \end{aligned} \tag{A.63}$$

Twisted Mass Formulation

Now we consider the overlap operator with twisted mass term and it carries through in exactly the same way.

$$D^3_{OL} = \frac{1+im\gamma_3}{2} + V\frac{1-im\gamma_3}{2} \tag{A.64}$$

which separates into $D^3_{OL} = D^0_{OL} + mD^{M3}_{OL}$, with D^0_{OL} as above, to get

$$D^0_{OL} = \frac{1}{2} + \frac{1}{2}V \tag{A.65}$$

$$D^{M3}_{OL} = (1-V)\frac{i\gamma_3}{2} \tag{A.66}$$

Now we have $V = (2D_{OL}^3 - 1 - im\gamma_3)(1 - im\gamma_3)^{-1}$ and so

$$\begin{aligned} D_{OL}^{M3} D_{OL}^{-1} &= (1-V)i\gamma_3[1+V+(1-V)im\gamma_3]^{-1} \\ &= (1-(2D_{OL}^3 - 1 - im\gamma_3)(1-im\gamma_3)^{-1})i\gamma_3 \\ &\times [1+(2D_{OL}^3 - 1 - im\gamma_3)(1-im\gamma_3)^{-1} + (1-(2D_{OL}^3 - 1 - im\gamma_3)(1-im\gamma_3)^{-1})im\gamma_3]^{-1} \\ &= (1-D_{OL}^3)i\gamma_3[(-im\gamma_3 + D_{OL}^3) + (1-D_{OL}^3)im\gamma_3]^{-1} \\ &= (1-D_{OL}^3)i\gamma_3[(D_{OL}^3)(1-im\gamma_3)]^{-1} \\ &= (1-D_{OL}^3)i\gamma_3(1-im\gamma_3)^{-1}(D_{OL}^3)^{-1} \\ &= (1-D_{OL}^3)\frac{-1}{i\gamma_3+m}(D_{OL}^3)^{-1} \end{aligned} \tag{A.67}$$

And by the cyclic property of traces of matrices we have

$$\begin{aligned} \mathrm{Tr}[D_{OL}^{M3} D_{OL}^{-1}] &= \mathrm{Tr}[(1-D_{OL}^3)\frac{-1}{i\gamma_3+m}(D_{OL}^3)^{-1}] \\ &= \mathrm{Tr}[\frac{-1}{i\gamma_3+m}(D_{OL}^3)^{-1}(1-D_{OL}^3)] \\ &= \mathrm{Tr}[\frac{-1}{i\gamma_3+m}((D_{OL}^3)^{-1}-1)] \end{aligned} \tag{A.68}$$

Left Twisted Mass Formulation

Now we consider the overlap operator with twisted mass term and it carries through in exactly the same way.

$$D_{OL}^4 = \frac{1+im\gamma_3}{2} + \frac{1-im\gamma_3}{2}V \tag{A.69}$$

which separates into $D_{OL}^4 = D_{OL}^0 + mD_{OL}^{M3}$, with D_{OL}^0 as above, to get

$$D_{OL}^0 = \frac{1}{2} + \frac{1}{2}V \tag{A.70}$$

$$D_{OL}^{M4} = \frac{i\gamma_3}{2}(1-V) \tag{A.71}$$

Now we have $V = (1 - im\gamma_3)^{-1}(2D^4_{OL} - 1 - im\gamma_3)$ and so

$$\begin{aligned}
D^{M4}_{OL}(D^4_{OL})^{-1} &= i\gamma_3(1-V)[1+V+im\gamma_3(1-V)]^{-1} \\
&= i\gamma_3(1-(1-im\gamma_3)^{-1}(2D^4_{OL}-1-im\gamma_3)) \\
&\times [1+(1-im\gamma_3)^{-1}(2D^4_{OL}-1-im\gamma_3)+im\gamma_3(1-(1-im\gamma_3)^{-1}(2D^4_{OL}-1-im\gamma_3))]^{-1} \\
&= i\gamma_3(1-im\gamma_3)^{-1}((1-im\gamma_3)-(2D^4_{OL}-1-im\gamma_3)) \\
&\times [(1-im\gamma_3)^{-1}((1-im\gamma_3)+(2D^4_{OL}-1-im\gamma_3) \\
&+ im\gamma_3(1-im\gamma_3)^{-1}((1-im\gamma_3)-(2D^4_{OL}-1-im\gamma_3))]^{-1} \\
&= i\gamma_3(1-D^4_{OL})[(-im\gamma_3+D^4_{OL})+im\gamma_3(1-D^4_{OL})]^{-1} \\
&= i\gamma_3(1-D^4_{OL})[(1-im\gamma_3)(D^4_{OL})]^{-1} \\
&= i\gamma_3(1-D^4_{OL})(D^4_{OL})^{-1}(1-im\gamma_3)^{-1} \\
&= i\gamma_3((D^4_{OL})^{-1}-1)(1-im\gamma_3)^{-1}
\end{aligned} \tag{A.72}$$

And by the cyclic property of traces of matrices we have

$$\mathrm{Tr}[D^{M4}_{OL}(D^4_{OL})^{-1}] = \mathrm{Tr}[D^{M3}_{OL}(D^3_{OL})^{-1}] \tag{A.73}$$

Appendix B

Numerical Aspects

B.1 Monte Carlo Integration

Monte Carlo integration is the go-to tool for integration over high dimensional spaces. Consider the integral

$$I = \int_V dx\ f(x) \tag{B.1}$$

and

$$Z = \int_V dx \tag{B.2}$$

then we may approximate the integral with

$$I \approx \frac{Z}{N} \sum f(x_i) = Z \langle f \rangle \tag{B.3}$$

where the same points x_i are taken uniformly randomly from the domain of integration V. However we may choose the points x_i from a non-uniform distribution in order to improve the convergence rate. This is importance sampling. The points thus chosen are more likely to contribute significantly to the calculation. Consideration of the Gaussian integral $I = \int_{-\infty}^{\infty} e^{-x^2} dx$ highlights the benefit (need) of sampling near the peak rather than the tails. To proceed, we may reexpress the integration as

$$I = \int_V dx\ w(x) \frac{f(x)}{w(x)} \tag{B.4}$$

with

$$Z = \int_V dx\ w(x) \tag{B.5}$$

and then we may approximate the integral with

$$I \approx \frac{Z}{N} \sum \frac{f(x_i)}{w(x_i)} = Z \langle f/w \rangle \tag{B.6}$$

where the same points x_i are taken non-uniformly randomly with weighting $w(x)$ from the domain of integration V.

For our measurements in chapter 4 we then have

$$\begin{aligned} I &\equiv \frac{1}{Z}\int \mathcal{D}[U]\exp(-S_G[U])\det[D[U]]\hat{O}[U] \\ &= \frac{1}{N}\sum \hat{O}[U_i] \end{aligned} \tag{B.7}$$

where the U_i are chosen with weighting $\exp(-S_G[U])\det[D[U]]$ and

$$Z = \int \mathcal{D}[U]\exp(-S_G[U])\det[D[U]] \tag{B.8}$$

B.2 Markov Chain Monte Carlo Integration

Markov chain Monte Carlo integration methods use Markov chains to produce the samples used in Monte Carlo integration. A slightly more detailed presentation of the Metropolis algorithm, which is the foundation of the hybird method given in the main text, is given below, following online lecture notes [66].

In general we want to find a vector A with probability distribution function $p(A)$. This can be achieved as follows.

1. Choose any initial vector A_0.
2. Choose a proposal probability distribution $J(A'|A)$, so that $\int \mathcal{D}[A']\ J(A'|A) = 1$.
3. Loop for $n = 1, ...N$
   - Choose a proposal A', with probability $p(A') = J(A'|A^{n-1})$
   - Calculate Metropolis-Hastings ratio

$$r = \frac{p(A')J(A^{n-1}|A')}{p(A^{n-1})J(A'|A^{n-1})} \tag{B.9}$$

   - Assign A^n according to

$$A^n = \begin{cases} A' & \text{with probability: } \min\{1, r)\} \\ A^{n-1} & \text{otherwise} \end{cases}$$

If we insist on the proposal distribution being symmetric, then the ratio reduces to

$$r = \frac{p(A')}{p(A^{n-1})} \tag{B.10}$$

which results in the *Metropolis algorithm* given in section 6.1. The two key properties of the algortihm are *ergodicity* and having *detailed balance*. The first is the ability to reach all possible distributions from any starting distribution, i.e. the space of possible distributions has no isolated states or subsets of states from which the algoithm cannot escape. Formally, for some N large enough, $\forall A, A^0$

$$P(A^N = A|A^0) > 0 \tag{B.11}$$

The second property is that the probability of going from one state to another is equal to the probability of the reverse. Detailed balance may then be expressed as

$$P[A^n = A^1|A^{n-1} = A^2] = P[A^n = A^2|A^{n-1} = A^1] \tag{B.12}$$

Observing that the probability to get from one state to another is the combination of the proposal and acceptance probabilites we have that

$$P[A^n = A'|A^{n-1}] = rJ(A'|A^{n-1}]) \tag{B.13}$$

B.3 Noisy Estimators and Point Sampling

For sparse matrices, multiplying a vector by the inverse of the matrix is often much faster than calculating the full inverse matrix. Further, individual entries of a matrix may be estimated through multiplication with a vector of random numbers. This provides a rough and (relatively) rapid method for calculating the trace of the inverse action matrix.

Let M be an $n \times n$ real matrix, and η be an n vector of standard Gaussian random variables, then let

$$\xi = M^{-1}\eta = A\eta \tag{B.14}$$

and so

$$\xi_j = \sum_k A_{jk}\eta_k \tag{B.15}$$

hence

$$\xi_j\eta_i = \eta_i\xi_j = \eta_i \sum_k A_{jk}\eta_k \tag{B.16}$$

and thus

$$\langle \eta_i\xi_j \rangle = \langle \eta_i \sum_k A_{jk}\eta_k \rangle = \sum_k A_{jk} \langle \eta_i\eta_k \rangle = A_{ji} \tag{B.17}$$

For complex Gaussian random variables $\langle \eta_i\eta_j \rangle = 2i$, so must multiply by the conjugate instead since $< \eta_i^\dagger\eta_k >= 0$, so

$$< \eta_i^\dagger\xi_j >=< \eta_i^\dagger \sum_k A_{jk}\eta_k >= \sum_k A_{jk} < \eta_i^\dagger\eta_k >= A_{ji} \tag{B.18}$$

The complex normal random variables have half variance components, i.e. $\eta_j = X_j + iY_j$, where $X_j \sim \mathcal{N}(0, \frac{1}{2})$ and similarly $Y_j \sim \mathcal{N}(0, \frac{1}{2})$. This ensures $\langle \eta_j^\dagger \eta_j \rangle = 1$.

Note it is not required to populate the entirety of the η vector. Each entry provides for the corresponding column of the matrix, i.e. if η_0 is a random variable, and the rest are zeros, then we still have $\langle \eta_0^\dagger \xi_i \rangle = A_{0i}$.

With Gaussian random vectors the more samples used, the closer the approximation gets to the target value $\langle \eta_j^\dagger \eta_k \rangle \to 1$, and the smaller the contributions of the off-target values $\langle \eta_i^\dagger \eta_k \rangle \to 0$, $i \neq j$. However, Gaussian rvs are not the only option available. A uniform distribution over the elements $-1, 1, -i, i$ instead may be used ($\mathbb{Z}_2$ noise), and in certain circumstances it can provide a better solution more quickly. The target value is always exact $\langle \eta_j^\dagger \eta_k \rangle = 1$, and it is only the off-target values which must decay. On testing, we found no advantage in our simulations, though, since to achieve a sufficient level of decay in the off-target values, the approximation to the target value was sufficient. The $\mathbb{Z}_2$ noise has a slightly smaller variance.

Alternatively, we can extract the kth column of A, $\xi = A\eta$ exactly by setting $\eta_j = 0$ for $k \neq j$ and $\eta_k = 1$. Then $\xi_j = A_{jk}$. This is the point method.

B.4 Autocorrelation

The error in non correlated data is given by $\text{err} = \frac{1}{\sqrt{N}}\sigma$ where σ is the standard deviation. Correlated data error may be corrected through the integrated time scale τ_{int}.

$$\text{err} = \sqrt{\frac{\tau_{\text{int}}}{N}}\sigma \tag{B.19}$$

where

$$\tau_{\text{int}} = 1 + 2\sum_{t=1}^{\infty} \hat{c}(t) \tag{B.20}$$

and

$$\hat{c}(t) = \frac{\hat{C}(t)}{\hat{C}(0)} \tag{B.21}$$

$$\hat{C}(t) = \langle C(x)C(y) \rangle_{|x-y|=t} \tag{B.22}$$

When we have $\hat{C}(t) = e^{-t/\tau}$ we also have

$$\tau_{\text{int}} = 1 + 2\sum_{1}^{\infty} e^{-t/\tau_{\text{exp}}} = 1 + \frac{2e^{-1/\tau}}{1 - e^{-1/\tau}} \approx 2\tau \tag{B.23}$$

Bibliography

[1] Simon Hands, Fixed point four Fermi theories, In *APCTP - ICTP Joint International Conference (AIJIC 97) on Recent Developments in Nonperturbative Quantum Field Theory*, pages 193–211, 5 1997.

[2] L. Del Debbio, S. J. Hands, and J. C. Mehegan, The Three-dimensional Thirring model for small N(f), *Nucl. Phys. B*, 502:269–308, 1997, doi: 10.1016/S0550-3213(97)00435-5.

[3] S. Hands, Domain wall fermions for planar physics, *JHEP*, (09), 2015, URL arXiv:hep-lat/1507.07717.

[4] Björn H. Wellegehausen, Daniel Schmidt, and Andreas Wipf, Critical flavor number of the Thirring model in three dimensions, *Phys. Rev. D*, 96(9):094504, 2017, doi: 10.1103/PhysRevD.96.094504.

[5] J. Lenz, B. Wellegehausen, and A. Wipf, Absence of chiral symmetry breaking in thirring models in 1+2 dimensions, *Phys. Rev. D*, (100), 2019, URL arXiv:hep-lat/1905.00137.

[6] Andreas W. Wipf and Julian J. Lenz, Symmetries of Thirring Models on 3D Lattices, *Symmetry*, 14(2):333, 2022, doi: 10.3390/sym14020333.

[7] Simon Hands, Michele Mesiti, and Jude Worthy, Critical behaviour in the single flavor Thirring model in 2+1D, *Phys. Rev. D*, 102(9):094502, 2020, doi: 10.1103/PhysRevD.102.094502.

[8] Simon Hands, Michele Mesiti, and Jude Worthy, Critical behaviour in the single-flavor Planar Thirring Model, *PoS*, LATTICE2021:539, 2022, doi: 10.22323/1.396.0539.

[9] Jude Worthy and Simon Hands, Properties of Overlap and Domain Wall Fermions in the 2+1D Thirring Model, *PoS*, LATTICE2021:317, 2022, doi: 10.22323/1.396.0317.

[10] C. Gattringer and C. B. Lang, *Quantum Chromodynamics on the Lattice*, Springer, Berlin, Heidelberg, 2010.

[11] P. T. Matthews and Abdus Salam, The Green's functions of quantized fields, *Nuovo Cim.*, 12:563–565, 1954, doi: 10.1007/BF02781302.

[12] P. T. Matthews and Abdus Salam, Propagators of quantized field, *Nuovo Cim.*, 2: 120–134, 1955, doi: 10.1007/BF02856011.

[13] Ashok Das, *Lectures on quantum field theory*, 2008.

[14] B. R. Holstein, A brief introduction to chiral perturbation theory, *CZECHOSLOVAK J. OF PHYS. 310.*, 2000.

[15] Stefan Scherer, Introduction to chiral perturbation theory, *Adv. Nucl. Phys.*, 27: 277, 2003.

[16] F. del Aguila, L. Ametller, Gordon L. Kane, and J. Vidal, Vector Like Fermion and Standard Higgs Production at Hadron Colliders, *Nucl. Phys. B*, 334:1–23, 1990, doi: 10.1016/0550-3213(90)90655-W.

[17] Holger Bech Nielsen and M. Ninomiya, Absence of Neutrinos on a Lattice. 1. Proof by Homotopy Theory, *Nucl. Phys. B*, 185:20, 1981, doi: 10.1016/0550-3213(82)90011-6, [Erratum: Nucl.Phys.B 195, 541 (1982)].

[18] D. Friedan, A proof of the nielsen-ninomiya theorem, *Commun. Math. Phys.*, (85): 481–490, 1982.

[19] I. Montvay and G. Munster, *Quantum fields on a lattice*, Cambridge Monographs on Mathematical Physics. Cambridge University Press, 3 1997, ISBN 978-0-521-59917-7, 978-0-511-87919-7, doi: 10.1017/CBO9780511470783.

[20] Paul H. Ginsparg and Kenneth G. Wilson, A remnant of chiral symmetry on the lattice, *Phys. Rev. D*, 25:2649–2657, May 1982, doi: 10.1103/PhysRevD.25.2649, URL https://link.aps.org/doi/10.1103/PhysRevD.25.2649.

[21] D. B. Kaplan, A method for simulating chiral fermions on the lattice, *Phys. Lett. B*, (288):342–347, 1992, URL arXiv:hep-lat/9206013.

[22] H. Neuberger, Exactly massless quarks on the lattice, *Phys.Lett.B*, (417), 1998, URL arXiv:hep-lat/9707022.

[23] Yoshio Kikukawa and Herbert Neuberger, Overlap in odd dimensions, *Nucl. Phys. B*, 513:735–757, 1998, doi: 10.1016/S0550-3213(97)00779-7.

[24] Wolfgang Bietenholz, Solutions of the Ginsparg-Wilson relation and improved domain wall fermions, *Eur. Phys. J. C*, 6:537–547, 1999, doi: 10.1007/s100520050364.

[25] Ting-Wai Chiu, GW fermion propagators and chiral condensate, *Phys. Rev. D*, 60: 034503, 1999, doi: 10.1103/PhysRevD.60.034503.

[26] C.G. Callan and J.A. Harvey, Anomalies and fermion zero modes on strings and domain walls, *Nuclear Physics B*, 250(1):427–436, 1985, ISSN 0550-3213, doi: https://doi.org/10.1016/0550-3213(85)90489-4, URL https://www.sciencedirect.com/science/article/pii/0550321385904894.

[27] K. Jansen, Domain wall fermions and chiral gauge theories, *Phys. Rept.*, 273:1–54, 1996, doi: 10.1016/0370-1573(95)00081-X.

[28] Yigal Shamir, Chiral fermions from lattice boundaries, *Nucl. Phys. B*, 406:90–106, 1993, doi: 10.1016/0550-3213(93)90162-I.

[29] V. Furman and Y. Shamir, Axial symmetries in lattice qcd with kaplan fermions, *Nucl. Phys. B*, (439):54–78, 1995, URL ,arXiv:hep-lat/9405004.

[30] A. Borici, Truncated overlap fermions, *Nucl. Phys. Proc. Suppl.*, (83), 2000, URL arXiv:hep-lat/9909057.

[31] T.-W. Chiu, Optimal domain wall fermions, *Phys. Rev. Lett.*, (90), 2003, URL arXiv:hep-lat/0209153.

[32] Rajamani Narayanan and Herbert Neuberger, Infinitely many regulator fields for chiral fermions, *Phys. Lett. B*, 302:62–69, 1993, doi: 10.1016/0370-2693(93)90636-V.

[33] Rajamani Narayanan and Herbert Neuberger, A Construction of lattice chiral gauge theories, *Nucl. Phys. B*, 443:305–385, 1995, doi: 10.1016/0550-3213(95)00111-5.

[34] Robert G. Edwards, Urs M. Heller, and Rajamani Narayanan, The overlap Dirac operator: Topology and chiral symmetry breaking, *Chin. J. Phys.*, 38:594–604, 2000.

[35] S. Hands, From domain wall to overlap in 2+1d, *Phys. Lett. B*, (754), 2016, URL arXiv:hep-lat/1512.05885.

[36] Dorota M. Grabowska and David B. Kaplan, Chiral solution to the Ginsparg-Wilson equation, *Phys. Rev. D*, 94(11):114504, 2016, doi: 10.1103/PhysRevD.94.114504.

[37] A. D. Kennedy, Approximation theory for matrices, *Nucl. Phys. Proc. Suppl.*, (128C), 2004, URL arXiv:hep-lat/0402037.

[38] B. Jegerlehner, Krylov space solvers for shifted linear systems, 12 1996.

[39] A. D. Kennedy, Algorithms for dynamical fermions, *Nucl. Phys. Proc. Suppl.*, (128C), 2006, URL arXiv:hep-lat/0607038.

[40] R. Brower, H. Neff, and K. Orginos, The mobius domain wall fermion algorithm, *Computer Physics Communications*, 220:1–19, 2012.

[41] E. I. Zolotarev, Application of elliptic functions to the questions of functions deviating least and most from zero, *Zap. Imp. Akad. Nauk. St. Petersburg*, (30), 1877.

[42] A. D. Kennedy, Fast evaluation of Zolotarev coefficients, In *QCD and numerical analysis III. Proceedings, 3rd International Workshop, Edinburgh, UK, June 30-July 4, 2003*, pages 169–189, 2004, URL arXiv:hep-lat/0402038.

[43] T.-W. Chiu, T.-H. Hsieh, C.-H. Huang, and T.-R. Huang, A note on the zolotarev optimal rational approximation for the overlap dirac operator, *Phys. Rev. D*, (66), 2002, URL arXiv:hep-lat/0206007.

[44] J. Worthy, Improved numerical methods for domain wall fermions in 2+1d, Master's thesis, Swansea University, 2019.

[45] Walter E. Thirring, A Soluble relativistic field theory?, *Annals Phys.*, 3:91–112, 1958, doi: 10.1016/0003-4916(58)90015-0.

[46] S. Hands, On the critical flavor number in the 2+1d thirring model, *Phys. Rev. D*, 99(3), 2019, URL arXiv:hep-lat/1811.04818.

[47] J. J. Binney, N. J. Dowrick, A. J. Fisher, and M. E. J. Newman, *The Theory of critical phenomena: An Introduction to the renormalization group*, 1992.

[48] Simon Hands, Aleksandar Kocic, and John B. Kogut, Four Fermi theories in fewer than four-dimensions, *Annals Phys.*, 224:29–89, 1993, doi: 10.1006/aphy.1993.1039.

[49] Luigi Del Debbio and Simon Hands, Monte Carlo simulation of the three-dimensional Thirring model, *Phys. Lett. B*, 373:171–177, 1996, doi: 10.1016/0370-2693(96)00137-2.

[50] Simon Hands, Numerical Study of the $2+1d$ Thirring Model with U($2N$)-Invariant Fermions, In *35th International Symposium on Lattice Field Theory*, 8 2017.

[51] L. P. Kadanoff, Scaling laws for Ising models near T(c), *Physics Physique Fizika*, 2:263–272, 1966, doi: 10.1103/PhysicsPhysiqueFizika.2.263.

[52] Friedrich Gehring, Holger Gies, and Lukas Janssen, Fixed-point structure of low-dimensional relativistic fermion field theories: Universality classes and emergent symmetry, *Phys. Rev. D*, 92(8):085046, 2015, doi: 10.1103/PhysRevD.92.085046.

[53] P. Hernandez, K. Jansen, and M. Luscher, Locality properties of neuberger's lattice dirac operator, *Nucl. Phys. B*, 552, 1999, URL arXiv:hep-lat/9808010.

[54] Rajamani Narayanan, Transition in the spectral gap of the massless overlap Dirac operator coupled to abelian fields in three dimensions, *Phys. Rev. D*, 103(9):094514, 2021, doi: 10.1103/PhysRevD.103.094514.

[55] Michael Creutz, Partial quenching and chiral symmetry breaking, *PoS*, LATTICE2014:070, 2014, doi: 10.22323/1.214.0070.

[56] S. Duane, A. D. Kennedy, B. J. Pendleton, and D. Roweth, Hybrid Monte Carlo, *Phys. Lett. B*, 195:216–222, 1987, doi: 10.1016/0370-2693(87)91197-X.

[57] M. A. Clark, The Rational Hybrid Monte Carlo Algorithm, *PoS*, LAT2006:004, 2006, doi: 10.22323/1.032.0004.

[58] D. Weingarten, Monte carlo algorithms for qcd, *Nuc. Phys. B (Prc. Suppl.)*, (9), 1989.

[59] A. D. Kennedy, Ivan Horvath, and Stefan Sint, A New exact method for dynamical fermion computations with nonlocal actions, *Nucl. Phys. B Proc. Suppl.*, 73:834–836, 1999, doi: 10.1016/S0920-5632(99)85217-7.

[60] M. A. Clark and A. D. Kennedy, 2005, URL https://github.com/mikeaclark/AlgRemez.

[61] R. Brower, H. Neff, and K. Orginos, Mobius fermions: Improved domain wall chiral fermions, *Nucl. Phys. Proc. Suppl.*, 140, 2005, URL arXiv:hep-lat/0409118.

[62] Henri P. Gavin, The levenberg-marquardt method for nonlinear least squares curve-fitting problems, 2022, URL https://people.duke.edu/~hpgavin/ExperimentalSystems/lm.pdf.

[63] Aleksandar Kocic, Simon Hands, John B. Kogut, and Elbio Dagotto, The Equation of State and Critical Exponents in Quenched Strongly Coupled QED, *Nucl. Phys. B*, 347:217–242, 1990, doi: 10.1016/0550-3213(90)90558-U.

[64] S. Hands, M. Mesiti, and E. Bennett, 2018, URL https://github.com/sa2c/thirring-rhmc.

[65] S. Hands, Towards critical physics in 2+1d with u(2n)-invariant fermions, *JHEP*, 11, 2016, URL arXiv:hep-lat/1610.04394.

[66] Iowa State University, 2008, URL https://www.ece.iastate.edu/~namrata/EE527_Spring08/l4c.pdf.